Westhoff, Philipp:

A method to investigate many-body Liouvillian spectra beyond the steady state

Masterarbeit, Wintersemester 2025

Gutachter*in: Schollwöck, Ulrich

Fakultät für Physik

Ludwig-Maximilians-Universität München

https://doi.org/10.5282/ubm/epub.129477

A method to investigate many-body Liouvillian spectra beyond the steady state

Philipp Westhoff

SIGILL: UNIVERSITAT: LUDOVIC: MAXIM:

Munich 2025

Master's Thesis

A method to investigate many-body Liouvillian spectra beyond the steady state

Faculty of physics
Ludwig-Maximilians-Universität München

Philipp Westhoff

Munich, October 29th, 2025

Submitted in partial fulfillment of the requirements for the degree of M. Sc.
Supervised by Prof. Dr. Ulrich Schollwöck

Abstract

Open quantum systems, where quantum dynamics is influenced by (non-)Markovian environments, have attracted increasing attention due to their rich physical properties. Understanding phenomena such as non-equilibrium phases, anomalous thermalization, and dissipative state preparation requires the knowledge of the low-lying eigenvalues and eigenstates of the Lindbladian. In this thesis, we introduce a framework that systematically computes not only steady states but also low-lying excited states in large, dissipative, interacting quantum many-body systems. The framework is based on tensor-network methods and utilizes recent advances in complex-time Krylov spaces. Extending these ideas to the challenging non-Hermitian eigenvalue problem ubiquitous in open quantum systems enables simulations at unprecedented Hilbert-space dimensions.

We employ the framework to analyze a dissipative state preparation protocol for Bose-Einstein condensates (BECs) on optical lattices. Analytical and numerical studies allow us to characterize the steady state and perform a finite-size scaling of the dissipative gap, uncovering strong evidence for non-linear hydrodynamics described by the Kardar-Parisi-Zhang universality class. Furthermore, we show analytically that the dissipative state preparation can be substantially accelerated via the quantum Mpemba effect. Our approach exploits weak symmetries to analytically identify a class of simple, experimentally realizable states that converge exponentially faster to the steady state than typical random initializations.

Overall, this work establishes a versatile framework for the spectral analysis of generic open quantum many-body systems, enabling the analysis of complex collective phenomena and additionally paving the way toward faster dissipative preparation of highly entangled states in analog quantum simulators.

In loving memory of Ulla and Heinz

Publications

This thesis is based on the following publications and preprints:

[1] **Philipp Westhoff**, Sebastian Paeckel, Mattia Moroder:
'Fast and direct preparation of a genuine lattice BEC via the quantum Mpemba effect'
Arxiv preprint *(2504.05549)*

[2] **Philipp Westhoff**, Mattia Moroder, Ulrich Schollwöck, Sebastian Paeckel:
'A Tensor Network Framework for Lindbladian Spectra and Steady States'
Arxiv preprint *(2509.07709)*

My contributions to the different projects are shortly summarized below:

Ref. [1]	I carried out the MPS calculations, simulating the dynamics with the help of MM and SP. I devised and worked out the symmetry arguments for the emergence of the Mpemba effect, with the help of MM and SP. I contributed to the figures and writing of the text.
Ref. [2]	I developed the CLIK-MPS framework with the help of SP and MM. I developed the warm-up procedure, the efficient arithmetic as well as the convergence analysis. I carried out simulations of the Bose-Hubbard model and contributed to the figures and writing of the text.

Contents

1 Introduction

In the past decades, open quantum systems have received increasing attention because of their exotic physical properties, ranging from dissipative phase transitions [3, 4, 5] to anomalous thermalization [6]. Additionally, experimental advances in quantum simulators [7, 8], digital quantum processors [9, 10], control over strong light-matter interactions [11, 12], and the unprecedented precision in optically driving low-dimensional materials [13, 14] make the theoretical understanding of such systems more relevant than ever. However, even in the case of memoryless, or Markovian, environments, where the dynamics of the system is governed by the Lindbladian [15], the theoretical description is challenging. Yet, analyzing many of the key phenomena occurring in open quantum systems relies on understanding the spectrum and eigenstates of the Lindbladian. For instance, the properties of the steady state, which corresponds to the eigenvalue $\lambda_1 = 0$, are important for dissipative phase transitions (DPTs) [3, 4, 5] and dissipative state preparation (DSP) [16, 17]. Additionally, the dissipative gap, which is the real part of the first excited eigenvalue, dictates the experimentally relevant relaxation timescale of the system [18, 1]. Many other phenomena, such as anomalous thermalization processes [18, 6], topological effects [19, 20, 21] and metastability [22], require the knowledge of a large portion of the Lindbladian spectrum and eigenvectors.

However, analytic explorations of quantum many-body systems coupled to large environments are mostly limited to non-interacting systems via third quantization [23] or the Lyapunov equation [24]. Numerical treatment on the other hand is complicated by the inherent non-Hermiticity of the Lindbladian, which prevents the direct application of variational algorithms such as the density matrix renormalization group (DMRG) [25, 26, 27, 28].

Other numerical methods have been limited to computing the steady state, using approaches such as tensor-network (TN) methods [29, 30, 31, 32, 33, 34, 35, 36, 37, 38], possibly combined with Monte-Carlo sampling [39, 40, 41, 42, 43], to neural quantum states [44, 45, 46], quantum algorithms [47, 48, 49, 50, 51, 52], and phase space methods [53]. Exploration of other parts of the Lindbladian spectrum mostly rely on exact diagonalization (ED) methods, which are severely limited in the accessible system sizes. As a consequence, there is an urgent need for an efficient and flexible framework to access information about Lindbladian spectra.

In this thesis we introduce the TN-based *complex-time Lindbladian Krylov subspace matrix-product-state* (CLIK-MPS) framework, which is capable of calculating a set of low-lying eigenvalues and eigenvectors accurately and efficiently. The framework utilizes time evolutions which can be readily carried out with standard TN methods [54]. Additionally, we harness the specific properties of the Lindbladian spectrum and its non-Hermiticity to exploit complex-time evolutions [55, 56] and span an optimized Krylov space. We propose physically motivated warm-up procedures that generate tailored initial states to target the steady state as well as slowly decaying eigenvectors. Crucially, we are able to find initial states that converge not to the steady state, but to the slowest decaying mode, without knowing the explicit form of the steady state itself. These novel developments are accompanied by methods to efficiently calculate expectation values and overlaps within the subspace, methods to evaluate the quality of the approximated eigenvalues, and benchmarks against ED results.

To assess the capabilities of the new framework, we consider the challenging physical problem of analyzing and optimizing a dissipative state preparation (DSP) protocol. These protocols can be used to prepare highly-entangled states in analog quantum simulators based on ultracold atoms in optical lattices [57, 58, 59, 60, 61, 62, 63]. While other schemes are based on coherent control, it has recently been shown that adding controlled dissipation can be computationally [64, 65] and experimentally [66] advantageous in terms of robustness to noise and efficiency. Despite significant progress, however, DSP protocols still suffer from long preparation times [67, 68] due to the closing of the dissipative gap upon increasing the system size. One unexplored route to address this problem is finding optimized, fast-converging initializations.

In this thesis, we analyze a dissipative protocol to prepare Bose-Einstein condensates (BECs) [17, 69] and devise ways to speed up the preparation. After we examine the properties of the steady state of the protocol using analytic methods, we extensively employ CLIK-MPS to verify the predictions. Crucially, we also use it to carry out a finite-size scaling of the dissipative gap, uncovering strong evidence for the emergence of the Kardar-Parisi-Zhang (KPZ) universality class. This implies a superlinear scaling of the relaxation time, necessitating fast-converging initial states. To overcome this obstacle, we build upon the Mpemba effect, which originally referred to the classical non-equilibrium phenomenon whereby hot systems cool faster than warm ones, and exploit it to substantially speed up the DSP protocol. By harnessing weak symmetries of the Lindbladian, we analytically classify its eigenvalues according to their associated transformation behavior. This enables us to identify initial states which feature vanishing overlap with the slowly decaying channels, speeding up the preparation exponentially. Using CLIK-MPS we also show that this analysis remains valid across a wide parameter range and is stable upon varying the system size. By finding tailored unitaries, the analysis carries over to finite-momenta BECs [70], which we propose to implement via lattice shaking techniques [71, 72, 73].

The thesis is structured as follows: Section 2 provides an overview of the theoretical background and establishes the notation used throughout this work. This includes a discussion of Markovian quantum systems, vectorization, symmetries, and matrix-product state (MPS) methods. In Section 3, we introduce the main result of this thesis, the complex-time Lindbladian Krylov subspace MPS (CLIK-MPS) framework. After a short introduction to the main ideas, we discuss Krylov spaces, complex-time evolutions, warm-up procedures, and efficient Krylov arithmetic in detail. We benchmark the framework and devise ways for straightforward convergence analysis. In Section 4, we analyze a DSP protocol for preparing BECs both analytically and using CLIK-MPS. We investigate the properties of the prepared state analytically and extract critical exponents. Importantly, we discuss the symmetries of the system and use them to find rapidly-converging states, similar to the quantum Mpemba effect. This is complemented by numerical studies quantifying the speedups and identifying the admissible parameter regime.

2 Theory and Methods

This chapter provides an overview of the theoretical background and notation we will need in the scope of the thesis. In Section 2.1, we review the notion of open quantum systems and Markovianity. We discuss the Lindblad equation and derive properties of the Lindbladian superoperator. In Section 2.2, we describe the notion of vectorization to handle density matrices as vectors. In Section 2.3, we discuss the importance of symmetries in the open quantum system setting and the differences compared to isolated ones. In Section 2.4, we give a short introduction to a paradigmatic non-equilibrium effect occurring in open quantum systems, the quantum Mpemba effect. Lastly, in Section 2.5, we discuss the main numerical methods used in this thesis, which rely on matrix-product states (MPSs).

2.1 Open quantum systems and the Born-Markov approximation

Quantum systems in the realm of many-body physics typically need to be approximated by a tractable minimal model capturing the intricate physics of the full system. Often, this requires the treatment of interactions with the surrounding environment, such as light-matter interactions [11, 12] in optically driven low-dimensional materials [13, 14] and methods to describe such systems have been used for a long time [74]. Eventually, these systems were termed *open quantum systems*, and a mathematical precise description was put forward by Gorini, Kossakowski, and Sudarshan [74] and independently Lindblad [15]. They described the most general form of a generator of time evolution under the assumption of Markovianity, building on mathematically precise concepts, such as complete positivity. Since for this thesis, many of these mathematical details are not of major importance, we lay them aside and describe the ideas from a physical point of view. Most importantly though, we are interested in general properties of open quantum systems, which we briefly deduce from the analysis.

To describe open quantum systems accurately, we need to formalize them. Assume we are given a system S_{tot} potentially consisting of many constituents of different species or spatial position, for instance, a lattice with particles. Importantly, we are not interested in the dynamics of the whole system, but only of a small subsystem A. The complementary subsystem $B = S_{\text{tot}} \setminus A$ is not of explicit interest and we will refer to it as the *environment*. The full system is characterized by a Hamiltonian $\hat{H}_S$, which can be split up into the following three contributions

$$\hat{H}_S = \hat{H}_A \otimes \hat{\mathbb{1}}_B + \alpha \hat{H}_{A\leftrightarrow B} + \hat{\mathbb{1}}_A \otimes \hat{H}_B \ , \tag{2.1}$$

where $\hat{H}_A$ ($\hat{H}_B$) summarize all terms concerning only the constituents in A (B), while $\hat{H}_{A\leftrightarrow B}$ contains interactions between subsystems A and B. The prefactor α controls the interaction strength between the two subsystems. In principle, given some initial configuration $\hat{\rho}_S$ of S_{tot}, we are then able to calculate the full dynamics of the system by solving the Schrödinger equation induced by $\hat{H}_S$. In reality though, only the dynamics of the subsystem A is of interest, which is obtained by tracing out the environment with the partial trace $\hat{\rho}_A(t) = \mathrm{Tr}_B\, \hat{\rho}_S(t)$. This procedure requires the explicit treatment of the environment, which is challenging due to, for instance, a large amount of degrees of freedom. Instead we would be interested in a description similar to a Schrödinger equation for the density matrix $\hat{\rho}_A$. This is quite difficult and the dynamics at time t of the subsystem may depend explicitly on earlier times $t' \ll t$, preventing a direct formulation in terms of a linear differential equation [75]. Nevertheless, we can consider the Markovian limit, where the timescales of correlation and relaxation of the environment are far smaller than the typical timescales of the system. Additionally, we assume that the interaction with the environment B is weak, that is, $\alpha \ll 1$ (Born limit). Using these approximations, one can derive a differential equation for the reduced density matrix $\hat{\rho}_A$ starting from the full Schrödinger equation [76, 77]. This equation is termed the *Lindblad equation* and is given by

$$\frac{\mathrm{d}\hat{\rho}_A}{\mathrm{d}t} = \mathcal{L}\hat{\rho}_A = -\mathrm{i}\big[\hat{H}_A, \hat{\rho}_A\big] + \sum_l \hat{L}_l \hat{\rho}_A \hat{L}_l^\dagger - \frac{1}{2}\big\{\hat{L}_l^\dagger \hat{L}_l, \hat{\rho}_A\big\}\ , \tag{2.2}$$

where we introduced the *Lindbladian superoperator* $\mathcal{L}$ and the jump operators $\hat{L}_l$. The difference compared to the isolated case is given by the sum over the jump operators, which contain the information about the coupling to the environment. This Lindblad equation is a simplification of the actual system, and the requirements for its validity need to be checked before it is used. Nevertheless, over the past decades it has proven to be a powerful tool to analyze open quantum systems and is extensively employed throughout the field. It is important to note that the original derivation of the Lindblad equation [74, 15] is based on a purely mathematical consideration.

The Lindbladian superoperator features a variety of interesting properties. It is a linear operator on the space of density matrices, but it is, in general, non-Hermitian. The spectrum of $\mathcal{L}$ is thus given by the generalized spectral decomposition, where $\mathcal{L}$ is decomposed into eigenvalues λ_j and right and left eigenvectors $\hat{r}_j$, $\hat{l}_j$ such that for a general density matrix $\hat{\rho}$

$$\mathcal{L}\hat{\rho} = \sum_i \lambda_i \hat{r}_i \mathrm{Tr}\left(\hat{l}_i^\dagger \hat{\rho}\right)\ , \quad \mathrm{Tr}\big(\hat{l}_n^\dagger \hat{r}_m\big) = \delta_{nm}\ . \tag{2.3}$$

In the following, we order the eigenvalues decreasing according to their real part, that is, $\mathrm{Re}\,\lambda_1 \geq \mathrm{Re}\lambda_2 \geq \dots$ and with slight abuse of language, we call $\hat{r}_j$ and $\hat{l}_j$ eigenvectors or eigenmodes despite them being matrices. A density matrix $\hat{\rho}$ of the subsystem at time t can now be written in terms of the Lindbladian eigen-decomposition as

$$\hat{\rho}(t) = \sum_i \mathrm{e}^{\lambda_i t} \hat{r}_i \mathrm{Tr}\left(\hat{l}_i^\dagger \hat{\rho}\right)\ . \tag{2.4}$$

We are then interested in properties of the spectrum and eigenvectors of $\mathcal{L}$. The constraint of a physical time evolution restricts the spectrum to $\mathrm{Re}\,\lambda_k \leq 0$, as otherwise states might be exponentially amplified over time [76]. Additionally, the time evolution must conserve the trace of the density matrix [78], which implies that there must be at least one eigenvalue at zero, $\lambda_1 = 0$. The corresponding right eigenvector $\hat{r}_1$ needs to be a physical state, as Eq. (2.4) implies that an initial state will converge to this eigenvector in the infinite time limit, $\hat{\rho}(t) \to c_1 \hat{r}_1$ as $t \to \infty$, where c_1 is a normalization factor. This right eigenvector is also referred to as the *steady state* of the system. In the case of a degenerate eigenvalue 0, an arbitrary initial state converges to a superposition of the corresponding right eigenvectors. Furthermore, all other eigenvalues need to be traceless, as their contribution to the trace features an explicit time dependence in the evolution.

In case of a unique steady state, we can actually pin the form of the corresponding left eigenvector $\hat{l}_1$. Considering two arbitrary density matrices $\hat{\rho}$ and $\hat{\rho}'$ and using the conservation of the trace, we find that $\mathrm{Tr}(\hat{l}_1 \hat{\rho}') = \mathrm{Tr}(\hat{l}_1 \hat{\rho})$. This equation is only true for the identity, fixing the left eigenvector $\hat{l}_1 = \hat{\mathbb{1}}$. The generalization to multiple steady states is discussed in Sec. 2.3. Additionally, time evolution needs to preserve the Hermiticity of a state, which enforces a specific structure on the spectrum,

$$\mathcal{L}\hat{r}_j = \lambda_j \hat{r}_j \qquad \Longrightarrow \qquad \mathcal{L}\hat{r}_j^\dagger = \lambda_j^* \hat{r}_j^\dagger\ , \tag{2.5}$$

and similarly for the left eigenmodes [79]. This result is quickly proven by decomposing the right eigenvector into Hermitian parts. As a consequence, the spectrum is symmetric around the real axis.

Although the restrictions used in the derivation of the Lindblad equation are quite severe, there are ways to approximate more complex open quantum systems in a similar fashion. For instance the mesoscopic leads approach [80, 81], approximates couplings to a complex environment with lead modes, and the system plus lead modes can again be described by a Lindblad equation. This is an instance of the so-called *Markovian embedding* approach.

2.2 Vectorization

Compared to the Schrödinger equation, the Lindblad equation has some drawbacks. Besides the complicated structure of the Lindbladian itself, it is an equation for density matrices. Therefore, the Lindbladian is a superoperator, acting on the space of density matrices. Since we would like to use tools from isolated systems, it is advantageous to recast everything into the language of vectors and operators acting on these. To do so, we can rely on the fact that the space of matrices acting on $\mathbb{R}^D$ is isometric to the vector space $\mathbb{R}^{2D}$. A mapping corresponding to this isometry can easily be defined, for example through

$$\begin{pmatrix} a_{11} & a_{12} \\ a_{21} & a_{22} \end{pmatrix} \to \begin{pmatrix} a_{11} \\ a_{21} \\ a_{12} \\ a_{22} \end{pmatrix} , \tag{2.6}$$

in the case $D = 2$. Typically we describe a lattice with L sites, each featuring a local Hilbert space $\mathfrak{H}_{\mathrm{loc}}$. The full system is then described by a Hilbert space of the form $\mathfrak{H}_{\mathrm{loc}}^L = \bigotimes_{j=1}^L \mathfrak{H}_{\mathrm{loc}}$, and consequently, the density matrices on this space live in $\mathfrak{H}_{\mathrm{loc}}^{L\times L}$. In close analogy to the case of $\mathbb{R}^{D\times D}$, there is now an isometry to the space $\mathfrak{H}_{\mathrm{loc}}^{2L}$, which also describes a lattice with $2L$ sites, double the amount of the initial ones. Consequently, density matrices may be described as vectors on a lattice of doubled size, and the Lindbladian as an operator on this new lattice. A useful relation when working with vectorization is how to apply it to products of matrices $\hat{M}_1$, $\hat{M}_2$, $\hat{M}_3$

$$\hat{M}_1\hat{M}_2\hat{M}_3 \to \left(\hat{M}_3^T \otimes \hat{M}_1\right)|\hat{M}_2\rangle\!\rangle , \tag{2.7}$$

where we denoted the vectorization of a matrix $\hat{M}$ as $|M\rangle\!\rangle$. This relation makes it possible to vectorize the Lindbladan Eq. (2.2)

$$\hat{\mathcal{L}} = \underbrace{-\mathrm{i}\hat{H} \otimes \hat{\mathbb{1}} + \hat{\mathbb{1}} \otimes \mathrm{i}\hat{H}^{\mathrm{T}}}_{\hat{\mathcal{H}}} + \underbrace{\sum_l \hat{L}_l \otimes \left(\hat{L}_l^\dagger\right)^{\mathrm{T}} - \frac{1}{2}\hat{L}_l^\dagger\hat{L}_l \otimes \hat{\mathbb{1}} - \frac{1}{2}\hat{\mathbb{1}} \otimes \left(\hat{L}_l^\dagger\hat{L}_l\right)^{\mathrm{T}}}_{\hat{\mathcal{D}}} , \tag{2.8}$$

where we denote the Hamiltonian part as $\hat{\mathcal{H}}$ and the dissipative part as $\hat{\mathcal{D}}$. We say, that if an operator is on the left side of the tensor product it acts on the *physical* sites, while it acts on the *auxiliary* sites if it is on the right side of the product and the only term connecting the two sublattices is the $\hat{L}_l \otimes \hat{L}_l$ term. This description makes it possible to represent the dynamics of a density matrix $|\rho\rangle\!\rangle$, written as a vector, fully in the vectorized Hilbert space as

$$\frac{\mathrm{d}}{\mathrm{d}t}|\rho(t)\rangle\!\rangle = \hat{\mathcal{L}}|\rho(t)\rangle\!\rangle . \tag{2.9}$$

Unfortunately, there are some subtleties connected to vectorization. Since there is an isometry, one would naively argue that the norm of the density matrices equals the canonical norm of the vectorized counterparts. This is true, but the natural trace norm $\mathrm{Tr}(\hat{\rho})$ on the density matrix space is not the Hilbert space norm, which is the two norm given by $\mathrm{Tr}\big(\hat{\rho}^\dagger\hat{\rho}\big)^{1/2}$. Consequently, we have

$$\mathrm{Tr}\big(\hat{\rho}_1^\dagger\hat{\rho}_2\big) = \langle\!\langle \rho_1|\rho_2\rangle\!\rangle \,. \tag{2.10}$$

The natural normalization constraint for density matrices can now be reformulated using the *vectorized identity* $|\mathbb{1}\rangle\!\rangle$. The constraint reads

$$1 = \mathrm{Tr}(\hat{\rho}) = \langle\!\langle \mathbb{1}|\rho\rangle\!\rangle \,. \tag{2.11}$$

Combining Eq. (2.7) with Eq. (2.10) we can calculate expectation values of some operator $\hat{O}$ directly in the vectorized form as

$$\mathrm{Tr}\big(\hat{O}\hat{\rho}\big) = \langle\!\langle \mathbb{1}|\hat{\mathbb{1}}\otimes\hat{O}|\rho\rangle\!\rangle \,. \tag{2.12}$$

Throughout the thesis, we make a slight abuse of notation and typically only write $\hat{O}$ instead of $\hat{\mathbb{1}}\otimes\hat{O}$. Appendix A.2 provides detailed instructions on how to calculate the vectorized identity explicitly. This shows, that many interesting quantities can be directly calculated in the vectorized framework and we do not need to map vectorized states back to density matrices, which is often a delicate procedure.

2.3 A dive into symmetries, conserved quantities and steady states

Symmetries are crucial to understand the underlying structure of a physical system. They almost always help to simplify a problem, and many exactly solvable quantum mechanical systems are solvable only because they exhibit many symmetries (e.g. the hydrogen atom or the harmonic oscillator). In closed systems obeying a unitary time evolution, symmetries always lead to a quantity $\hat{J}$ being conserved over time. Since open quantum systems do not evolve according to a unitary time evolution, they behave fundamentally different. Heuristically, this can be understood by considering a system coupled to an environment, where the full system has a symmetry with associated conserved quantity $\hat{J}$. However, the globally conserved quantity is typically not a locally conserved one due to transport between the system and environment, leading to the conservation of $\hat{J}$ being broken when looking at the system of interest.

Thus, even Markovian systems obeying the Lindblad equation can have symmetries that do not admit a conserved quantity [82]. A rigorous description of symmetries in the Markovian case requires a unitary transformation $\hat{U}$, which acts on a density matrix $\hat{\rho}$ as $\hat{U}\hat{\rho}\hat{U}^\dagger$. Its vectorization reads $\hat{\mathcal{U}} = \hat{U}\otimes\hat{U}^*$. The Lindbladian $\hat{\mathcal{L}}$ is invariant under the action of $\hat{\mathcal{U}}$ if it fulfills

$$\big[\hat{\mathcal{U}},\hat{\mathcal{L}}\big] = 0 \,, \tag{2.13}$$

and thus has a symmetry [82]. This definition is similar to the closed system case. The unitary $\hat{U}$ now admits a unique Hermitian generator $\hat{Q}$ by $\hat{U} = \exp\big(-2\pi\alpha i\hat{Q}\big)$, where α is a real number (we consider the continuous case here, but the discrete symmetry case is analogous). In closed systems, this directly implies that $\hat{Q}$ commutes with the Hamiltonian and is a conserved quantity. Instead in open quantum systems, the generator $\hat{\mathcal{Q}}$ of the vectorized unitary $\hat{\mathcal{U}}$ commutes with the Lindbladian, and it is not guaranteed that $\hat{Q}$ is also conserved, and we distinguish between two types of symmetries: A symmetry is called *strong* if the generator is conserved during time evolution. For *weak symmetries*, this is not the case and the generator is not conserved. We would like to get a more quantitative distinction between the two cases on the level of commutators. Indeed one can show that $\hat{U}$ is a strong symmetry if the generator commutes with both the Hamiltonian and *all* jump operators, that is

$$\hat{Q}\text{ is a conserved quantity} \Longleftarrow \big[\hat{H},\hat{Q}\big] = 0,\; \big[\hat{L}_j,\hat{Q}\big] = 0 \quad \forall j \,. \tag{2.14}$$

We will not prove this, but we refer the reader to [82]. The right-hand side is a strictly stronger condition than Eq. (2.13). Heuristically, this result can be understood from the fact that the breaking of conservation originates from local transport into the environment. The right-hand side in Eq. (2.14) implies that this transport does not change $\hat{Q}$, since it is mediated through the jump operators.

Building upon this, we aim to investigate the implications of symmetries for the spectrum of the Lindbladian. Especially for the steady state it seems reasonable that conserved quantities fix some of their properties. Since the steady state subspace typically has much lower dimensionality than the full vectorized Hilbert space, many initial configurations converge to the same steady state, losing information about their exact initial properties. However, the information about the initial value of a conserved quantity must be reflected in the steady state. Thus, there have to be different steady states depending on the value of the conserved quantity. Putting this onto a more rigorous footing, assume that the conserved quantity $\hat{Q}$ has eigenvalues $\{\lambda_k\}_{k,n}$ and eigenvectors $\{\,|\psi_{k,n}\rangle\,\}_{k,n}$, where k numbers the different values, while n numbers the degeneracy. Prepare the initial density matrices $\hat{\rho}_{k_1}$ and $\hat{\rho}_{k_2}$ as $\hat{\rho}_k = |\psi_{k,1}\rangle\langle\psi_{k,1}|$, such that $\mathrm{Tr}\big(\hat{Q}\hat{\rho}_{k_{1,2}}\big) = \lambda_{k_{1,2}}$. Over time, the density matrices converge to some steady states, $\hat{\rho}_{k_1} \to \hat{\rho}_{\mathrm{ss}}^{k_1}$ and $\hat{\rho}_{k_2} \to \hat{\rho}_{\mathrm{ss}}^{k_2}$. Since we deal with a conserved quantity, we find

$$\mathrm{Tr}\big(\hat{Q}\rho_{\mathrm{ss}}^{k_1}\big) = \lambda_{k_1} \neq \lambda_{k_2} = \mathrm{Tr}\big(\hat{Q}\rho_{\mathrm{ss}}^{k_2}\big) \ . \tag{2.15}$$

This directly implies that the two steady states are indeed different from each other. Most importantly, if we do this inductively for each of the eigenvalues, we find that the dimensionality of the steady state subspace is bigger than the number of different eigenvalues of the conserved quantity. Note that although more general theorems about the characterization of the steady state subspace and associated conserved quantities hold [82], we do not want to go into more detail in the scope of this thesis.

Since for symmetric systems the unitary representation of the symmetry commutes with the Lindbladian, the Lindbladian has a block diagonal structure in the eigenbasis of the generator $\hat{\mathcal{Q}}$, similarly to the isolated system case. We can label the individual blocks by the eigenvalues of the generator. For a weak symmetry there are blocks which only contain decaying eigenvectors of the Lindbladian, that is, eigenvectors with finite real part. If an initial state has a component in such a subspace, it will decay over time and vanish when approaching the steady state, thus changing the expectation of the generator $\hat{Q}$ over time. This also gives an intuitive explanation for the fact that the Lindbladian might be block diagonal but nevertheless does not admit a conserved quantity.

Interestingly it is possible to pin down the block which contains the steady state sector for an arbitrary symmetry. Let's consider the generator $\hat{\mathcal{Q}}$ of the vectorized unitary, which can be written in terms of the initial generator $\hat{Q}$ as

$$\hat{\mathcal{Q}} = \hat{Q} \otimes \hat{\mathbb{1}} - \hat{\mathbb{1}} \otimes \hat{Q}^{\mathrm{T}} \ . \tag{2.16}$$

Now the following theorem holds.

Theorem: Consider the generator $\hat{\mathcal{Q}}$ of a vectorized unitary constituting a symmetry of some Lindbladian $\hat{\mathcal{L}}$. Then, the steady state(s) $|\rho_{\mathrm{ss}}\rangle\!\rangle$ satisfy $\hat{\mathcal{Q}}|\rho_{\mathrm{ss}}\rangle\!\rangle = 0$.

Proof: Let's start with the vectorized identity. We can directly determine its behavior by going back into the density matrix picture

$$\hat{\mathcal{Q}}|\mathbb{1}\rangle\!\rangle = |\hat{Q}\hat{\mathbb{1}} - \hat{\mathbb{1}}\hat{Q}^{\dagger}\rangle\!\rangle = |\hat{Q} - \hat{Q}\rangle\!\rangle = 0 \ , \tag{2.17}$$

where we used the specific form of the vectorized generator Eq. (2.16) and the Hermiticity of $\hat{Q}$. This equation implies, that $|\mathbb{1}\rangle\rangle$ is an eigenvector of $\hat{\mathcal{Q}}$, lying in the $\{\hat{\mathcal{Q}} = 0\}$ sector. Consequently, it is orthogonal to all states in the span of $\{\hat{\mathcal{Q}} \neq 0\}$. Since the steady state has a finite trace, its overlap with $|\mathbb{1}\rangle\rangle$ needs to be nonvanishing. But $\hat{\mathcal{Q}}$ and the Lindbladian are simultaneously diagonalizable, and the steady state is completely supported in the $\{\hat{\mathcal{Q}} = 0\}$ sector. Note that the proof does not rely on any properties of the steady state except its physicality, and the result holds independently of the steady state manifold's dimension.

This theorem reveals a lot of information about the steady state. In the sections to come, we will use it extensively. Unfortunately, for excited states a similar theorem does not exist, since the proof relies on the physicality of the steady state, and excited states need to be traceless, hence they are especially not physical states. In Section 2.1, we deduced that for a unique steady state, the left eigenmode is given by $\hat{\mathbb{1}}$. Especially in the case of a conserved quantity, this result can be generalized if each symmetry sector features a unique steady state. Projecting the Lindblad equation into a single symmetry sector, we recover a Lindblad equation with a unique steady state. By Sec. 2.1, the left eigenmodes are thus given by the identities in the respective symmetry sectors. Although further generalizations of these theorems can be made in a similar fashion, the subspaces onto which the vectorized identities need to be projected to yield left eigenvectors may get very complicated, and the left eigenmodes are not of practical use any more. In many physical scenarios, non-uniqueness of steady states actually originates from conserved quantities, and the projection onto symmetry sectors suffices. Note that this is also the case in the systems we look at throughout the thesis.

2.4 Nonequilibrium dynamics – the quantum Mpemba effect

The counterintuitive phenomenon of hot systems cooling down faster than warm ones was first explored by Erasto Mpemba and Denis Osborne in 1969 [83] and is since known as the Mpemba effect. While its occurrence in water is still debated, the effect was unambiguously measured in colloidal systems by Kumar and Bechhoefer in 2020 [84]. Already in 2017, it was described in a mathematically rigorous way for classical Markovian systems by Lu and Raz [85]. This theoretical explanation [85] is based on the idea, that an initialization cools down faster if it avoids the slowest decaying channels of the system. For the rigorous exploration Lu and Raz analyzed the spectral properties of the Liouvillian generator of the dynamics. They discovered that an Mpemba effect can occur when the initial microscopic configuration of the system is orthogonal to the slowest decaying mode of the Liouvillian.

By near analogy, this framework was recently generalized to open quantum systems by Carollo, Lasanta, and Lesanovsky [18]. As established in Section 2.1, the generator of time evolution in Markovian open quantum systems is given by the Lindbladian. Let's assume, for simplicity, that we have a unique steady state $\hat{\rho}_{\mathrm{ss}}$ and that the *dissipative gap* $\Delta = \min_{j:\,\mathrm{Re}\,\lambda_j \neq 0} \big(-\mathrm{Re}\,\lambda_j \big)$ is given by $\Delta = -\mathrm{Re}\,\lambda_2$. In this case the late time dynamics $t \gg 1/\Delta$ is dominated by the terms

$$\hat{\rho}(t) = \hat{\rho}_{\mathrm{ss}} + \mathrm{e}^{\lambda_2 t}\mathrm{Tr}\big(\hat{l}_2^\dagger \hat{\rho}\big)\hat{r}_2 + \mathcal{O}\big(\mathrm{e}^{\lambda_3 t}\big)\,. \tag{2.18}$$

Consequently, the state $\hat{\rho}(t)$ converges exponentially to the steady state with a characteristic relaxation time given by $1/\Delta$. Note that this relaxation timescale is universal, since it only depends on the structure of the system, not on the initial state. Nevertheless, the initialization enters into the relaxation dynamics by the prefactor $\mathrm{Tr}\big(\hat{l}_2^\dagger \hat{\rho}\big)$. If we choose a state $\hat{\rho}$ exhibiting vanishing overlap with $\hat{l}_2$, that is $\mathrm{Tr}\big(\hat{l}_2^\dagger \hat{\rho}\big) = 0$, the relaxation instead has the asymptotic behavior $\hat{\rho}(t) = \hat{\rho}_{\mathrm{ss}} + \mathcal{O}\big(\mathrm{e}^{\lambda_3 t}\big)$. This amounts to a change in the relaxation timescale from $-1/\mathrm{Re}\,\lambda_2$ to $-1/\mathrm{Re}\,\lambda_3$, which speeds up the relaxation by the relative ratio $\Delta_3 = \mathrm{Re}\,\lambda_3/\mathrm{Re}\,\lambda_2$. This effect is termed the *strong quantum Mpemba effect*, while the *weak quantum Mpemba effect* describes the scenario when $\mathrm{Tr}\big(\hat{l}_2^\dagger\hat{\rho}\big) \ll \mathrm{Tr}\big(\hat{l}_3^\dagger\hat{\rho}\big)$, leading to a convergence rate $-\mathrm{Re}\,\lambda_3$ at intermediate times only [6].

The generalization to multiple steady states is straightforward, but presents slight technical subtleties. For instance, in the case of particle number conserving bosonic systems, as considered mainly throughout this thesis, Sec. 2.3 entails that each particle number sector has at least one steady state. This implies an infinite number of linearly independent steady states. Therefore, we typically look at the Mpemba effect within each particle number sector individually. This is done by considering only initial states having a fixed number of particles for which the argumentation given above again applies.

Note that strictly speaking, the Mpemba effect only occurs if the fast-converging initialization is hotter than the typically used initial state. Since open systems are not at equilibrium, a temperature in the common thermodynamic sense is not defined, and one relies on the free energy to compare different states instead [6]. In this thesis, with a slight abuse of language, we refer to a faster convergence as an Mpemba effect regardless of the temperature of the states.

2.5 Matrix product states

Efficiently performing numerical calculations in large many-body systems presents several fundamental challenges. For one, the Hilbert space dimension increases exponentially with system size, leading to storage problems for the matrices and vectors one needs to handle. For sparse matrices, explicit storing can be done up to a Hilbert space dimensions which are insufficient for large scale interacting many-body systems [86].

In the past few decades, a lot of effort has been made to find physically sensible subspaces of the Hilbert space, which are easily parametrizable, while capturing the physically relevant states.

This gave rise to matrix-product states (MPSs), a class of states which fulfill these requirements [87, 88, 89, 27]. Given a lattice system with L sites, where each site l has a local Hilbert space $\mathfrak{H}_{\mathrm{loc}}$, the full Hilbert space is the tensor product of the local Hilbert spaces, $\mathfrak{H} = \mathfrak{H}_{\mathrm{loc}}^L$. A general state can now be written as a linear combination of product states, and we define a matrix-product state (MPS) by

$$|\psi\rangle = \sum_{\substack{i_1, i_2 \ldots, i_L \\ m_0, m_1, \ldots, m_L}} \left[\mathbf{A}^1_{i_1,m_0,m_1}\mathbf{A}^2_{i_2,m_1,m_2}\cdots\mathbf{A}^L_{i_L,m_{L-1},m_L}\right] |i_1\rangle \otimes |i_2\rangle \otimes \ldots \otimes |i_L\rangle \;, \tag{2.19}$$

where the elements elements $\mathbf{A}^l_{i_l,m_{l-1},m_l}$ can be summarized into a rank-three tensor for each site l (and m_0, m_L are dummy indices) [54]. The indices m_{l-1} and m_l are called bond indices (or virtual indices), and the number of their possible values is termed (left or right) bond dimension χ. We typically refer to the maximal bond dimension over all sites as the bond dimension χ of some MPS state. Obviously, this description only makes sense if the bond dimensions remain low, as otherwise storing and numerical operations become increasingly difficult. To understand if this description actually captures the physically relevant portion of the Hilbert space, we first look at the entanglement entropy $S(B)$ of some subregion B of the lattice for a general MPS state. One can easily establish the bound [27]

$$S(B) \leq 2\log\chi \;. \tag{2.20}$$

This result suggests a tight connection between the bond dimension and the entanglement entropy. For instance, groundstates of gapped local Hamiltonians obey an area law, leading to an $\mathcal{O}(1)$ scaling of the entanglement entropy in system size [90], and reasons why they are well

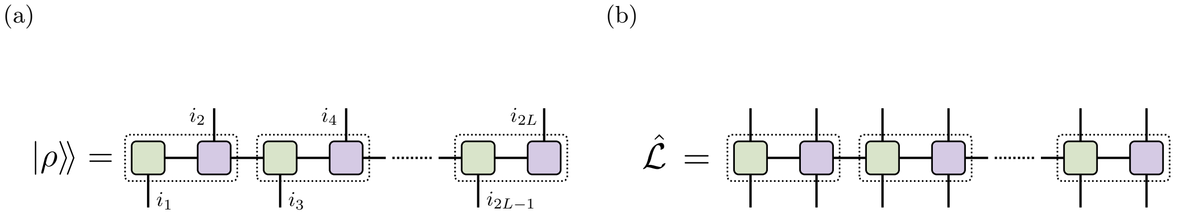

Figure 1: Schematic MPS and matrix-product operator (MPO) representations on the vectorized lattice. The lattice is ordered alternating between physical (green) and auxiliary (lilac) sites. Panel a): Vectorized density matrix as a MPS. Panel b): Local Lindbladian described by a MPO. The alternating order of physical and auxiliary sites leads to the Lindbladian staying local [92]. Adapted from [1, 2].

captured by ground state search via MPS techniques such as the density matrix renormalization group (DMRG) [27, 28, 25]. Unfortunately, there are also some setbacks for MPS, like gapless systems, which typically do not obey an area law, or the linear increase in entanglement entropy during time evolution, which leads to exponentially large bond dimensions [91]. This makes the need for methods systematically lowering bond dimensions to maintain numerical efficiency self-evident. The common method is truncating each matrix $\mathbf{A}^l_{i_l m_{l-1},m_l}$ by calculating the singular value decomposition (SVD) and discarding all contributions from the smallest singular values, such that the new bond dimension is below a given threshold.

One can also apply MPS methods to open quantum systems. In this case, there are several additional difficulties. For one, as we need to deal with density matrices, it is useful to vectorize them. This doubles the size of the lattice as discussed in Sec. 2.2, which may limit accessible system sizes. The vectorization itself possesses many freedoms in chosing the ordering of the new doubled lattice. We can use this to our benefit, as shown in Fig. 1. Since Lindbladians are often comprised of both a local Hamiltonian and local jump operators, we would like this locality to carry over to the description on the vectorized lattice, such that the vectorized Lindbladian only contains local terms. This is particularly useful, since local operators can be described as MPOs with bond dimensions independent of the lattice size [93, 94, 95]. We guarantee locality by alternating the physical and auxiliary sites of the vectorized lattice, which will lead to a local Lindbladian and computational benefits [92]. Indeed, if the Hamiltonian and jump operators involve local terms at most spanning over d sites ($d = 1$ for nearest neighbor interactions), the vectorized Lindbladian will contain only local terms spanning over $2d$ sites.

Due to the inherent non-Hermiticity of the Lindbladian, each initial configuration will time evolve to a fix point on the steady state manifold, as discussed in Sec. 2.1. Thus, while unitary components might lead to a linear increase in entanglement entropy in the short time dynamics, it saturates to the entanglement entropy of the steady state in the infinite time limit, which is a crucial numerical benefit over isolated systems. Nevertheless, the system size dependence of the steady state might lead to entanglement entropy increase in the thermodynamic (TD) limit, which again limits accessible system sizes for time evolution methods. Note that there are some rigorous results about area laws in open quantum systems: If the system features a dissipative gap in the TD-limit, the corresponding steady state obeys an area law and entanglement entropy scales as $\mathcal{O}(1)$ under some assumptions [96]. Unfortunately, in many interesting cases this is not satisfied, as for particle number conserving Lindbladians [97] or at dissipative phase transitions [3]. This especially highlights the necessity of truncation insensitive methods, which make finite-size scaling in large systems possible.

Up until now, we established some remarkable properties of the MPS representation that underscore its usefulness, however we did not introduce any tools to perform computations. Basic manipulations include the calculation of overlaps, MPO-MPS multiplication, MPS addition or expectation values and variances, for which there are luckily some quite efficient algorithms [98, 87, 93]. Although we do not want to dive into these methods in detail, it is important to note that their individual efficiency strongly depends on the bond dimension of the MPS or MPO: The numerical complexity of MPS overlaps scales as $\mathcal{O}\big(L\,\chi^3\big)$ [54] and of expectation values as $\mathcal{O}\big(L\,\chi^3\,\chi_{\hat{O}}\big)$ [54], where $\chi_{\hat{O}}$ is the bond dimension of the MPO $\hat{O}$. Furthermore, adding two MPS states $|\psi_{1,2}\rangle$ with bond dimensions $\chi_{1,2}$ will in general result in a state with a MPS representation with bond dimension $\chi_1 + \chi_2$. This makes repeated MPS addition prohibitively costly, which needs to be considered when working with MPS representations. MPO-MPS multiplication is even worse, since the bond dimensions need to be multiplied together in general.

Although these fundamental operations are quite costly, the MPS representation benefits from various methods to perform time evolutions. Naive time evolution is a prohibitively costly task. For instance simple trotterization requires MPO-MPS multiplication in each timestep, leading to exponentially increasing bond dimensions, if no truncation is performed. Sophisticated methods often build upon the time-dependent variational principle (TDVP) [99, 100, 54, 101, 102, 103]. It makes use of the fact that the full Schrödinger equation can be approximated through multiple local Schrödinger equations which only evolve a small number of sites and bond tensors at the same time [103]. The resulting equations can then be solved using Krylov subspace methods [54]. Note that the computational complexity increases with the number of sites the Schrödinger equation is projected onto, from a quadratic for one site (referred to as 1TDVP) to a cubic scaling with local Hilbert space dimension for two sites [54]. Consequently, 1TDVP is much more efficient especially for bosonic systems. Unfortunately though, 1TDVP suffers from problems describing the spread of correlations along the lattice, since it cannot increase bond dimensions, which makes it impractical in many situations.

This major problem was tackled by combining the the 1TDVP with local subspace expansions, resulting in the local subspace expansion time-dependent variational principle (LSE-TDVP) [101, 104, 102]. Since we work with bosonic systems which typically require a high local Hilbert space dimension of $\mathcal{O}(10)$ in this thesis, the LSE-TDVP is the method of choice when performing time evolutions.

For open quantum systems, the situation is complicated through the inherent non-Hermiticity of the Lindbladian, which is fundamentally different to the Hamiltonian case being Hermitian. This results in minor problems when performing the propagation in the local Krylov space, since it is not numerically practicable to exponentiate the non-Hermitian generator directly like in the case of a Hermitian one. Instead, we perform a brute force Taylor expansion of the exponential and cut it off at some maximal order M, by applying the generator M times, which is efficient as long as the Krylov space is low dimensional [105].

Throughout this thesis, we use the SyTen toolkit to perform TN operations [106, 107]. We use LSE-TDVP for time evolutions.

3 Krylov subspace methods – introducing CLIK-MPS

As established in Section 1 and 2, the Lindbladian spectrum contains rich information about the physical properties of the system it describes. For instance, the properties of the steady state, which is the eigenvector to the zero eigenvalue, is relevant for dissipative state preparation [17, 108, 1] and for characterizing non-equilibrium phases of matter [109, 3]. The dissipative gap, i.e. the real part of the first excited eigenvalue dictates the experimentally relevant relaxation timescale of the system [18, 1], and is the central quantity characterizing DPTs [3, 4]. Describing other phenomena such as anomalous thermalization processes [18, 6], topological effects [19, 20, 21] and metastability [22] even require the explicit knowledge of multiple excited eigenvectors and eigenvalues. Crucially, also the study of the quantum Mpemba effect, which will play a central role in Section 4, requires the knowledge of the slowest decaying left eigenmode in general [6, 18]. In Fig. 2a we summarize the relations between physical phenomena and the corresponding parts of the Lindbladian spectrum.

Although there have been methodological developments, they are typically restricted to computing the steady state or to small system sizes, which is insufficient for the study of many phenomena in large, many-body open quantum systems. A short overview of the available methods, their target quantities and reachable system sizes is presented in Fig. 2b. As a consequence, there is an urgent need for an efficient and flexible framework to overcome these limitations.

In this chapter we introduce complex-time Lindbladian Krylov subspace MPS (CLIK-MPS), a matrix-product state (MPS)-based framework capable of calculating the low-lying spectrum and eigenvectors of Lindbladians with high accuracy. We refine the idea of building a Krylov space with time-evolved states [110] by additionally considering complex-time contours [56] and physically motivated warm-up procedures, which make it possible to target excited states directly. These systematic improvements lead to unprecedented accuracy in approximating left and right eigenmodes and eigenvalues far beyond the steady state. Crucially, we also provide efficient subspace arithmetic that makes it possible to calculate expectation values and overlaps for large systems.

The chapter is organized as follows: First in Sec. 3.1, we introduce the basic ideas behind the framework, and we discuss why simple time evolution is insufficient for our purposes. Next, we give a detailed description of the framework in Sec. 3.2, where we elaborate on the efficient implementation of Krylov subspace representations in Sec. 3.2.1 and the benefit of complex-time evolution in Sec. 3.2.2. We discuss adjoint Lindbladian time evolution to approximate left eigenvectors in Sec. 3.2.3 and crucially, we introduce physically motivated warm-up procedures to increase accessible system sizes and to target slowly decaying modes more accurately in Sec. 3.2.4. To optimize the arithmetic, we derive ways to calculate expectation values and overlaps with eigenvectors directly inside the Krylov space in Sec. 3.2.5, bypassing numerically costly MPS arithmetic. A short discussion of the generalization of the framework to non-Markovian systems is given in Sec. 3.2.6. Lastly in Sec. 3.3, we benchmark the framework by evaluating low-lying eigenvalues and eigenvectors of a Bose-Hubbard Hamiltonian with Markovian dissipation, described by Eq. (3.1). We evaluate the performance of CLIK-MPS by comparing to data obtained through ED and other methods in Sec. 3.3.1. Additionally in Sec. 3.3.2, we discuss methods to assess the quality of the approximated spectrum and eigenvectors, which we test on large-scale systems.

Note that CLIK-MPS is extensively employed for various large-scale calculations in Sec. 4. This chapter is strongly based on the publication [2], that summarizes some of the work done in the scope of this thesis.

We perform numerical calculations at the example of a dissipative Bose-Hubbard model,

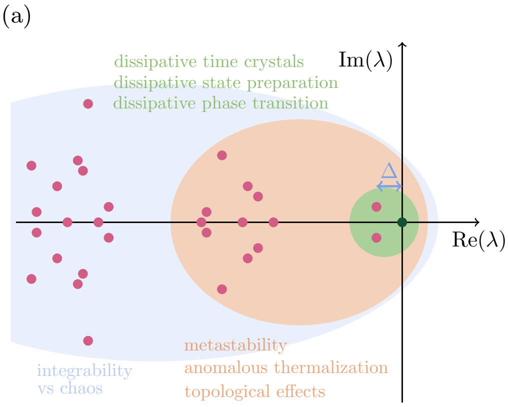

(b)

Method	Target quantity	dim $\mathcal{H}$
VQA [48, 49, 51]	steady state	$2^{12} \approx 10^{3}$
NQS [44, 45, 46]	steady state	$2^{16} \approx 10^{5}$
Variational MPO [30, 31, 34, 38]	steady state	$2^{100} \approx 10^{30}*$
Quantum MC [111, 112]	steady state	$2^{40} \approx 10^{12}$
ED [113, 114]	full spectrum	$2^{12} \approx 10^{3}$
CLIK-MPS	steady state, gap	$2^{130} \approx 10^{40}$
CLIK-MPS	spectral region	$2^{70} \approx 10^{21}$

Figure 2: Panel a): physical relevance of different parts of the Lindbladian spectrum. In most cases, the analysis of many-body Markovian open quantum systems relies on the Lindbladian steady state (dark green) and the Liouvillian gap Δ (green). However, some phenomena require a set of low-lying eigenvalues (orange) or even the full spectrum (blue). Panel b): target quantities and reachable Hilbert space dimensions for various existing methods compared to our new framework CLIK-MPS. The * indicates that for variational MPO methods, large system sizes of about 100 spins can be reached only for local Lindbladians that satisfy entanglement area laws [30]. The figures are adapted from [2].

which is characterized by

$$\hat{H} = -J \sum_{j=1}^{L-1} \left(\hat{b}_{j+1}^{\dagger} \hat{b}_{j} + \text{h.c.} \right) + \frac{U}{2} \sum_{j=1}^{L} \left[\hat{b}_{j}^{\dagger} \right]^{2} \left[\hat{b}_{j} \right]^{2} , \qquad \hat{L}_{j} = \sqrt{\kappa} \left(\hat{b}_{j+1}^{\dagger} + \hat{b}_{j}^{\dagger} \right) \left(\hat{b}_{j+1} - \hat{b}_{j} \right) \ . \tag{3.1}$$

Here, L is the number of sites, J the hopping strength, U the onsite interaction and κ the dissipation strength. The system features a strong $U(1)$-symmetry (c.f. Sec. 4.1), which gives rise to a particle number conservation. We thus typically consider the system with a fixed number of bosons, N. While in this section we are mainly interested in using the Lindbladian Eq. (3.1) to benchmark the framework, in Sec. 4 we investigate its physical properties thoroughly. Physical relevance of the model is manifested in its steady state, which is a lattice analogue of a Bose-Einstein condensate (BEC). As a consequence, it can be used as a dissipative state preparation (DSP) protocol.

3.1 Introduction and general idea

Approximating eigenvalues and eigenvectors of a many-body Lindbladian is a notoriously difficult task. As we have already discussed, its non-Hermiticity prevents the use of the well-established toolbox at one's disposal when working with unitary dynamics [25, 26, 98]. For general Lindbladians we know from Sec. 2.1 that the steady state can be approximated via a long time evolution, since $\hat{\rho}_{\text{ss}} = \lim_{t\to\infty} \hat{\rho}(t)$. Note the similarity to imaginary-time evolution in unitary systems, where the ground-state manifold spans the fixed point of (imaginary) time evolution.

For the Lindbladian, we can expand the time evolution of an arbitrary vectorized initial state $|\rho\rangle\rangle$ in the eigenbasis of the Lindbladian as

$$|\rho(t)\rangle\rangle = \mathrm{e}^{\hat{\mathcal{L}}t} |\rho\rangle\rangle = |\rho_{\text{ss}}\rangle\rangle + \sum_{k=2}^{D^2} \mathrm{e}^{\lambda_k t} \langle\langle l_k | \rho_0 \rangle\rangle \, |r_k\rangle\rangle \ , \tag{3.2}$$

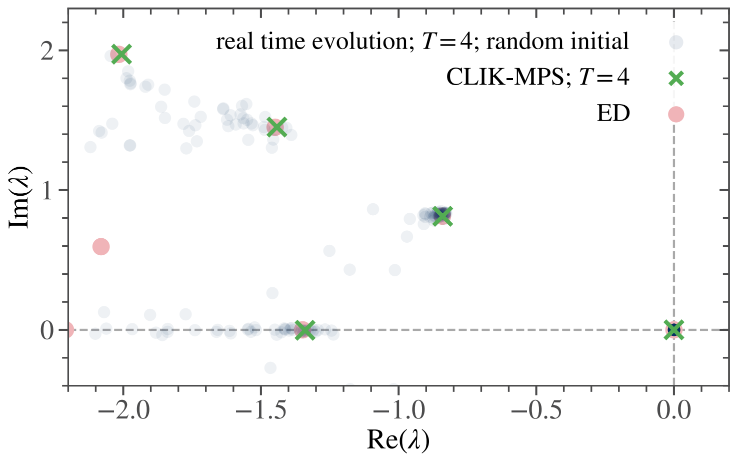

Figure 3: Impact of the initial state on the approximated spectrum of the system specified by Eq. (3.1), adapted from [2]. We compare ED data to the spectrum from a Krylov method with a single real-time evolution and a randomly sampled initial state [110]. In total, 50 initial states were generated, and increasing darkness of the blue shade indicates a higher density of approximated eigenvalues from different initial states. Additionally the results from CLIK-MPS are shown. We considered 5 sites and 4 particles, all other parameters are specified in Fig. 6.

where λ_k are the eigenvalues of $\hat{\mathcal{L}}$, $|r_k\rangle\rangle$ ($|l_k\rangle\rangle$) the corresponding right (left) eigenvectors, and $D = \dim \mathcal{H}$ denotes the dimension of the Hilbert space of the underlying physical system. Here, the contribution from every right eigenvector decays exponentially in time with a rate $-\mathrm{Re}(\lambda_k)$, which also implies that the contribution of the steady state $|\rho_{\mathrm{ss}}\rangle\rangle$ has no time dependence. As we discussed in Sec. 2.5, this time-evolution can be computed efficiently using TN methods, and the computational complexity depends mostly on the bond dimensions, which, in the worst case, increase exponentially at short times. Nevertheless, since contributions from eigenvalues with large absolute real part decay fast, the states at intermediate times contain information about the low-lying spectrum. This observation leads to the insight that the low-lying spectrum should be well approximated within a Krylov space spanned by time-evolved states, which was used by Minganti and Huybrechts in 2022 [110] to approximate steady states and the dissipative gap for Lindbladians. However, their method was based on ED and limited to small system sizes and had problems approximating higher excited eigenvalues.

In Fig. 3, we show the results of the previously introduced procedure for the paradigmatic dissipative Bose-Hubbard Lindbladian Eq. (3.1). We fix the timestep of the state sampling $\delta t = 0.1$ (which we call the sampling interval) and maximal evolution time $T = 4$ and consider the Krylov spaces generated by the time evolution of a single randomly generated initial state. This Krylov space consequently features 40 time-evolved states. The resulting spectra are shown for 50 such initializations (blue dots), in comparison to the exact spectrum (pink dots) obtained by ED. The darker the shade of blue, the more eigenvalues from different initial states lie at the respective position. While the steady state eigenvalue (λ_1) is approximated well for all initializations, already the slowest decaying mode shows minor fluctuations. If we are interested in higher excited states, the Krylov method is not conclusive and the individual initial states yield completely different eigenvalues.

This motivates that we first need to substantially refine the method before we move on to large-scale calculations. We do so by considering complex-time evolutions, where we evolve according to a contour $z(t) \in \mathbb{C}$. By the nature of the Lindbladian spectrum, complex-time evolution enhances specific parts of the spectrum compared to real-time evolution. Importantly, we find that it enhances a part of the low-lying spectrum by decreasing its decay rates, which makes it very useful for our framework. By combining real and complex-time-evolved states into a larger Krylov space, we benefit from the strengths of both time evolutions as we discuss in Sec. 3.2.2. Additionally, Fig. 3 suggests that an optimized initial state is important for the accuracy of the method, which is why we implement physically motivated warm-up procedures to find good initial states. Here, a crucial ingredient is the insight that traceless states are orthogonal to the steady state sector, and thus they converge to the slowest decaying mode during time evolution, instead of the steady state. We therefore propose to use a traceless initial state for the complex-time evolution, with the intention of getting a large overlap with slowly decaying modes, while real-time evolving a physical state and obtaining a large overlap with the steady state.

Combining all of these novelties, we end up with the complex-time Lindbladian Krylov subspace MPS (CLIK-MPS) framework. We show its improvements in approximating the Lindbladian spectrum in Fig. 3, with the same maximal time and sampling interval as for the simple Krylov space from a single time evolution discussed above. We find excellent agreement with the ED spectrum, indicating the efficacy of the introduced adjustments.

3.2 Detailed walkthrough of CLIK-MPS

In this section we aim to provide a detailed discussion of the theoretical and numerical novelties behind CLIK-MPS. We also present the implementation of the framework in a concise way. This includes the Krylov diagonalization in Sec. 3.2.1, where we also discuss how to avoid numerical issues that naturally arise when performing diagonalizations up to eigenvalues near machine precision. Next, we provide detailed insights into the importance of complex-time evolutions to efficiently target slowly decaying modes in Sec. 3.2.2. We also discuss how to adapt the framework to target left eigenmodes in Sec. 3.2.3. All this is accompanied by a physically motivated warm-up procedure in Sec. 3.2.4, which significantly increases the capabilities of the method. We also dive into the problem of performing arithmetic in the Krylov basis in Sec. 3.2.5: We aim at a full description of overlaps and expectation values inside the Krylov space, surpassing numerically costly MPS arithmetics. This makes large-scale calculations even possible, and we also discuss how to bring knowledge about symmetries into the Krylov space and ensure physicality of the approximated states. Lastly, we briefly discuss the generalization of CLIK-MPS to the non-Markovian setting in Sec. 3.2.6.

3.2.1 Constructing the Krylov subspace

As we already motivated in Sec. 3.1, we start from a Krylov space which is spanned by time-evolved states given by Eq. (3.2). Since states at late times mostly feature contributions from slowly decaying modes (i.e. the low-lying eigenvalues), the Krylov space approximates these eigenvalues and eigenvectors. Rigorously speaking, we are interested in the Krylov space [110, 56]

$$\mathcal{K}_0(\rho_0) = \mathrm{span}\big\{|\rho_0\rangle\!\rangle,\ \exp(\hat{\mathcal{L}}\,\delta t)|\rho_0\rangle\!\rangle,\ \dots\ (\exp(\hat{\mathcal{L}}\,\delta t))^{N^K-1}|\rho_0\rangle\!\rangle\big\}\ , \tag{3.3}$$

where δt is the sampling interval and N^K the number of time-evolved states, such that the maximal evolved time T is given by $T = N^K\delta t$. The remaining task is to represent the Lindbladian in this Krylov space. To do so, we first need to build an orthonormal basis (ONB) of the Krylov space, since the time-evolved states are not orthogonal.

To circumvent explicitly constructing the MPS representations of the ONB, we calculate the Gram matrix as in [56]. If we denote the non-orthonormal basis states of the Krylov space $\mathcal{K}$ by

$\left\{|\rho_j\rangle\!\rangle\right\}_j$ (which are given by the time-evolved states) the Gram matrix is given by $\mathbf{M}_{ij} = \langle\!\langle\rho_i|\rho_j\rangle\!\rangle$. After diagonalizing $\mathbf{M} = \mathbf{U}\mathbf{S}\mathbf{U}^\dagger$ a transformation $\mathbf{X}$ into an ONB $|e_m\rangle\!\rangle$ is given by

$$\mathbf{X} = \mathbf{U}\mathbf{S}^{-1/2} , \qquad |e_m\rangle\!\rangle = \sum_{j=1}^{N^K} \mathbf{X}_{jm}|\rho_j\rangle\!\rangle \, . \tag{3.4}$$

We stress that inverting the square roots of the eigenvalues of $\mathbf{M}$ is a numerically delicate operation, as the time-evolved states are almost linearly dependent. However, using a recursive factorization [115, 56], the numerical precision of the computed eigenvalues can be improved to arbitrary precision such that eventually only the linear dependency of columns or rows of $\mathbf{U}$ imposes constraints. The main idea for the recursive factorization is to diagonalize the matrix, keep the eigenvalues above a threshold η (we chose $\eta = 10^{-4}$) and repeat the steps in the subspace spanned by the discarded eigenvectors with the rescaled matrix. To avoid linear dependencies, we discard eigenvalues and eigenstates of $\mathbf{M}$ featuring eigenvalues below a given threshold $\epsilon = 10^{-14}$. The corresponding rows and columns are removed in $\mathbf{S}$ and $\mathbf{U}$. The calculation of $\mathbf{X}$ is a numerically stable operation, which is imperative for the Krylov diagonalization to work reliably. While the initial non-orthonormal basis featured N^K states, the constructed ONB may be composed of less states D^K due to linear dependent contributions. Consequently, while $\mathbf{M} \in \mathbb{C}^{N^K \times N^K}$, the transformation satisfies $\mathbf{X} \in \mathbb{C}^{N^K \times D^K}$.

Once we have obtained $\mathbf{X}$, we can easily represent the Lindbladian in the corresponding orthonormal eigenbasis by computing the matrix elements $\mathbf{L}_{ij} = \langle\!\langle\rho_i|\hat{\mathcal{L}}|\rho_j\rangle\!\rangle$ and transforming into the ONB by

$$\mathbf{L}^{\text{eff}} = \mathbf{X}^\dagger \mathbf{L} \mathbf{X} \, , \tag{3.5}$$

such that $\mathbf{L}^{\text{eff}} \in \mathbb{C}^{D^K \times D^K}$. The effective Lindbladian $\mathbf{L}^{\text{eff}}$ can be diagonalized using standard routines. This yields eigenvalues λ_k, a matrix of right (left) eigenvectors $\mathbf{R}$ ($\mathbf{L}$), and we sort their columns such that the k-th eigenvector corresponds to the approximation of the k-th eigenvalue.

Besides calculating expectation values and overlaps, we avoid numerically costly MPS-addition. By this strategy, we map the Krylov space spanned by MPS states onto an abstract vector space $\mathbb{C}^{D^K}$, and directly performing computations in the new vector space is much more efficient. In Sec. 3.2.5 we use these insight to efficiently compute overlaps and expectation values of arbitrary operators in the abstract Krylov representation.

We can always transform a state in the abstract Krylov vector space back into the original MPS representation. For instance, the MPS representation of the right eigenvectors of the effective Lindbladian are given by

$$|r_k\rangle\!\rangle = \sum_{m=1}^{D^K} \mathbf{R}_{mk}|e_m\rangle\!\rangle = \sum_{l=1}^{N^K} [\mathbf{X}\mathbf{R}]_{lk} \, |\rho_l\rangle\!\rangle \, , \tag{3.6}$$

where we used the representation of the ONB from Eq. (3.4). A pseudocode summarizing the procedure to diagonalize the Lindbladian inside the Krylov space is provided in Algorithm 1. Note that the calculation of $\mathbf{G}$ and $\mathbf{L}^{\text{eff}}$ can be parallelized, since each overlap and expectation is independent of the others.

Algorithm 1 Krylov subspace diagonalization

```
procedure KRYLOV_LINDBLADIAN($\{|\rho(t_i)\rangle\rangle\}_i$, $\epsilon$)
    $\mathbf{L} \leftarrow$ Lindbladian matrix elements $\langle\langle\rho(t_i)|\hat{\mathcal{L}}|\rho(t_j)\rangle\rangle$
    $\mathbf{M} \leftarrow$ Gram matrix $\langle\langle\rho(t_i)|\rho(t_j)\rangle\rangle$
    $\mathbf{S}$, $\mathbf{U} \leftarrow$ diagonalized Gram matrix $\mathbf{M}$ and discard eigenvalues smaller than $\epsilon$
    $\mathbf{X} \leftarrow \mathbf{U}\mathbf{S}^{-1/2}$                                    ▷ trafo into ONB
    $\mathbf{L}^{\text{eff}} \leftarrow \mathbf{X}^{\dagger}\mathbf{L}\mathbf{X}$                                    ▷ Action on ONB
    return $\{\lambda_i, \mathbf{r}^i\}_i$, $\mathbf{X} \leftarrow$ spectral decomp. of $\mathbf{L}^{\text{eff}}$
end procedure
```

It is important to note that using this approach, we effectively describe density operators with a much higher bond dimension than the one actually used during the numerics. We are thus interested in the bond dimension we can maximally reach within the Krylov space, which we term the effective bond dimension χ_{eff}. A connection to the bond dimensions $\chi(\psi)$ of the initial time-evolved states and Eq. (3.21) can be derived by a simple counting argument. Note that we always define $\chi(\psi)$ as the largest dimension of a state ψ's set of virtual legs. Using this convention, the bond dimensions of the time-evolved density operator at time step t_i is given by $\chi(|\rho(t_i)\rangle\rangle) = \chi_i$. If we would construct the MPS representation of the orthonormal basis states of $\mathcal{K}$ explicitly according to Eq. (3.21), we would need to successively perform MPS additions. As we have already discussed in Sec. 2.5, the bond dimensions in general add upon MPS addition. The maximally expressible bond dimension χ_{eff} within the Krylov space is therefore approximately

$$\chi_{\text{eff}} \sim \sum_{j=1}^{N^K} \chi_j \leq N^K \max_j \chi_j \, . \tag{3.7}$$

Later, we will construct Krylov spaces with $N^K \sim \mathcal{O}(100)$, i.e., we approximate the Lindbladian in a Krylov space whose basis states would be represented by MPS with bond dimensions exceeding those of the time-evolved states by more than two orders of magnitude. Note that this insight shows a systematic benefit, as we are able to describe states which have much higher entanglement than the original time-evolved states. Thus, we expect the framework to be robust to truncation during time evolution. This provides an intuitive explanation for the excellent precision of CLIK-MPS we observed during our simulations for the steady state as well as the low-lying eigenvalues and eigenmodes of the Lindbladian. Note that this argument is corroborated by numerical results in Sec. 3.3.2.

Eq. (3.7) unfortunately implies that brute force building the MPS representation of the approximated eigenstates will result in the poor scaling $\mathcal{O}\big(L(\chi_{\max}N^K)^3\big)$ when calculating overlaps or expectation values. Crucially, we find ways to reduce this scaling to $\mathcal{O}\big(L\chi_{\max}^3 N^K\big)$ by calculating overlaps and expectation values directly inside the Krylov space in Sec. 3.2.5.

Regardless of the high reachable bond dimensions, Fig. 3 proved that a single real-time evolution is not sufficient to accurately resolve slowly decaying eigenvectors. We conclude, that we need to refine the Krylov space to reliably approximate the low-lying spectrum.

3.2.2 Role of complex-time evolution

As we have seen in Fig. 3, real-time evolutions are not sufficient to span a Krylov space which reliably approximates low-lying eigenmodes. This is partially due to the problem that contributions from low-lying eigenvalues are suppressed exponentially, leading to a poor representation by time evolved states. We would like to alter the exponential decay of the slow decaying modes to better represent them inside the Krylov space. To achieve this objective, there are two methodological improvements, one of which we will introduce in this section.

In strong analogy to the unitary case, we want to employ complex-time evolution, that is, use a complex-time variable into the exponent of Eq. (3.8) instead of a real one. In unitary systems, this proves to be a very viable approach to target the low-lying eigenvalues, and has been used to calculate the low energy behavior of Greens functions [116, 56].

In the open system case complex-time evolution has other benefits, since the spectrum of the Lindbladian is fundamentally different from the unitary case. We can start by directly looking at the time evolution with a complex-time z in the eigenbasis of the Lindbladian

$$|\rho(z)\rangle\!\rangle = \mathrm{e}^{\hat{\mathcal{L}}z}|\rho_0\rangle\!\rangle = |\rho_{\mathrm{ss}}\rangle\!\rangle + \sum_{k=2}^{D^2} \mathrm{e}^{\lambda_k z}\langle\!\langle l_k|\rho_0\rangle\!\rangle |r_k\rangle\!\rangle \,. \tag{3.8}$$

To extract the damping rate, we need to bring the decaying part of the exponential prefactors into the form $\exp\big(-\xi_k|z|\big)$. This fixes the damping rate ξ_k for λ_k as

$$\xi_k = -\frac{1}{|z|}\operatorname{Re}\big(\lambda_k z\big) = -\operatorname{Re}(\lambda_k)\cos(\alpha(t)) - \operatorname{Im}(\lambda_k)\sin(\alpha(t))\,, \tag{3.9}$$

where we introduced the parametrization of the contour as $z(t) = \mathrm{e}^{\mathrm{i}\alpha(t)}|z(t)|$. We can interpret this result better by inserting the polar decomposition of the eigenvalue $\lambda_k = |\lambda_k|\mathrm{e}^{\mathrm{i}\phi_k}$. Now with a little bit of algebra, we find

$$\xi_k = -\operatorname{Re}(\lambda_k)\,\frac{\cos(\alpha(t)-\phi_k)}{\cos(\phi_k)}\,. \tag{3.10}$$

Eq. (3.10) reveals that the damping rate does not depend on the full contour, but only on the complex angle $\alpha(t)$. Furthermore, it shows how the dampening changes compared to the case of a real-time evolution, where it is given by $\xi_k = -\operatorname{Re}(\lambda_k)$. Fixing a value of $\alpha(t)$, eigenvalues whose decay is the same as for $\alpha = 0$ satisfy $\cos(\alpha(t)-\phi_k) = \cos(\phi_k)$, which shows that eigenvalues having $\phi_k < \alpha(t)/2 + \pi$ are enhanced (i.e. feature lower damping rate $\xi_k < -\operatorname{Re}(\lambda_k)$). On the other hand, if $\phi_k > \alpha(t)/2 + \pi$ the eigenmode is suppressed. This means that states evolved under a contour with $\alpha(t) > 0$ feature higher weight on the eigenvalues with $\operatorname{Im}(\lambda_j) > 0$ than real-time-evolved states ($\alpha(t) = 0$).

We can also translate this into the spectral picture, where the dampening gets a geometrical meaning and can be visualized graphically. From Eq. (3.8) and (2.3) we can deduce that the state $|\rho(z)\rangle\!\rangle$ and the left eigenmode $|l_k\rangle\!\rangle$ have the overlap

$$\Big|\langle\!\langle l_k|\rho(z)\rangle\!\rangle\Big| \sim \mathrm{e}^{\operatorname{Re}(z\lambda_k)} \equiv \mathrm{e}^{-\xi_k t}\,. \tag{3.11}$$

Let us now consider the linearly inclined complex-time contours $z(t) = t\mathrm{e}^{-\mathrm{i}\alpha}$ with $\alpha > 0$ as shown in Fig. 4a. In this case, Eq. (3.11) and Eq. (3.10) suggest that the damping rate is given by the projection of the eigenvalue λ_k onto the complex conjugated contour z^*. Indeed, we can connect the scalar product in the complex plane, seen as a real vector space $\mathbb{R}^2$, with the complex numbers themselves by

$$\begin{pmatrix}\operatorname{Re}\lambda & \operatorname{Im}\lambda\end{pmatrix} \bullet \begin{pmatrix}\operatorname{Re} z^* \\ \operatorname{Im} z^*\end{pmatrix} = \operatorname{Re}\big(z\lambda\big)\,, \tag{3.12}$$

where $\bullet$ denotes the *real* scalar product. This reveals that the damping rate ξ_k is given by the projection onto the line z^*, as depicted in Fig. 4a, and lines of constant damping are orthogonal to

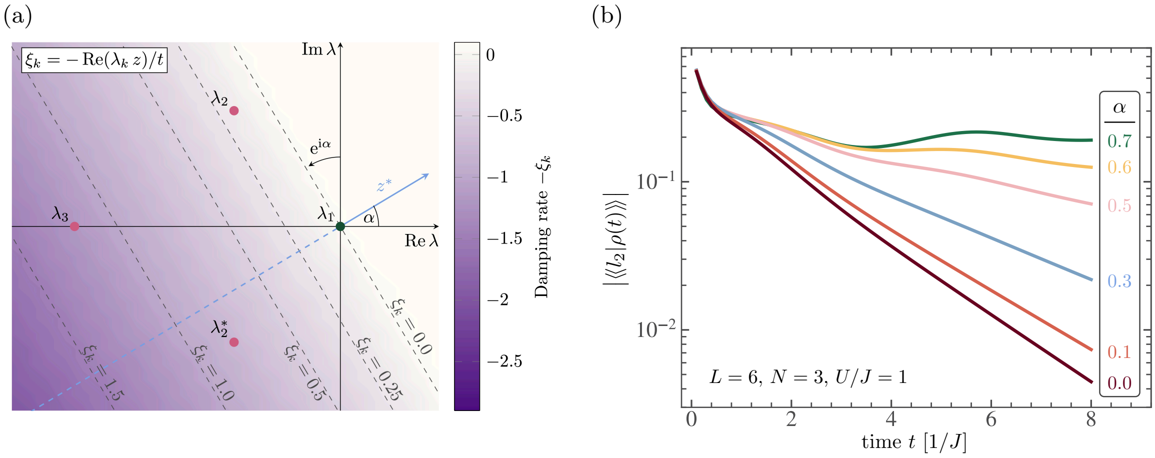

Figure 4: Panel a): Effect of linearly inclined complex-time contours $z = te^{-i\alpha}$ on the damping rates ξ_k (see Eq. (3.9)), adapted from [2]. The color shading indicates the damping rate $\xi_k = -\operatorname{Re}(\lambda_k\, z)/t$ for an eigenvalue λ_k when evolving along the contour $z(t)$. The contour lines ξ_k = const. are tilted and lie orthogonal to z^* (solid blue line, c.f. Eq. (3.12)). Panel b): Overlap of a density matrix $|\rho(t)\rangle\rangle$ with the slowest decaying mode $|l_2\rangle\rangle$ during time evolution for multiple angles α (c.f. Eq. (3.11)). The eigenmode lies at $\lambda_2 = -0.517 + 0.592\mathrm{i}$, and consequently the damping rate is lowered when increasing angle α. At $\alpha = 0.7$ the angle is comparable to $\phi_2 - \pi/2 = 0.71$, and the damping rate completely vanishes in accordance to Eq. (3.10). We considered the dissipative Bose-Hubbard Lindbladian Eq. (3.1) for 6 sites and 3 bosons at $\kappa = U = J = 1$.

the path followed by the complex conjugated contour $z^*(t)$. For any finite tilt angle $\alpha > 0$, these lines are rotated counterclockwise and therefore slow down the damping of excited eigenmodes, if $\phi_k < \alpha/2 + \pi$, as discussed above. Since the Lindbladian modes come in complex conjugate pairs, it suffices to accurately determine, for instance, those eigenvalues λ_k with a positive imaginary part, and the whole spectrum is retrieved by complex conjugation. In the following, we typically consider positive angles $\alpha > 0$.

Nevertheless, one has to be careful with choosing the complex angle. As Eq. (3.10) shows, if $\phi_k < \frac{\pi}{2} + \alpha$, the damping rate changes sign and the corresponding mode is exponentially enhanced. This leads to major instabilities in the time evolution, since bulk states with a low angle ϕ_k get enhanced strongly due to the linear dependence of ξ_k on $-\operatorname{Re}(\lambda_k)$. To mitigate these problems, one should always choose

$$\alpha \ll \min_{\phi_k:\, \operatorname{Re}(\lambda_k) < \operatorname{Re}(\lambda_{i_0})} \left(\phi_k - \frac{\pi}{2}\right) , \tag{3.13}$$

where λ_{i_0} is the largest eigenvalue we want to approximate. In practice, this is achieved by starting time evolutions with multiple angles and checking if the norm of the time-evolved state increases exponentially. If this is the case for some angle α_{crit}, the sign of the damping rate ξ_k has changed sign for some eigenvalue λ_k, which is a clear sign that the angle α_{crit} is chosen to high. Then, we just choose some angle $\alpha \ll \alpha_{\text{crit}}$.

In Fig. 4b, we numerically test the effect of complex-time evolution given in Eq. (3.11), by reproducing the dependence of the decay rate on the complex angle. We present the overlap of a time-evolved density matrix with the slowest decaying mode $|l_2\rangle\rangle$, which has a complex eigenvalue $\lambda_2 = -0.517 + 0.592\mathrm{i}$. With increasing angle α, the exponential decay is slowed down, which is in agreement with the damping rate ξ_k in Eq. (3.10). Note that if $\alpha \to \phi_2 - \pi/2$ the damping rate completely vanishes, as seen for $\alpha = 0.7$, which is near the eigenvalue angle $\phi_2 - \pi/2 = 0.71$ in accordance to Eq. (3.10).

In the same spirit as for real-time evolution in Eq. (3.3), we can evolve an initial state $|\rho_\alpha\rangle\!\rangle$ with a complex-time evolution along a contour with angle α and collecting the states with a sampling interval $\delta z = \mathrm{e}^{-\mathrm{i}\alpha}\delta t$ to produce a Krylov space

$$\mathcal{K}_\alpha(\rho_\alpha) = \mathrm{span}\big\{|\rho_\alpha\rangle\!\rangle,\ \exp(\hat{\mathcal{L}}\,\delta z)|\rho_\alpha\rangle\!\rangle,\ \ldots\ (\exp(\hat{\mathcal{L}}\,\delta z))^{N^K-1}|\rho_\alpha\rangle\!\rangle\big\}\,. \tag{3.14}$$

Our analysis suggests, that the Krylov space $\mathcal{K}_\alpha(\rho_\alpha)$ should approximate the slowly decaying modes with positive imaginary part well. To additionally approximate the steady state well, we combine a real-time evolution with initial state $|\rho_0\rangle\!\rangle$ with a complex-time evolution of another state $|\rho_\alpha\rangle\!\rangle$, resulting in the full Krylov space

$$\mathcal{K}_{0,\alpha} = \mathcal{K}_0(\rho_0) \oplus \mathcal{K}_\alpha(\rho_\alpha)\,. \tag{3.15}$$

Crucially, the two time evolutions can be performed in parallel. We want to stress that the two initial states $|\rho_0\rangle\!\rangle$, $|\rho_\alpha\rangle\!\rangle$ should be chosen differently, as it lowers the linear dependency of the Krylov vectors. Note that we typically only specify the non-zero angle when providing explicit parameters used in a numerical calculation, as we always additionally consider a real-time evolution.

3.2.3 Targeting left eigenmodes

As we established in Sec. 3.2.1 and 3.2.2, the Krylov basis constructed using time-evolved states features high overlap with the slowly decaying *right eigenvectors*, as seen from Eq. (3.8). Since the Lindbladian is non-Hermitian, its left eigenmodes are different from the right ones. Thus, while the low-lying right eigenvectors might be well approximated with the Krylov space Eq. (3.15), the left ones are in general not.

To resolve this issue, we would like to swap the places of the left and right eigenmodes in the decomposition Eq. (3.8). We can do so by considering not the Lindbladian itself, but its Hermitian conjugate $\hat{\mathcal{L}}^\dagger$. The key idea is that the left eigenvectors of the Lindbladian are actually the right eigenvectors of $\hat{\mathcal{L}}^\dagger$. In more detail, the spectral decompositions of the two operators are linked through

$$\hat{\mathcal{L}} \to \hat{\mathcal{L}}^\dagger \quad \text{implies} \quad \big\{\lambda_k, \hat{l}_k, \hat{r}_k\big\}_k \to \big\{\lambda_k^*, \hat{l}_k^\dagger, \hat{r}_k^\dagger\big\}_k\,. \tag{3.16}$$

As a consequence, the time evolution generated by $\hat{\mathcal{L}}^\dagger$ can be written in the original eigenbasis of $\hat{\mathcal{L}}$ as

$$|\rho^*(z)\rangle\!\rangle = \mathrm{e}^{\hat{\mathcal{L}}^\dagger z}|\rho_0\rangle\!\rangle = \sum_{k=1}^{D^2} \mathrm{e}^{\lambda_k^* z}\langle\!\langle r_k|\rho_0\rangle\!\rangle|l_k\rangle\!\rangle\,, \tag{3.17}$$

where ρ^* indicates that the dynamics is generated by $\hat{\mathcal{L}}^\dagger$. The adjoint Lindbladian can easily be represented as a linear operator on the vectorized density matrices as

$$\hat{\mathcal{L}}^\dagger = \mathrm{i}\hat{H} \otimes \hat{\mathbb{1}} - \hat{\mathbb{1}} \otimes \mathrm{i}\hat{H}^{\mathrm{T}} + \sum_l \hat{L}_l^\dagger \otimes \hat{L}_l^{\mathrm{T}} - \frac{1}{2}\hat{L}_l^\dagger\hat{L}_l \otimes \hat{\mathbb{1}} - \frac{1}{2}\hat{\mathbb{1}} \otimes \Big(\hat{L}_l^\dagger\hat{L}_l\Big)^{\mathrm{T}}\,. \tag{3.18}$$

The resulting Krylov space $\mathcal{K}_0^*(\rho_0)$ spanned by these states now includes contributions mainly from the slowly decaying *left* eigenmodes, which is exactly what we are interested in. Again, we utilize two time evolutions and build the Krylov space $\mathcal{K}_{0,\alpha}^* = \mathcal{K}_0^*(\rho_0) \oplus \mathcal{K}_\alpha^*(\rho_\alpha) \oplus \{|\mathbb{1}\rangle\!\rangle\}$. We added the vectorized identity because $\hat{l}_1 = \hat{\mathbb{1}}$ as discussed in Sec. 2.1. Notice that this is the case for a unique steady state, but a similar result holds for multiple steady states as shown in Sec. 2.3. Directly adding the steady state of the conjugate time evolution into the Krylov space by hand increases the approximation quality of the slowly decaying eigenvectors.

3.2.4 Initialization of states

The initial state remains an important input for spanning a good Krylov space. For the framework to perform reliably, it must be chosen carefully and according to a systematic strategy. We thus aim at finding physically motivated warm-up procedures to generate good initial states. In Sec. 3.2.1, 3.2.2 and 3.2.3 we encountered three different types of time evolutions, which all have varying demands on an optimal initial state. While for the real-time evolution with $\hat{\mathcal{L}}$ we want to maximize the initial overlap with the steady state, the complex-time evolutions with $\hat{\mathcal{L}}$ should target the slowly decaying modes. Lastly, for the left eigenmodes we need a large overlap with the slowly decaying modes, since we already know the left eigenvector $|l_1\rangle\rangle$ when time evolving with $\hat{\mathcal{L}}^\dagger$.

As previously discussed, for the complex-time evolution with $\hat{\mathcal{L}}$, we would like to find initial states which are orthogonal to the steady state sector in order to maximize the overlap with the slowly decaying modes. This is indeed possible since orthogonalizing w.r.t. the steady state sector means orthogonalizing w.r.t. the corresponding left eigenmode. Since we know that the left eigenmode $\hat{l}_1$ is the vectorized identity on the whole space (or on irreducible blocks of the symmetry for strong symmetries), traceless states $|\rho^{\mathrm{u}}\rangle\rangle$ (lying in a single block) are orthogonal w.r.t. all steady states. If we normalize during time evolution, this state will approach the slowest decaying mode instead of a steady state with the asymptotic scaling

$$\left|\langle\langle l_2|\rho^{\mathrm{u}}(z)\rangle\rangle\right| \sim 1 - \mathcal{O}\Big(\exp\big(-t \max_{k>2} \xi_k - \xi_2\big)\Big) , \tag{3.19}$$

where the exponent is just the gap between the damping rates of the slowest decaying mode and the second-slowest. This behavior can be seen in Figure 5a, where we consider the Bose-Hubbard Lindbladian Eq. (3.1) with 20 sites and 10 bosons. While a physical state $|\rho^{\mathrm{p}}\rangle\rangle$ converges to the steady state $|r_1\rangle\rangle$ fast (upper panel), the overlap of the traceless initial state $|\rho^{\mathrm{u}}\rangle\rangle$ with $|r_1\rangle\rangle$ stays much lower. On the other hand, the overlap with the slowest decaying mode $|r_2\rangle\rangle$ (lower panel) decays quickly for the physical state, while it increases up to 0.8 for the traceless initialization. The oscillations in the overlap $\left|\langle\langle r_2|\rho^{\mathrm{u}}(t)\rangle\rangle\right|$ originate from the imaginary part of λ_2 and the frequency agrees with $\mathrm{Im}(z\lambda_2)/t$ as expected.

However, the overlap of $|\rho^{\mathrm{u}}\rangle\rangle$ with $|r_2\rangle\rangle$ does not converge to one as suggested by Eq. (3.19), and the maxima even slightly decrease over time. This is well understood when taking into account truncation, which is performed during time evolution as discussed in Sec. 2.5. In each step, the truncation leads to the emergence of components which have overlap with the steady state sector. These are exponentially enhanced due to the normalization of the time-evolved states. Thus, if we denote the truncation error by $\epsilon_{\mathrm{trunc}}$, the overlap with the steady state sector behaves as

$$\left|\langle\langle l_1|\rho^{\mathrm{u}}(z)\rangle\rangle\right| \sim \epsilon_{\mathrm{trunc}}\, \mathrm{e}^{\xi_2 t} . \tag{3.20}$$

The exponent depends on ξ_2, suppressing the exponential increase in truncation error when considering higher angles α.

Now that we clarified the demands on the different initializations, we can move on and propose warm-up procedures. We present them in a general fashion, so that they do not depend strongly on the specific Lindbladian. Nevertheless, as we mostly consider the dissipative Bose-Hubbard Lindbladian in this work, we give detailed descriptions on tailoring the procedure to the

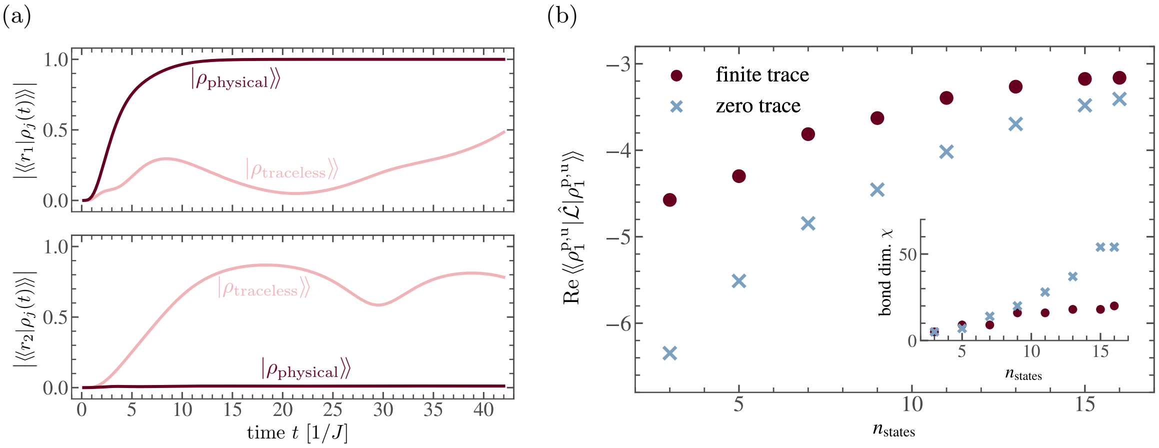

Figure 5: Panel a): Overlap of two initial states with $|r_1\rangle\rangle$ (upper panel) and $|r_2\rangle\rangle$ (lower panel). We test optimized physical ($|\rho_{\text{physical}}\rangle\rangle$) and traceless ($|\rho_{\text{traceless}}\rangle\rangle$) states for a dissipative Bose-Hubbard model with 20 sites and 10 bosons at $\kappa/J = 2$ and $U/J = 0.5$. While the physical state converges exponentially to $|r_1\rangle\rangle$ (upper panel), the traceless state remains at comparably low overlap with $|r_1\rangle\rangle$. On the other hand, the traceless state has exponentially higher overlap with $|r_2\rangle\rangle$ than the physical one (lower panel). Panel b): Initial states optimized via the warm-up procedure for a dissipative Bose-Hubbard model Eq. (3.1) with $L = 10$ sites and $N = 5$ particles, setting $J = U = \kappa = 1$, adapted from [2]. We perform a search up to $n_{\text{states}} = 16$ and compute $\langle\langle\rho_1^{\text{p,u}}|\hat{\mathcal{L}}|\rho_1^{\text{p,u}}\rangle\rangle$ for the optimal basis in every iteration, both for finding a physical initial state (red dots) and a traceless initial state (blue crosses). Inset: Corresponding maximal bond dimensions of the respective states $|\rho_1^{\text{p,u}}\rangle\rangle$.

specific case. The efficient initialization of states requires two different optimization protocols, which we discuss below.

Starting with the *real-time* evolution with $\hat{\mathcal{L}}$, we are interested in capturing the steady state and the slowest decaying modes efficiently, and we therefore search for an initial state exhibiting a large overlap with the low-lying eigenmodes. This is implemented by minimizing the real part of the expectation value and variance of the Lindbladian on a subspace spanned by stochastically chosen states. The resulting routine is summarized in Algorithm 2. The random subspace is initialized by a product state $|\psi_0\rangle = |n_1, n_2, \ldots, n_L\rangle$ on the physical lattice, which is appended to a list S. Then, $n_{\text{samples}} - 1$ different states are generated stochastically. In this step, the specific form of the Lindbladian is important, as the sampled states should feature finite transition rates between each other. For the Bose-Hubbard model, exhibiting a particle number conservation and nearest-neighbor hopping, the algorithm is set up as follows: A state $|\psi\rangle$ is randomly selected from S, together with an index k labeling an occupied site, and a neighboring site $i \in k \pm 1$. The new state $\hat{b}^\dagger_{k+i}\hat{b}_k|\psi\rangle$ is appended if it is not already included in S. Depending on the Lindbladian, next nearest neighbor hopping or particle-loss and -creation should be considered in the sampling process. We build a set of vectorized states $R = S \otimes S$, containing all $|\rho\rangle\rangle = |\psi\rangle \otimes |\phi\rangle$ with $|\psi\rangle$ and $|\phi\rangle$ in S, featuring n^2_{samples} different orthonormal states. After calculating the effective Lindbladian action $\mathbf{L}^{\text{eff}}$ on R by $\mathbf{L}^{\text{eff}}_{ij} = \langle\langle\rho_i|\hat{\mathcal{L}}|\rho_j\rangle\rangle$, where $|\rho_i\rangle\rangle$, $|\rho_j\rangle\rangle \in R$, we diagonalize $\mathbf{L}^{\text{eff}}$ and pick the right eigenvector $\mathbf{r}^0$ corresponding to the eigenvalue with smallest absolute real part as our initial state. The algorithm returns the MPS-representation of $\mathbf{r}^0$ given by $|\rho^{\text{p}}\rangle\rangle = \sum_i \mathbf{r}^0_i|\rho_i\rangle\rangle$. To ensure that it is a traceful state, we calculate its trace norm $\langle\langle\mathbb{1}|\rho^{\text{p}}\rangle\rangle$ and repeat the procedure if it is smaller than some threshold ϵ_{trace}.

Algorithm 2 Compute optimal initial state $|\rho^{\mathrm{p}}_1\rangle\rangle$

```
 1: procedure INITIAL_PHYSICAL($|\psi_0\rangle$, $n_{\text{samples}}$)
 2:     $S \leftarrow \big[\, |\psi_0\rangle \,\big]$                ▷ Initialize with the input state
 3:     for $n = 1$ to $n_{\text{samples}} - 1$ do
 4:         $\big\{ |\psi\rangle, k, i \big\} \leftarrow |\psi\rangle$ drawn from $S$, $k$: occupied site in $|\psi\rangle$, $i$: random number $\pm 1$
 5:         $|\tilde{\psi}\rangle \leftarrow \hat{b}^{\dagger}_{k+i}\hat{b}_k |\psi\rangle$
 6:         Check that $|\tilde{\psi}\rangle \notin S$ and append it to $S$, otherwise go back to line 4
 7:     end for
 8:     $R \leftarrow \big[\, |\psi\rangle \otimes |\phi\rangle$ for $|\psi\rangle, |\phi\rangle$ in $S \big]$
 9:     $\mathbf{L}^{\text{eff}} \leftarrow \langle\langle \rho_i | \hat{\mathcal{L}} | \rho_j \rangle\rangle$ for $|\rho_i\rangle\rangle$, $|\rho_j\rangle\rangle$ in $R$
10:     $\lambda_0, \mathbf{r}^0 \leftarrow$ lowest eigenvalue and right eigenvector of $\mathbf{L}^{\text{eff}}$
11:     $|\rho^{\mathrm{p}}\rangle\rangle \leftarrow$ build $\sum_i \mathbf{r}^0_i |\rho_i\rangle\rangle$ for $|\rho_i\rangle\rangle$ in $R$
12:     return $\big\{ |\rho^{\mathrm{p}}\rangle\rangle, S \big\}$ if $\big| \langle\langle \mathbb{1} | \rho^{\mathrm{p}} \rangle\rangle \big| > \epsilon_{\text{trace}}$, else go back to line 3
13: end procedure
```

As we already discussed, the *complex-time* evolution should be initialized with a traceless initial state to approximate the low-lying spectrum best. We can derive a warm-up protocol similar to Algorithm 2, with the only difference that all random states in the set R should be traceless. The corresponding pseudocode is given in Algorithm 3. We again construct the set S in the same fashion as in Algorithm 2. Vectorized states of the form $|\psi\rangle \otimes |\phi\rangle$ with $|\psi\rangle, |\phi\rangle \in S$ are traceless if $|\psi\rangle \neq |\phi\rangle$ and can be appended to R. However, $|\psi\rangle \otimes |\psi\rangle$ has trace one, so we may instead take $|\psi\rangle \otimes |\psi\rangle - |\phi\rangle \otimes |\phi\rangle$ into R. Note that the procedure now produces only $n^2_{\text{samples}} - 1$ states in R. Different from Algorithm 2, these states are not orthonormal, and we need to build an ONB from them. Note that due to the simple structure of the states in R, the Gram matrix is easily constructed analytically. Algorithm 1 then returns the eigenvalues and corresponding right eigenvectors $\{\lambda_i, \mathbf{r}^i\}_i$ of the effective Lindbladian in the Krylov space, as well as the transformation $\mathbf{X}$ into the Krylov-ONB. The right eigenvector $\mathbf{r}^0$ with the lowest $\big|\mathrm{Re}\,\lambda_0\big|$ is again the optimal initial state, and its MPS representation is given by $|\rho^{\mathrm{u}}\rangle\rangle = \sum_i \big[\mathbf{X}\mathbf{r}^0\big]_i |\rho_i\rangle\rangle$.

Algorithm 3 Compute optimal initial state $|\rho^{\mathrm{u}}_1\rangle\rangle$

```
1: procedure INITIAL_TRACELESS($|\psi_0\rangle$, $n_{\text{samples}}$)
2:     $S \leftarrow$ do lines 2 – 7 from Algorithm 2
3:     $R \leftarrow \big[\, |\psi\rangle \otimes |\phi\rangle$ for $|\psi\rangle, |\phi\rangle$ in $S$ if $|\psi\rangle \neq |\phi\rangle \,\big]$
4:     $D \leftarrow \big[\, |\psi\rangle \otimes |\psi\rangle$ for $|\psi\rangle$ in $S \big]$
5:     Append $|\delta_n\rangle\rangle - |\delta_{n+1}\rangle\rangle$ to $R$ for $|\delta_n\rangle\rangle$, $|\delta_{n+1}\rangle\rangle$ in $D$ and $n = 1, \ldots, n_{\text{samples}} - 1$
6:     $\{\lambda_i, \mathbf{r}^i\}_i$, $\mathbf{X} \leftarrow$ do Algorithm 1 with states $R$
7:     $|\rho^{\mathrm{u}}\rangle\rangle \leftarrow$ build $\sum_i \big[\mathbf{X}\mathbf{r}^0\big]_i |\rho_i\rangle\rangle$ for $|\rho_i\rangle\rangle$ in $R$
8:     return $|\rho^{\mathrm{u}}\rangle\rangle$
9: end procedure
```

Although Algorithms 2 and 3 return a good initial state in the stochastically chosen subspace, the chosen subspace itself might not be the best one. Thus, we introduce an iterative extension to the methods, shown in Algorithm 4. Instead of directly building the set S with n_{states} states in a single step, we iteratively enlarge the subspace, adding only a few random states and optimizing this smaller subspace in each iteration. Specifically, given a state list S containing n states, we stochastically generate a new state list S' by adding two states through nearest-neighbor hopping (compare for Algorithms 2 and 3) to S and evaluate the lowest eigenvalue. The exact same process is repeated n_{trial} times (we chose $n_{\text{trial}} = L$) with S and afterwards we chose the one set S' which gave rise to the lowest eigenvalue. This generates a set S of size $n+2$ and the process is repeated. In each iteration, the Lindbladian expectation value is increased, and we terminate the algorithm either if a desired Krylov space dimension is attained, or a threshold bond dimension or expectation value is reached.

Algorithm 4 Iteratively compute optimal initial states $|\rho_1^{\mathrm{p/u}}\rangle\rangle$

```
procedure ITERATE_INITIAL($|\psi_0\rangle$, $n_{\text{samples}}$)
    for $n = 1$ to $n_{\text{samples}}/2$ do
        $|\rho(k)\rangle\rangle,\ S(k) \leftarrow$ Do Algorithm 2 or 3 with input $(S,\ 2)$ for $k = 1, \dots, n_{\text{trial}}$
        $k_{\max} \leftarrow \operatorname{argmax}_k \mathrm{Re}\langle\langle\rho(k)|\hat{\mathcal{L}}|\rho(k)\rangle\rangle$
        $|\rho^{\mathrm{p/u}}\rangle\rangle,\ S \leftarrow |\rho(k_{\max})\rangle\rangle,\ S(k_{\max})$
        if $\chi(\rho^{\mathrm{p/u}}) > \chi_{\max}$ or $\mathrm{Re}\langle\langle\rho^{\mathrm{p/u}}|\hat{\mathcal{L}}|\rho^{\mathrm{p/u}}\rangle\rangle > \epsilon_{\text{treshold}}$ then break
    end for
    return $|\rho^{\mathrm{p/u}}\rangle\rangle$
end procedure
```

Note that the calculation of the effective Lindbladian can be substantially accelerated by reusing the matrix elements from earlier iterations, since in every iteration only 2 basis vectors are added.

In Fig. 5, such an iterative procedure is shown for the dissipative Bose-Hubbard model with 10 sites and 5 particles. The warm-up was performed until $n_{\text{states}} = 16$ for both a traceless and a physical initial state. In every iteration, the real part of the expectation value is increased, which highlights the positive impact of iteratively applying Algorithm 2 and 3 according to Algorithm 4. The corresponding bond dimensions (see inset) increase with n_{states} to about $\chi = 20$ (physical) and $\chi = 60$ (traceless).

For the time evolution with $\hat{\mathcal{L}}^\dagger$, the search for an optimal initial state is not as easily physically motivated. Unfortunately, we do not know the structure of the left eigenvector corresponding to the steady state and orthogonalizing against it is out of reach. Minimizing the expectation value of $\hat{\mathcal{L}}^\dagger$ is nevertheless useful, and we hence use the same algorithms as for the time evolution with $\hat{\mathcal{L}}$. The sole adjustment is that the effective Lindbladian $\mathbf{L}^{\text{eff}}$ has to be replaced by the adjoint effective Lindbladian, whose matrix elements are given by $\langle\langle\rho_i|\hat{\mathcal{L}}^\dagger|\rho_j\rangle\rangle$. For time evolutions with zero complex angle $\alpha = 0$, we use Algorithm 2, whereas for finite angles, Algorithm 3 is employed (both within the iterative extension described in Algorithm 4). The optimal initialization for the adjoint time evolution will be subject to further research.

3.2.5 Efficient subspace arithmetic

As we already discussed in Sec. 3.1, it is numerically costly to calculate the MPS representation of both the steady state and slowly decaying eigenmodes. A crucial objective of CLIK-MPS is to avoid explicitly representing vectorized states and operators in the generated subspaces. Luckily, in most applications, the primary interest lies in overlaps and expectation values of the respective states. The idea is to calculate overlaps and expectation values with the initial time-evolved states. Since they span the Krylov space, suitable superpositions will result in overlaps and expectation values of the approximated right eigenvectors. Note that the calculation of overlaps is very similar to expectation values (chose operator to be the identity, and replace vectorized identity), which is why we first consider efficient expectation values and thereafter generalize to overlaps.

We start by recalling the representation of the right eigenvectors $|r_k^K\rangle\rangle$ obtained in the Krylov space in terms of the initial time-evolved states $|\rho(t_m)\rangle\rangle$ from Eq. (3.6),

$$|r_k^K\rangle\rangle = \sum_{m=1}^{N^K} [\mathbf{XR}]_{mk} \, |\rho(t_m)\rangle\rangle \, . \tag{3.21}$$

Again, we emphasize that Eq. (3.21) should never be evaluated explicitly.

The expectation of an operator $\hat{A}$ can be calculated by first obtaining the vectorized action of $\hat{A}$ on the Krylov basis as $\mathbf{A}_n^{\text{eff}} = \mathrm{Tr}\big(\hat{A}\hat{\rho}(t_n)\big) = \langle\langle \mathbb{1}|\hat{A}|\rho(t_n)\rangle\rangle$ (c.f. Eq. (2.12)) and the normalization $\mathbf{N}_n = \langle\langle \mathbb{1}|\rho(t_n)\rangle\rangle$,

$$\mathrm{Tr}\big(\hat{A}\hat{\rho}_{\text{ss}}\big) = \frac{\langle\langle \mathbb{1}|\hat{A}|r_1\rangle\rangle}{\langle\langle \mathbb{1}|r_1\rangle\rangle} = \frac{\sum_m \langle\langle \mathbb{1}|\hat{A}|\rho(t_m)\rangle\rangle \big[\mathbf{XR}\big]_{m1}}{\sum_k \langle\langle \mathbb{1}|\rho(t_k)\rangle\rangle \big[\mathbf{XR}\big]_{k1}} = \frac{\big[\mathbf{A}^{\text{eff}}\mathbf{XR}\big]_1}{\big[\mathbf{NXR}\big]_1} \, . \tag{3.22}$$

Note that the vectorized identity $|\mathbb{1}\rangle\rangle$ is often well-described by a MPS with moderate bond dimension; in all calculations performed in the scope of this thesis, it did not exceed $\chi \sim 10^3$. Additionally, the calculation of $\mathbf{A}^{\text{eff}}$ can be trivially parallelized, since the expectation values are independent of each other.

Several algorithmic optimizations can be exploited to improve the accuracy of the evaluated expectation value, using algebraic properties of states in the Krylov space. In contrast to real-time evolution, a complex angle leads to a time evolution which does not preserve Hermiticity, due to the asymmetric exponential dampening discussed in Sec. 3.2.2 and visualized in Fig. 4a. As a consequence, the steady state $|r_1^K\rangle\rangle$ from the Krylov space might feature some non-Hermitian artifacts from the complex-time-evolved states. In order to remove them in Eq. (3.22), we can instead insert the Hermitian component of $|r_1^K\rangle\rangle$. It is given by $|r_{1,\text{herm}}^K\rangle\rangle = {}^1\!/_2 \big(|r_1^K\rangle\rangle + |r_1^{K\dagger}\rangle\rangle\big)$, where $|r_1^{K\dagger}\rangle\rangle$ denotes the vectorization of $\big[\hat{r}_1^K\big]^\dagger$. We can make use of the relation

$$\mathrm{Tr}\big(\hat{A}\hat{\rho}^\dagger\big) = \Big(\mathrm{Tr}\big(\hat{A}^\dagger\hat{\rho}\big)\Big)^* = \langle\langle \mathbb{1}|\hat{A}^\dagger|\rho\rangle\rangle^* \, , \tag{3.23}$$

where $\hat{\rho}$ is a general state and $*$ denotes the complex conjugate. Thus, we do not need to calculate $|r_1^{K\dagger}\rangle\rangle$ explicitly, but only need the expectation values $\mathbf{A}_n^{\text{eff},*} = \langle\langle \mathbb{1}|\hat{A}^\dagger|\rho(t_n)\rangle\rangle$ to find

$$\mathrm{Tr}\big(\hat{A}\hat{\rho}_{\text{ss}}\big) = \frac{1}{2\big[\mathbf{NXR}\big]_1}\Big(\big[\mathbf{A}^{\text{eff}}\mathbf{XR}\big]_1 + \big[\mathbf{A}^{\text{eff},*}\mathbf{XR}\big]_1^*\Big) \, . \tag{3.24}$$

With slight changes, Eq. (3.22) and (3.24) can be used to calculate overlaps. Indeed, if we are interested in overlaps of some density matrix $\hat{\rho}$ with a right eigenvector $\hat{r}_k$, we redefine $\mathbf{O}_n^{\text{eff}} = \langle\langle \rho|\rho(t_n)\rangle\rangle$, $\mathbf{O}_n^{\text{eff},*} = \langle\langle \rho|\rho(t_n)\rangle\rangle$ and overlaps are calculated similarly to Eq. (3.22), just discarding the normalization in the denominator

$$\langle\langle \rho|r_k\rangle\rangle = \big[\mathbf{O}^{\text{eff}}\mathbf{XR}\big]_k \, , \tag{3.25}$$

and similarly for Eq. (3.24). To calculate overlaps with the steady state, the normalization needs to be kept.

Exploiting symmetries is a key strategy for improving the efficiency of observable calculations. In Sec. 2.3 we established that steady states of Lindbladians which possess a symmetry always lie in a specific sector associated to an eigenvalue of the corresponding unitary. Since many Lindbladians have symmetries, we would like to incorporate this knowledge into the Krylov space as well. For the moment, we restrict our discussion to $\mathbb{Z}_{N_S}$-symmetries, for which we establish a numerically efficient way of restricting the steady state to the particular symmetry sector. We discuss the generalization to continuous symmetries at the end of the section.

The *discrete symmetry* comes with a generator $\hat{Q}$ and a unitary $\hat{U}$ connected via

$$\hat{U} = \exp\bigl(- 2\pi i\, \hat{Q}\bigr)\ . \tag{3.26}$$

For $\mathbb{Z}_{N_S}$-symmetries, the generator $\hat{Q}$ has spectrum j/N_S for $0 \leq j < N_S$. The corresponding unitary on the vectorized lattice is given by $\hat{\mathcal{U}} = \hat{U} \otimes \hat{U}^*$, and its generator obeys $\hat{\mathcal{Q}} = \hat{Q} \otimes \mathbb{1} - \mathbb{1} \otimes \hat{Q}^{\mathrm{T}}$ (c.f. Sec. 2.3). Note that this directly fixes the spectrum of $\hat{\mathcal{Q}}$.

As we established in Sec. 2.3, each steady state obeys $\hat{\mathcal{Q}}|\rho_{\mathrm{ss}}\rangle\rangle = 0$. Thus, we would like to calculate expectation values for the approximate steady state projected into the correct symmetry subspace, which is given by

$$|\rho_{\mathrm{ss}}^{K,q=0}\rangle\rangle = \hat{\mathcal{P}}_{q=0}|\rho_{\mathrm{ss}}^{K}\rangle\rangle\ , \tag{3.27}$$

where $\hat{\mathcal{P}}_q$ is the projector onto the q-eigenspace of $\hat{\mathcal{Q}}$. Crucially, this projector can be written as a polynomial of order $N_S - 1$ in $\hat{\mathcal{U}}$ through its discrete Fourier transformation,

$$\hat{\mathcal{P}}_q = \frac{1}{N_S} \sum_{n=0}^{N_S-1} \mathrm{e}^{2\pi \mathrm{i} q n}\, \hat{\mathcal{U}}^n\ . \tag{3.28}$$

Now we insert the symmetrized approximate steady state $\hat{\mathcal{P}}_{q=0}|\rho_{\mathrm{ss}}^{K}\rangle\rangle$ into the observable

$$\begin{aligned}\mathrm{Tr}\bigl(\hat{A}\hat{\rho}_{\mathrm{ss}}\bigr) &= \langle\langle \mathbb{1}|\hat{A}\hat{\mathcal{P}}_{q=0}|\rho_{\mathrm{ss}}^{K}\rangle\rangle \\ &= \frac{1}{N_S}\sum_{n=0}^{N_S-1} \langle\langle \mathbb{1}|\hat{\mathcal{U}}^n(\hat{\mathcal{U}}^\dagger)^n\hat{A}\hat{\mathcal{U}}^n|\rho_{\mathrm{ss}}^{K}\rangle\rangle\ .\end{aligned} \tag{3.29}$$

Using $\hat{\mathcal{U}}|\mathbb{1}\rangle\rangle = |\mathbb{1}\rangle\rangle$, which was established in Sec. 2.3, we recover the final expression

$$\mathrm{Tr}\bigl(\hat{A}\hat{\rho}_{\mathrm{ss}}\bigr) = \frac{\bigl[\tilde{\mathbf{A}}^{\mathrm{eff}}\mathbf{XR}\bigr]_1}{\bigl[\mathbf{NXR}\bigr]_1}\ ,\quad \text{with}\quad \tilde{\mathbf{A}}^{\mathrm{eff}}_j = \frac{1}{N_S}\langle\langle \mathbb{1}|\Bigl(\sum_{n=0}^{N_S-1}\bigl(\hat{U}^\dagger\bigr)^n\hat{A}\hat{U}^n\Bigr)|\rho(t_j)\rangle\rangle\ . \tag{3.30}$$

Computationally, this is equivalent to Eq. (3.22), however the new operator inside $\tilde{\mathbf{A}}^{\mathrm{eff}}$ is often non-local. THerefore, it might be computationally advantageous to take the sum out of $\tilde{\mathbf{A}}^{\mathrm{eff}}_j$ and evaluate N_S observables individually instead. The crucial advantage we gain by avoiding projecting $|\rho_{\mathrm{ss}}^{K}\rangle\rangle$ onto the $q = 0$ subspace directly, is that in most use cases the operator $\hat{A}$ is much simpler than the states in the Krylov space in the sense that $(\hat{\mathcal{U}}^\dagger)^n\hat{A}\hat{\mathcal{U}}^n$ can be calculated exactly. For instance, expectations with particle-particle correlators as considered in Sec. 4.2.4 can be calculated easily when also taking into account the symmetries the system has. For more details, see App. A.2.

Note that Eq. (3.30) can be combined with the cancellation of non-Hermitian artifacts similarly as in Eq. (3.24), and we get a Hermitian expectation value as

$$\mathrm{Tr}\bigl(\hat{A}\hat{\rho}_{\mathrm{ss}}\bigr) = \frac{\bigl[\tilde{\mathbf{A}}^{\mathrm{eff}}\mathbf{XR}\bigr]_1 + \bigl[\tilde{\mathbf{A}}^{\mathrm{eff},*}\mathbf{XR}\bigr]_1^*}{2\bigl[\mathbf{NXR}\bigr]_1}\ ,\qquad \tilde{\mathbf{A}}^{\mathrm{eff},*}_j = \frac{1}{N_S}\langle\langle \mathbb{1}|\Bigl(\sum_{n=0}^{N_S-1}(\hat{U}^\dagger)^n\hat{A}^\dagger\hat{U}^n\Bigr)|\rho(t_j)\rangle\rangle\ . \tag{3.31}$$

The main bottleneck in generalizing the expressions Eq. (3.30) and (3.31) to continuous symmetries, is the explicit expression of the projector $\hat{\mathcal{P}}$ in terms of the unitary $\hat{\mathcal{U}}$. Indeed, in the case of a $U(1)$-symmetry, the generator has countably infinite eigenvalues, the unitary depends continuously on a parameter a (c.f. Sec. 2.3) and Eq. (3.28) takes on the form of a Fourier series

$$\hat{\mathcal{P}}_n = \frac{1}{2\pi}\int_0^1 \mathrm{d}a\; \mathrm{e}^{2\pi \mathrm{i} a n}\, \hat{\mathcal{U}}(a)\,. \tag{3.32}$$

Notice the similarity to Eq. (3.28), which motivates to perform the same steps as before. Indeed, doing so leads to a similar result

$$\mathrm{Tr}\big(\hat{A}\hat{\rho}_{\mathrm{ss}}\big) = \langle\!\langle \mathbb{1}|\hat{\mathfrak{A}}|\rho_{\mathrm{ss}}^{K}\rangle\!\rangle\;, \qquad \hat{\mathfrak{A}} = \frac{1}{2\pi}\int_0^1 \mathrm{d}a\; \hat{U}^{\dagger}(a)\hat{A}\hat{U}(a)\;. \tag{3.33}$$

Thus, Eq. (3.30) is also applicable in the continuous case, only the operator inside $\tilde{\mathbf{A}}^{\mathrm{eff}}$ is replaced by $\hat{\mathfrak{A}}$ and in spirit, only the sum is changed for an integral. This approach is readily generalized to other continuous symmetries in the same fashion.

Also the derivation of Eq. (3.30), (3.31) and (3.33) solely rely on the fact that $\hat{\mathcal{U}}|\mathbb{1}\rangle\!\rangle = |\mathbb{1}\rangle\!\rangle$ and in particular the explicit form of the generator of time evolution is irrelevant, which is particularly useful for the generalization of the framework to non-Markovian settings.

3.2.6 Generalizing to non-Markovian open quantum systems

Up to now we considered the Lindbladian as the generator of time-evolution in the CLIK-MPS framework. However, the framework is not restricted to the Markovian case. The crucial observation is that non-Markovian systems can be described in a similar fashion as Markovian ones via so-called Markovian embedding [41, 42]. One example is the mesoscopic leads approach [80, 81] where structured, non-Markovian environments are approximated by replacing each bath with a finite set of damped, discrete lead modes. The spectral density g characterizing the mesoscopic bath can be fitted by a sum of Lorentzian functions, which are implemented via the lead modes. In this way, the system plus lead modes again obey a Lindblad equation, and CLIK-MPS can be employed. Also, the efficient subspace arithmetic is not specifically tailored to Lindbladians and we can use the techniques described in Sec. 3.2.5 also in the non-Markovian setting. However, a big challenge for the numerical simulation of the time evolution itself arises. The enforced one-dimensional (1D) geometry of MPS leads to the natural emergence of long-range couplings in the respective generators of time evolutions when using Markovian embedding. Thus, time evolution using TDVP will suffer from exponentially increasing bond dimensions, which severely limits accessible times and system sizes. Luckily though, our framework has turned out to be quite robust to truncation, which will help overcome these challenges (c.f. Fig. 9a and Sec. 3.2.1). Nevertheless, exploring the regime of non-Markovian many-body open quantum systems remains a complicated task and will be subject to future research.

Moreover, a vast class of non-Markovian systems can readily be described by replacing the Lindblad generator $\hat{\mathcal{L}}$ with the hierarchical equations of motion (HEOM) generator $\hat{\mathcal{L}}_{\mathrm{HEOM}}$ [117, 5], and we will investigate the compatibility of the HEOM generator with CLIK-MPS in future research.

Note that the dissipative Bose-Hubbard Lindbladian Eq. (3.1) is already suitable as a preliminary non-Markovian test case. Although the environment is Markovian, the system-environment couplings feature interactions between different sites in real space. This leads to a local coupling in particle-momentum space, where each bosonic mode k is coupled to an environment, and it can exchange momentum q with the environment according to a non-trivial spectral density

$$\big|g_q(k)\big|^2 = 16\cos\Big(\frac{k-q}{2}\Big)^2 \sin\Big(\frac{k}{2}\Big)^2\,, \tag{3.34}$$

which is readily derived from Eq. (4.3). Such structured spectral densities are a feature of non-Markovian environments and typically arise when performing Markovian embeddings to describe non-Markovian environments [41, 42]. Consequently, we expect the numerical challenge in studying Eq. (3.1) to be comparable to Markovian embeddings of non-Markovian setups.

3.3 Simulations – Benchmarking the framework

After we carefully introduced the theory and implementation of the CLIK-MPS framework in Section 3.2, we are finally ready to evaluate its performance. We do this at the example of a Bose-Hubbard model with nearest-neighbor driving, given by Eq. (3.1). For small system sizes we can establish benchmark data in Sec. 3.3.1 by explicitly solving for the spectrum and eigenstates using ED, which we compare to CLIK-MPS. Moving on to larger system sizes is straightforward, but we face the problem of reliable error estimation and convergence analysis, and we therefore present multiple strategies filling this gap in Sec. 3.3.2. Note that results for large-scale calculations out of reach for ED are shown in Section 4.

Time evolution is carried out using TDVP [103, 54] combined with the local subspace expansion (LSE) [118, 116], as also discussed in Sec. 2.5. Additional information on the implementation is given in Appendix A.1.

3.3.1 Comparison with ED

To investigate the performance of CLIK-MPS, we benchmark the framework with spectra and eigenvectors obtained through ED methods for small scale systems. We once more consider the Bose-Hubbard Lindbladian Eq. (3.1), and fix the number of lattice sites to 5 and the number of bosons to 4. Complementary we show results obtained from another approximate method, where a Krylov space is built from real-time-evolved states initialized with a randomly chosen initial state [110]. We will also refer to this method as the $\alpha = 0$ method, as only a time evolution with zero complex angle is used.

These calculations are shown in Fig. 6. For CLIK-MPS, we chose the two angles $\alpha = 0$ and $\alpha = 0.05$ and to compare the methods realistically, we use the same maximal time $T = 4$ for all time evolutions and sampling interval $\delta t = 0.1$.

In Fig. 6a we show a set of Krylov low-lying eigenvalues in the complex plane. The steady state ($\lambda_1 = 0$) obtained using ED (circles) is accurately reproduced using either the $\alpha = 0$ method (blue triangles), or CLIK-MPS (orange triangles). However, already for the first excited state, a small deviation is visible in the $\alpha = 0$ data, which only becomes more severe when trying to evaluate higher excited states. On the other hand, CLIK-MPS effortlessly resolves multiple low-lying eigenvalues with high accuracy. It reproduces the first 5 eigenvalues without any problems. Note that the chosen positive angle $\alpha = 0.05$ enhances the precision of the eigenvalues with positive imaginary part, and we can obtain eigenvalues with negative imaginary part by complex conjugation, as already outlined in Sec. 3.2.2.

Next, we compute the deviation of the Krylov Lindbladian right (left) eigenvectors $|r_j^{\mathrm{K}}\rangle\!\rangle$ ($|l_j^{\mathrm{K}}\rangle\!\rangle$) from the exact eigenvectors $|r_j\rangle\!\rangle$ ($|l_j\rangle\!\rangle$) obtained from ED in Fig. 6b and Fig. 6c, respectively. These are obtained by extracting the vector representations of the time-evolved states $|\rho(t_j)\rangle\!\rangle$ in the basis used for the exact diagonalization $|e_m\rangle\!\rangle$. It is given by $\mathbf{E}_{mj} = \langle\!\langle e_m|\rho(t_j)\rangle\!\rangle$ and the overlaps are given by

$$\langle\!\langle r_j|r_j^K\rangle\!\rangle = \left[\mathbf{R}^{\mathrm{E}\dagger}\mathbf{E}\mathbf{X}\mathbf{R}\right]_{jj} , \tag{3.35}$$

where $\mathbf{R}^{\mathrm{E}}$ is the matrix containing the right eigenvectors calculated using ED. Here, the impact of the additional complex-time evolution and optimal initialization becomes very evident when comparing with the $\alpha = 0$ curves. For all five lowest lying eigenvectors, the accuracy is improved by more than three orders of magnitude. Additionally, we also include a comparison against a commonly used approach to approximate the steady state. Since the time evolution of a physical state converges to the steady state, we can just perform a time evolution and take the longest evolved state as the approximate steady state (crosses). This ansatz exhibits the poorest convergence when evolving up to the same maximal evolution time as the one used for the

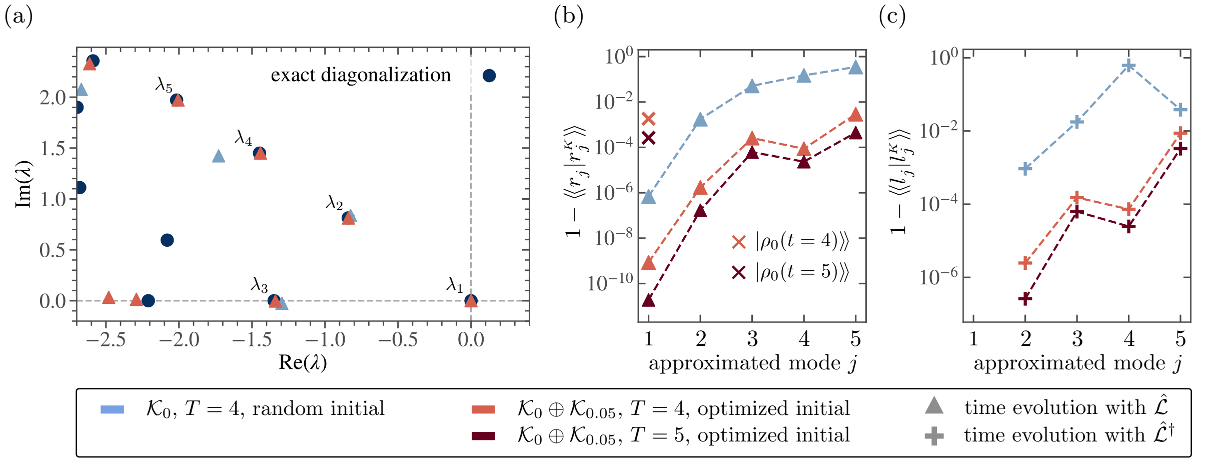

Figure 6: Accuracy of CLIK-MPS compared against ED and real-time evolution methods [110] for the Bose-Hubbard model Eq. (3.1). Panel a): Comparison of the low-lying Lindbladian eigenvalues against ED reference data (●). We consider time evolution with $\hat{\mathcal{L}}$ (▲) for a real-time evolution method [110] (blue) compared to CLIK-MPS (orange), which uses a real and a $\alpha = 0.05$ time evolution. Panel b): Deviation of approximated Lindbladian right eigenmodes from ED reference data and of time-evolved states at the maximal evolution time T (×) to the steady state. Panel c): Same analysis as in panel b), just for the left eigenmodes (+) obtained through time evolution with $\hat{\mathcal{L}}^\dagger$. We considered $L = 5$ lattice sites, $N = 4$ bosons, set $J = U = \kappa = 1$. Krylov spaces were built with $\delta t = 0.1$, while the maximal evolution time T and employed angles α are specified in the plot. The figure is adapted from [2].

Krylov-space-based methods, with a loss in precision of more than six orders of magnitude when comparing to CLIK-MPS. Moreover, increasing the duration of the time evolution systematically enhances the precision not only of the steady state $|r_1^{\mathrm{K}}\rangle\rangle$, but of all right eigenvectors.

We do a similar comparison for the left eigenmodes in Fig. 6c. As we already established in Sec. 3.2.3, targeting left eigenmodes requires evolving with the adjoint Lindbladian $\hat{\mathcal{L}}^\dagger$. Since the left eigenmodes of the Lindbladian are the right eigenmodes of $\hat{\mathcal{L}}^\dagger$ according to Eq. (3.16), we can again employ Eq. (3.35) to calculate the overlap. We build the Krylov space according to Sec. 3.2.3. Since the left eigenmode $\hat{l}_1$ is exact in the subspace, we only show the deviation of the higher left eigenmodes from exact data. Similarly as for the right eigenvectors, the accuracy is improved by 2 to 4 orders of magnitude for the three slowest decaying modes compared to the $\alpha = 0$ calculations. This showcases that the improvements made within CLIK-MPS lead to unprecedented accuracy, and we are confident to employ the framework in physically challenging large-scale systems. In large scale calculations, we will typically employ time evolutions with $\hat{\mathcal{L}}$ to approximate the spectrum, since it targets excited eigenmodes more efficiently due to the warm-up procedure. However, before we do exactly that in Sec. 4, we first need some measures of convergence and accuracy of the obtained spectra and eigenvectors.

3.3.2 Error approximation beyond ED

In the last section we tested the accuracy of CLIK-MPS by comparing to ED reference data. However, when considering large-scale systems, ED becomes unavailable and assessing the precision and convergence of CLIK-MPS needs to be done differently.

Tackling this task requires developing several different schemes that are optimized for specific parts of the spectrum. This includes error and convergence analysis for the steady state, where we develop both analytical and numerical techniques, and the remaining low-lying spectrum, where analytical methods fail and we fully rely on numerics.

First, we want to quantify the deviations of CLIK-MPS from the exact steady state $|\rho_{\mathrm{ss}}\rangle\!\rangle$ through accessible quantities such as expectation values or variances. Rigorously speaking, we want to bound $\left|\langle\!\langle \rho_{\mathrm{ss}}^K|\rho_{\mathrm{ss}}\rangle\!\rangle\right|^2$ from below by a quantity which we can calculate within the Krylov space, with $|\rho_{\mathrm{ss}}^K\rangle\!\rangle$ being the CLIK-MPS approximate steady state. Indeed, we can establish the bound

$$\left|\langle\!\langle r_1^K|r_1\rangle\!\rangle\right|^2 \geq 1 - \frac{\langle\!\langle r_1^K|\hat{\mathcal{L}}^\dagger\hat{\mathcal{L}}|r_1^K\rangle\!\rangle}{|\sigma_2|^2} \,, \tag{3.36}$$

where σ_2 is the second lowest singular value of $\hat{\mathcal{L}}$. Note that the right eigenvector $\hat{r}_1$ is the unnormalized steady state, and $\left|\langle\!\langle \rho_{\mathrm{ss}}^K|\rho_{\mathrm{ss}}\rangle\!\rangle\right|^2$ is directly connected to $\left|\langle\!\langle r_1^K|r_1\rangle\!\rangle\right|^2$. For the proof, first note that $\hat{\mathcal{L}}^\dagger\hat{\mathcal{L}}$ is Hermitian and positive. Furthermore, the steady state is its only eigenstate with eigenvalue 0. The gap of this Hermitian operator is given by $\mu_2 = \sigma_2^2$, where σ_2 is the second lowest singular value of $\hat{\mathcal{L}}$. We may diagonalize $\hat{\mathcal{L}}^\dagger\hat{\mathcal{L}}$, denote its increasingly ordered eigenvalues by μ_k and its eigenvectors by $|v_k\rangle\!\rangle$. The state $|r_1^K\rangle\!\rangle$ is expressed in the eigenbasis of $\hat{\mathcal{L}}^\dagger\hat{\mathcal{L}}$ as $|r_1^K\rangle\!\rangle = \sum_m a_m|v_m\rangle\!\rangle$ which yields

$$\langle\!\langle r_1^K|\hat{\mathcal{L}}^\dagger\hat{\mathcal{L}}|r_1^K\rangle\!\rangle = \sum_{m\geq 2} \mu_m|a_m|^2 \,. \tag{3.37}$$

Combining Eq. (3.37) with the normalization constraint $= \sum_m |a_m|^2$ leads to the bound

$$|a_1|^2 = 1 - \sum_{m\geq 2}|a_m|^2 \geq 1 - \frac{1}{\mu_2}\sum_{m\geq 2}\mu_m|a_m|^2 \,, \tag{3.38}$$

where we used that $\mu_m/\mu_2 \geq 1$ if $m \geq 2$. Since $|a_1|^2 = \left|\langle\!\langle r_1^K|r_1\rangle\!\rangle\right|^2$ the lower bound follows immediately. Although we do not know the singular value σ_2, Eq. (3.36) establishes a connection between the approximation quality and the variance, which makes it possible to compare the accuracy of different approximate steady states which each other. A non-trivial upper bound can be obtained using $\mu_m/\mu_{D^2} \leq 1$, where μ_{D^2} denotes the highest eigenvalue. Following the same steps as above, this implies

$$\left|\langle\!\langle r_1^K|r_1\rangle\!\rangle\right|^2 \leq 1 - \frac{\langle\!\langle r_1^K|\hat{\mathcal{L}}^\dagger\hat{\mathcal{L}}|r_1^K\rangle\!\rangle}{|\sigma_{D^2}|^2} \,. \tag{3.39}$$

Eq. (3.36) and (3.39) also reveal, that the sharpness of the bounds is governed by the ratio σ_{D^2}/σ_2, which is connected to the condition number of the Lindbladian, restricted to the subspace orthogonal to the steady state.

It is possible to calculate $\langle\!\langle r_1^K|\hat{\mathcal{L}}^\dagger\hat{\mathcal{L}}|r_1^K\rangle\!\rangle$ directly inside the Krylov subspace using the methods described in Sec. 3.2.5. Nevertheless, the efficient calculation requires building the variance matrix $\langle\!\langle \rho(t_i)|\hat{\mathcal{L}}^\dagger\hat{\mathcal{L}}|\rho(t_j)\rangle\!\rangle$, which is a computationally costly expression since the operator features long-range interactions. Although more efficient implementations of variances exist [54], for most large-scale calculations, it is not favorable to compute the variance, and instead we need a more practical numerical method to investigate the approximation quality and convergence.

A simple yet effective approach is to compare different Krylov spaces with each other. The idea relies on diagonalizing the Lindbladian in each Krylov space and then comparing the states and spectra. To assess the quality of the steady state, we propose to calculate expectation values and compare them. We generate multiple Krylov spaces by varying the maximal evolution time

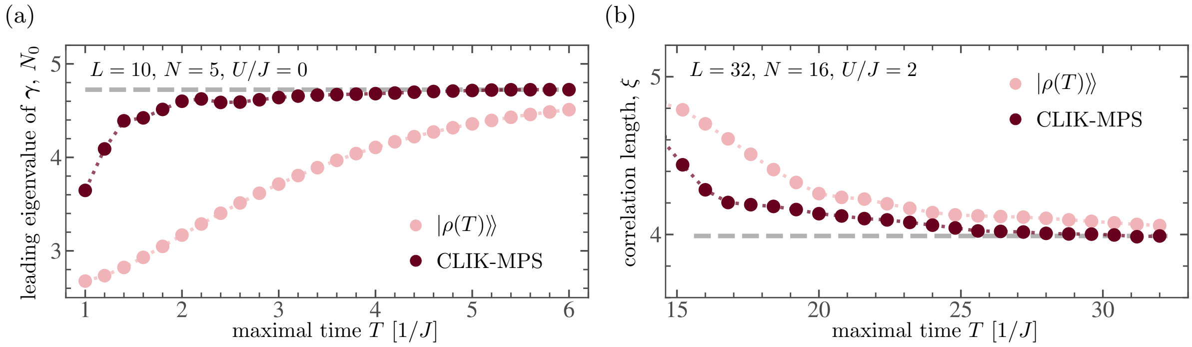

Figure 7: Large scale convergence analysis for the steady state. We show a comparison between a single time evolved state (pink) and CLIK-MPS (red) for a Bose-Hubbard model Eq. (3.1). Panel a): Leading eigenvalue N_0 of the OBDM γ depending on the maximal evolution time T. By tracking the dependence we can see if the approximation is sufficiently converged, indicated by the grey line. The Krylov space was built with $\alpha = 0.05$ and $\delta t = 0.05$ for 10 sites, 5 particles, $U/J = 0$, and $\kappa/J = 2$. Adapted from [2]. Panel b): Correlation length ξ depending on the maximal evolution time T. The Krylov space was built with $\alpha = 0.02$ and $\delta t = 0.4$ for 32 sites, 16 particles, $U/J = \kappa/J = 2$.

T, while the sampling interval δt remains fixed, leading to subspaces with different dimensionality. In the following, we label the CLIK-MPS Krylov spaces $\mathcal{K}_{0,\alpha}(T)$ by the maximal evolution time T. In this way we ensure that $\mathcal{K}_{0,\alpha}(T) \subseteq \mathcal{K}_{0,\alpha}(T')$ whenever $T \leq T'$, and we expect the approximation to be better the larger the Krylov space is. We say that the steady state $|\rho^K_{\mathrm{ss}}(T)\rangle\rangle$ is *sufficiently converged* with respect to an operator $\hat{O}$, if

$$\lim_{T'\to\infty} \frac{\left|\mathrm{Tr}\big(\hat{O}\hat{\rho}^K_{\mathrm{ss}}(T)\big) - \mathrm{Tr}\big(\hat{O}\hat{\rho}^K_{\mathrm{ss}}(T')\big)\right|}{\left|\mathrm{Tr}\big(\hat{O}\hat{\rho}^K_{\mathrm{ss}}(T')\big)\right|} \ll \epsilon \,, \tag{3.40}$$

where we introduced the precision ϵ. Eq. (3.40) implies that after time T the expectation value of $\hat{O}$ does not change much, and time T is sufficient to capture the right behavior of $\hat{O}$ (up to a precision ϵ). Although the choice of $\hat{O}$ is in principle free, there are some natural operators to consider. For instance the expectation of the two point correlator C (for bosonic systems given by $\hat{O} = \hat{b}^\dagger_i \hat{b}_j$), which is connected to the correlation structure of the steady state. In the context of bosonic systems, it is often referred to as the one-body reduced density matrix (OBDM) γ, defined by

$$\gamma_{ji} \equiv C(i-j) \equiv \mathrm{Tr}\big(\hat{b}^\dagger_i \hat{b}_j \hat{\rho}_{\mathrm{ss}}\big) \,. \tag{3.41}$$

Its off diagonal elements contain information about the correlation structure of the steady state, and we find the asymptotic behavior

$$C(i-j) = \frac{c_1}{|i-j|^{c_2}} \mathrm{e}^{-|i-j|/\xi} + c_3 \,. \tag{3.42}$$

Here, $c_3 > 0$ means long-range order, $c_2 > 0$ quasi-long-range order and $\xi < \infty$ implies short-range order.

In Fig. 7 we check the convergence of two quantities derived from the one-body reduced density matrix (OBDM) for the Bose-Hubbard Lindbladian Eq. (3.1). In Fig. 7a we track the leading eigenvalue N_0 of γ, while in Fig. 7b we look at the correlation length ξ (c.f. Eq. (3.42)) in the steady state. For both quantities, we can observe the convergence with increasing time T.

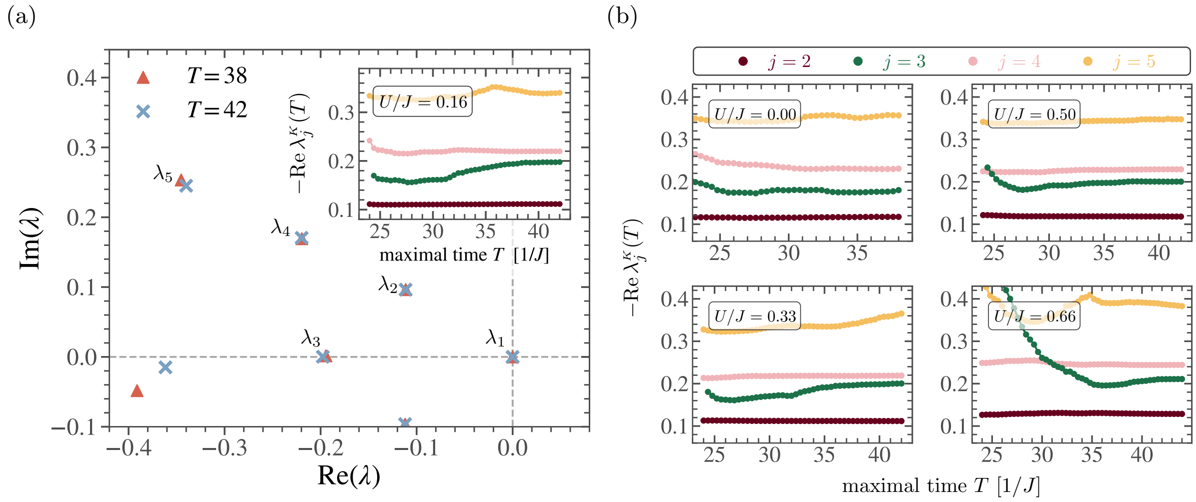

Figure 8: Convergence analysis for large-scale calculations of the low-lying eigenvalues of the dissipative Bose-Hubbard model Eq. (3.1) with 20 sites and 10 bosons at $\kappa/J = 2$. Panel a): Low-lying spectrum at onsite interaction $U/J = 0.16$ and we compare two maximal evolution times T. Adapted from [2]. Inset and Panel b): 5 lowest eigenvalues obtained by CLIK-MPS depending on T for several U/J. The maximal evolution time T must be chosen such that the eigenvalue of interest is converged, i.e. does not depend on T any more. The Krylov space is built with a sampling interval $\delta t = 0.2$ and using $\alpha = 0.02$. This constitutes the convergence analysis for the data presented in Fig. 22b.

We also compare to the simple approximation method, where a single time-evolved state $|\rho(T)\rangle\rangle$ is chosen for the steady state. For both quantities, CLIK-MPS displays faster convergence, and we conclude that after $T = 5$ for Fig. 7a with $L = 10$ and $T = 30$ for Fig. 7b with $L = 32$ the corresponding quantities are sufficiently converged, and the results are reliable.

A similar method can be employed for the numerical error approximation of higher excited eigenvalues. Here, instead of comparing expectation values, we directly compare the approximated spectra $\lambda_j^K(T)$, and a spectral feature at time T is sufficiently converged if

$$\lim_{T' \to \infty} \frac{\left|\lambda_j^K(T) - \lambda_j^K(T')\right|}{\left|\lambda_j^K(T')\right|} \ll \epsilon \,, \tag{3.43}$$

in close analogy to Eq. (3.40). In Fig. 8, we show this analysis for the Bose-Hubbard model Eq. (3.1) with 20 sites and 10 bosons for multiple onsite interactions U/J. While the lowest eigenvalue λ_2 is already converged at around $T = 25$, the next eigenvalue λ_3 needs a time evolution to about $T = 40$ to converge fully. The convergence time for higher eigenvalues varies strongly, as we see when comparing λ_4 and λ_5. There are also large differences between the convergence at different U/J. We conclude that numerical convergence analysis works efficiently and reliably. Also from a computational perspective, Eq. (3.40) and (3.43) are good criteria: If the Gram matrix $\mathbf{M}$ and effective Lindbladian $\mathbf{L}^{\text{eff}}$ have been calculated for a large time $T_{\max}$, then all Krylov spaces $\mathcal{K}_{0,\alpha}(T)$ with $T < T_{\max}$ require no further overlaps or expectation values. This makes convergence analysis particularly easy.

In Fig. 9b we lastly show another convergence analysis, now restricted to the dissipative gap. We compare various system sizes (linestyle) and onsite interactions U/J (color) at half filling,

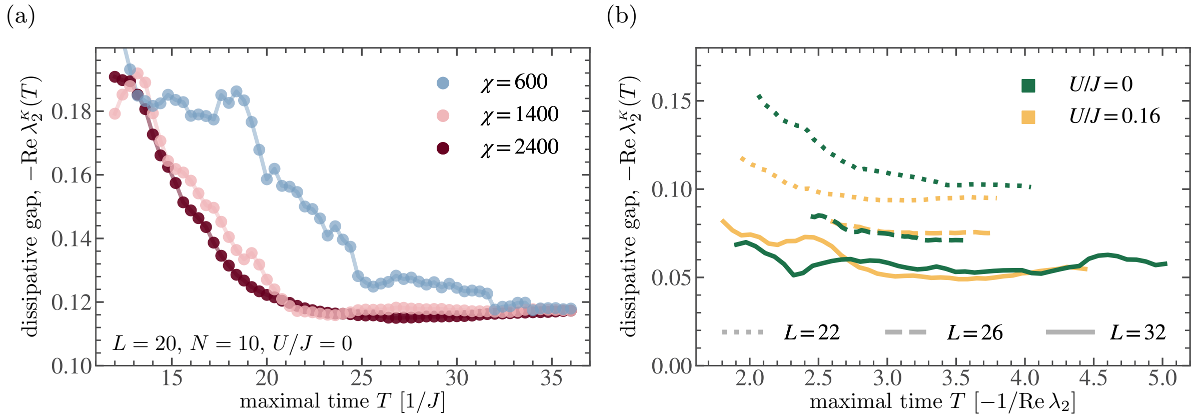

Figure 9: Convergence analysis of the dissipative gap for the dissipative Bose-Hubbard model Eq. (3.1) at $\kappa/J = 2$, adapted from [2]. Panel a): Dissipative gap for 20 sites and 10 particles at $U/J = 0$ for different maximal times T. We chose sampling rate $\delta t = 0.2$ and consider data from time evolutions with different maximal bond dimensions χ. Notice, while the approximated gap depends heavily on the bond dimension at intermediate times, all eventually converge to the same value. Panel b): Dissipative gap from CLIK-MPS for system sizes $L = 22$, 26 at $\delta t = 0.4$ and $L = 32$ at $\delta t = 0.6$ depending on T for two different U/J. T is given in units of the gap to compare the different system sizes. We set the maximal bond dimension to $\chi = 1400$.

depending on the maximal time T for the Krylov space. Since convergence times strongly depend on the system parameters, we express T in orders of the inverse dissipative gap $-1/\mathrm{Re}\,\lambda_2$. All data is sufficiently converged between $T = 3.5$ and 4.5 in orders of the inverse dissipative gap. Nevertheless for $L = 32$, we evolve further to be sure. Note that this is a part of the error convergence analysis for the data shown in Figure 15.

Finally, we can check the effect of truncation during time evolution on the approximation. If the effective bond dimension χ_{eff} given in Eq. (3.7) actually has the effect we expected in Sec. 3.2.1, the spectrum should depend on the maximal bond dimension at intermediate times and converge to the same value at late times. We check this intuition in Fig. 9a for the Bose-Hubbard model Eq. (3.1) with 20 sites and 10 bosons at $U = 0$ and $\kappa/J = 2$. We compare the dissipative gap obtained by CLIK-MPS for three different time evolutions, where only the maximal bond dimensions are altered. Note that the respective maximal bond dimensions are reached during the time evolution, which suggests, that truncation errors happen. As expected, the three calculations yield different behavior at intermediate times, while they all converge to the same value eventually. Note that the smaller the bond dimension, the longer it takes for the dissipative gap to converge, which is also in agreement with $\chi_{\text{eff}} \sim N^K$. Indeed, at intermediate times, the effective bond dimension of the $\chi = 2400$ evolution is high enough to render the slowest decaying mode accurately, which is not the case for the $\chi = 600$ evolution. Eventually though, also the latter will reach a sufficiently high effective bond dimension and the dissipative gap is accurately captured. Note that the entanglement is higher for the transient dynamics than for the steady state, which might also play a role here.

The analysis reveals a picture in which we can trade lower bond dimension during time evolution for a larger number of linearly independent time-evolved vectors (which implies longer time evolution). This tradeoff is a remarkable property of the method and explains, why the framework is so robust against truncation errors, a property which is indispensible when simulating large systems.

4 Dissipative Bose-Hubbard model – properties and the Mpemba effect

In this chapter, we test the capabilities of CLIK-MPS for large scale interacting many-body open quantum systems by analyzing and optimizing a DSP protocol to prepare BECs on optical lattice platforms. So-called DSP protocols use controlled interactions with an environment to drive the ultracold atoms in the optical lattice into a target state. Consequently, they represent a possible route to prepare highly-entangled states in analog quantum simulators based on ultracold atoms in optical lattices [57, 58, 59, 60, 61, 62, 63]. Although a lot of progress in realizing such protocols has been done, long preparation times [67, 68] due to the closing of the dissipative gap upon increasing the system size prohibit the efficient use in large scale systems. A central goal of this chapter is therefore to use the quantum Mpemba effect to speed up the dissipative preparation of BECs.

The chapter is organized as follows: After introducing the model in Sec. 4.1 followed by a brief discussion of the experimental realization in Sec. 4.1.1, we take a look at the properties of the prepared target state in Sec. 4.2. In Sec. 4.3 we use CLIK-MPS to analyze the behavior of the dissipative gap around a critical point, finding strong evidence for the emergence of non-linear hydrodynamics and the Kardar-Parisi-Zhang (KPZ) universality class. In Sec. 4.4 we analyze the dependence on the physical parameters further and introduce unitary transformations connecting different Lindbladians. Lastly, in Sec. 4.5 we analyze the spectrum of the Lindbladian with the goal of utilizing the quantum Mpemba effect to speed up the protocol exponentially. This proves to be especially difficult, since the Lindbladian is not analytically diagonalizable, making it inaccessible to previously proposed strategies of finding admissible states [6, 105]. We address this problem by arguments relying on the symmetries of the system, making it possible to characterize the slow decaying channels analytically, as schematically depicted in Figure 10b. We numerically verify the analytical predictions, analyze the parameter regions where a quantum Mpemba effect is stabilized, and discuss the experimental realization of the proposed quickly-decaying states. Throughout the chapter, we provide numerical data obtained by MPS calculations, and we especially use and showcase the capabilities of the CLIK-MPS framework introduced in Sec. 3.

Note that the dissipative protocol was first introduced by Diehl et al. in 2008 [17]. This section is strongly based on the publication [1], and we show results for large-scale systems that were presented in [2], both summarizing some of the work done in the scope of this thesis.

4.1 Introducing the model

Since dissipative state preparation (DSP) protocols crucially rely on interactions with a tailored environment to drive a system into a desired target state, the theoretical treatment of quantum systems coupled to environments is needed. This can be done by describing the interactions in the optical lattice by a Hamiltonian and the interaction with the environment through jump operators within the Born-Markov approximation. If these conditions are met, the dynamics is governed by a Lindbladian, as discussed in Sec. 2.1. Since the fixed point of the dynamics is given by the steady state of the Lindbladian, a good DSP protocol can be characterized by the proximity of the steady state and the experimental target state. From this purely theoretical perspective, the protocol takes the form of a model, which might be far away from experimental reality.

Of course it is also imperative to look through the eyes of an experimentalist, who is interested in a *realizable* protocol, that is, a model that is implementable on an optical lattice or analog quantum computer. For example, a good candidate model for a protocol should ideally feature

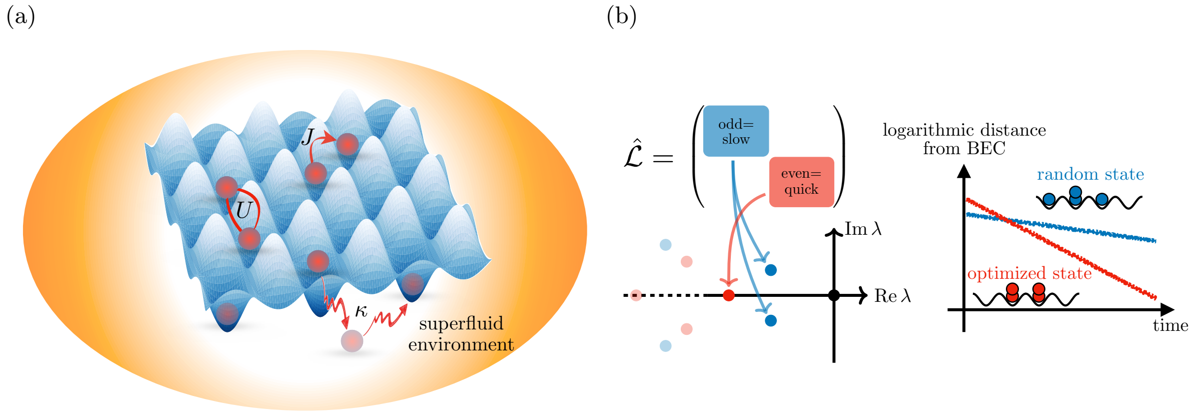

Figure 10: Panel a): Dissipatively preparing a Bose-Einstein condensate (BEC) in an optical lattice by combining coherent hopping with dissipation-mediated tunneling via a superfluid environment in which the optical lattice is immersed. Panel b) left: The Lindbladian $\hat{\mathcal{L}}$ describing the system features a weak $\mathbb{Z}_2$-symmetry corresponding to reflections about the center of the lattice. The Lindbladian consequently possesses a block-diagonal structure, corresponding to evenly and oddly transforming states under reflections. Spectral analysis shows that the slowest-decaying mode belongs to the oddly transforming block. Panel b) right: Based on this symmetry argument, we identify a class of (evenly-transforming) product states that converge exponentially faster to the steady state. The figures were adapted from [1].

local terms and a simple dissipator. Keeping these requirements in mind, Diehl et al. introduced a theoretical model which describes a DSP protocol to prepare BECs in 2008 [17], which we schematically depicted in Fig. 10a. Note that we comment on the experimental realization in Sec. 4.1.1.

The model consists of bosons in a 1D lattice described by the Bose-Hubbard Hamiltonian

$$\hat{H}_{k_0} = -J\sigma_{k_0} \sum_{j=1}^{L-1} \left(\mathrm{e}^{\mathrm{i}k_0} \hat{b}_{j+1}^{\dagger} \hat{b}_j + \text{h.c.} \right) + \frac{U}{2} \sum_{j=1}^{L} \left[\hat{b}_j^{\dagger}\right]^2 \left[\hat{b}_j\right]^2 . \tag{4.1}$$

Here, $\hat{b}_j^{\dagger}$ ($\hat{b}_j$) creates (annihilates) a boson on site j, L is the number of sites, J and U represent the hopping amplitude and the onsite interaction strength, and $k_0 = 2\pi n/L$ with $n \in \mathbb{N}$ is the target momentum. We consider open boundary conditions (OBCs) due to experimental and numerical benefits. The prefactor σ_{k_0} is 1 for $|k_0| < \pi/2$ and -1 otherwise, ensuring that the real part of the hopping amplitude is always negative for $J > 0$.

This Hamiltonian alone already admits intricate physics. The first sum, called the *coherent hopping* term, is non-interacting and tends to delocalize the system by enforcing bosons to condense in the single particle state with the lowest energy. The corresponding Hamiltonian eigenstate is exactly known and sharply peaked around the momentum k_0. This leads to the formation of a BEC with momentum k_0 in the thermodynamic limit. Unfortunately, the second sum, called the *onsite interaction* term, tends to localize the particles, leading to a dynamic that is incompatible with the coherent hopping term. As a consequence, it is not immediately clear which term wins this competition, which will certainly depend on the system parameters J and U.

Indeed there is a transition between a delocalized superfluid phase and localized insulating phase, the former being only stable at the trivial point $U = 0$. Nevertheless, this behavior strongly depends on the dimensionality of the problem: In one and two dimensions, the Mermin-Wagner theorem forbids a phase transition away from $U = 0$ [119], while in higher dimensions the superfluid phase extends to finite U [120, 121].

To propose a model for a dissipative state preparation protocol, a dissipative interaction with an environment is needed. In the following, we study the Markovian dissipative dynamics obeying Eq. (2.2) and choose

$$\hat{L}_j^{k_0} = \sqrt{\kappa}\big(\hat{b}_{j+1}^\dagger + \mathrm{e}^{-\mathrm{i}k_0}\hat{b}_j^\dagger\big)\big(\hat{b}_{j+1} - \mathrm{e}^{\mathrm{i}k_0}\hat{b}_j\big)\,, \tag{4.2}$$

as jump operators. Here, κ is the dissipation strength and k_0 is fixed by the Hamiltonian parameters. Note that up to the phase factor $\mathrm{e}^{\mathrm{i}k_0}$ and boundary conditions, Eq. (4.1) and (4.2) are consistent with the model proposed in [69, 17]. A model with a similar phase factor was considered in [70].

In the Hamiltonian and all jump operators, each creation operator $\hat{b}^\dagger$ is paired with an annihilation operator $\hat{b}$, which shows that both commute with the total particle number $\hat{N} = \sum_j \hat{b}_j^\dagger \hat{b}_j$. According to Eq. (2.14), this implies that the total particle number is conserved by inducing a strong, continuous $U(1)$-symmetry. As also proven in Sec. 2.3, there is at least one steady state for each number of particles N (which are the eigenvalues of $\hat{N}$). In this specific model it is furthermore possible to prove that there is exactly one, which is a consequence of the specific form of the jump operators [17, 122].

The dissipation is only useful if it induces a dynamic that delocalizes the particles, stabilizing the superfluid phase. Indeed, the jump operators have the property of driving the system further into the superfluid phase. To see this, it is most convenient to transform the jump operators into momentum space. We discard boundary effects, and find

$$\hat{L}_q = \sqrt{\frac{\kappa}{L}} \sum_{k\in 1\mathrm{BZ}} \big(\mathrm{e}^{-\mathrm{i}(k-q)} + \mathrm{e}^{-\mathrm{i}k_0}\big)\big(\mathrm{e}^{\mathrm{i}k} - \mathrm{e}^{\mathrm{i}k_0}\big)\hat{b}_{k-q}^\dagger \hat{b}_k\,, \tag{4.3}$$

where the momentum $q = 2\pi n/L$ lies in the First Brillouin zone (1BZ), $q \in (-\pi, \pi]$ and we defined $\hat{b}_k^\dagger = \sum_j \mathrm{e}^{\mathrm{i}kj}\hat{b}_j^\dagger$. Now, the jump operator has an intuitive interpretation as a scattering process. If a boson with momentum k comes in, it is scattered into momentum $k-q$ with a transition rate proportional to the prefactor in Eq. (4.3). Note that this especially means the jump operator $\hat{L}_{k-k_0}$ scatters the incoming particle into the k_0-mode. Interestingly, for an incoming particle with momentum k_0, the transition rate is zero regardless of the value of q, and it is not scattered by any jump operator and remains at momentum k_0. Hence, particles already having momentum k_0 stay unchanged by the jump operators, while all other particles are scattered, partly also into the k_0-mode. As a consequence, its population increases and eventually a BEC with characteristic momentum k_0 forms. The jump operators can thus be interpreted as effectively pumping the particles into the k_0-mode.

This interpretation can be put on more rigorous footing by calculating the time dependent population of the k_0-mode, N_{k_0}, in a semiclassical pumping protocol. In the following we will refer to the particles outside the k_0-mode as the non-condensed particles. The setting is a system with N particles, and we assume that the probability during a timestep $\mathrm{d}t$ for a non-condensed particle to scatter into a condensed particle is constant, at α_0. This assumption is reasonable, since the jump operators do not contain a time dependence. The time derivative of N_{k_0} can now be written as

$$\frac{\mathrm{d}N_{k_0}}{\mathrm{d}t}(t) = \alpha_0\left(N - N_{k_0}(t)\right)\,. \tag{4.4}$$

This differential equation is solved by

$$N_{k_0}(t) = N - \big(N - N_{k_0}(0)\big)\,\mathrm{e}^{-\alpha_0 t}\,, \tag{4.5}$$

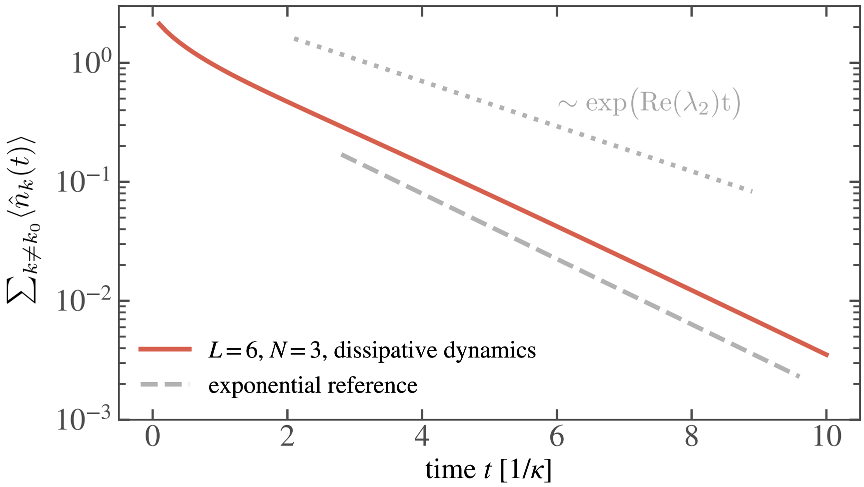

Figure 11: Testing the action of the jump operators. We show the population of the momenta $k \neq k_0$ not targeted by the Lindbladian, which in this case only consists of a dissipative part with jump operators $\hat{L}_j^{k_0}$ (see Eq. (4.2)). We find that this population decreases exponentially with time, indicating that the action of the jump operators can be indeed interpreted as pumping into the k_0 mode. To only see the influence of the jump operators, we set $J = U = 0$ and $\kappa = 1$. The system has $L = 6$ sites, $N = 3$ bosons, we chose $k_0 = 0$, and we use ED to simulate the dynamics.

where $N_{k_0}(0)$ denotes the number of bosons which are already in the k_0-mode in the initial configuration. The exponent is dictated by the rate α_0, which depends on the specific architecture of the system, and is in general difficult to calculate from macroscopic quantities.

We can check if the jump operator's action aligns with an interpretation as a pumping process, by tracking the number of particles left in the other modes, $N - N_{k_0}(t) = \sum_{k\neq k_0}\langle\hat{n}_k(t)\rangle$ during time evolution. In Fig. 11 we use exact diagonalization to describe the time evolution of a random initial state $|\rho_0\rangle\rangle$ for a system of 6 sites and 3 particles and calculate $N - N_{k_0}(t)$. To highlight the action of the jump operators, we switch off the Hamiltonian by setting $J = U = 0$. The dynamics is then governed by the dissipator $\mathcal{D}$ alone (c.f. Eq. (2.8)). As expected, the population of non-targeted modes drops during time evolution, and at time $t = 10/\kappa$, all but 3×10^{-3} particles have momentum k_0. Most importantly, the population decreases exponentially which supports the interpretation as an effective pumping protocol. Having in mind Lindbladian spectral theory this is not a big surprise, since the contributions outside of the steady state decay exponentially with time according to Eq. (3.2), and the slowest decaying mode λ_2 dictates the long-time behavior. We thus expect the behavior to be $N - N_{k_0}(t) \sim \exp\big(\mathrm{Re}(\lambda_2)t\big)$. To our surprise we find that the exponential decay is not governed by $\mathrm{Re}\,\lambda_2 = -0.436$, but instead by -0.633, which is also indicated in Fig. 11 via the dotted grey line. Doing the same calculations for several initial configurations, we furthermore see that this exponent is independent of the initial configuration, which is even more confusing. The question about this exponent is highly nontrivial, but at the end of this chapter we will be able to reason this odd behavior (see Sec. 4.5.5).

4.1.1 Experimental setup and realization

The main obstacle in realizing the model introduced in Sec. 4.1 are the jump operators Eq. (4.2) [123]. The Bose-Hubbard Hamiltonian itself presents no major difficulty, as it was successfully realized with ultracold atoms in optical lattices in the past [124, 121]. The problematic part of the implementation therefore concerns the realization of the jump operators. In short, the idea is to submerse the optical lattice into a superfluid of a different atomic species, which acts as an environment [17]. The goal is to engineer the interaction between the particles in the optical lattice and the surrounding superfluid in such a way that they are effectively captured by the jump operators. Diehl et al. proposed such a mechanism [17], by using a two band structure and exciting the out-of-phase part of particles on neighboring lattice sites using a driving laser. Then, the excited state can decay back into the lower band by emitting Bogoliubov quasiparticles into the superfluid. This process enriches the in-phase part of the state, since the excited state will relax into both an in-phase and out-phase part. Looking back at the jump operators, this process seems reasonable: If we read Eq. (4.2) from right to left, we first annihilate the out-of-phase part by $\hat{b}_{j+1} - \hat{b}_j$, and then create an in-phase part instead by $\hat{b}^\dagger_{j+1} + \hat{b}^\dagger_j$, which is exactly what happens effectively in the physical process. It is furthermore possible to show that this experimental setup is well described by the jump operators Eq. (4.2) [17, 122].

Unfortunately the realization is very challenging, and the protocol has not been implemented yet. But also other preparation schemes for BECs have their downsides: The starting point is to prepare an initial BEC in a harmonic trap via several cooling stages. Then, it is subsequently transferred into a shallow optical lattice [125]. In the process, the BEC may be contaminated with unwanted excitations and quasiparticles, and the transfer process needs to be performed quasi-adiabatically. The transfer process thus constitutes the main bottleneck, as it exposes the BEC to particle loss, decoherence, and heating originating from the ubiquitous presence of environmental channels [126]. The dissipative preparation therefore presents a viable alternative, skipping the tedious loading procedure completely.

The dissipative process may have additional advantages, in the form of better controlability of the condensate quality. To analyse this, we need to characterize the properties of the prepared state, which is the steady state of the Lindbladian Eq. (3.1). This is rendered difficult due to the quartic terms both in the Hamiltonian and dissipator, which is why we use a mean-field theory approach in the next section.

4.2 Mean-field analysis for the steady state

In Section 4.1 we established that the dissipative Bose-Hubbard model features parts giving rise to incompatible dynamics. While the coherent hopping term in the Hamiltonian (controlled by J) and the dissipative hopping in the jump operators (controlled by κ) want to enforce a BEC with momentum k_0, the onsite interaction term in the Hamiltonian (controlled by U) tends to localize the state. In light of this heuristic initial consideration, it is interesting to see which of the terms dominates in the steady state. Since the full Lindbladian is not integrable, we need to rely on approximations which are only valid in confined parameter regimes. These will be backed by simulations with the full Lindbladian. Note that the following mean-field approximation is similar to [17, 122].

For convenience, let us first consider the case of characteristic momentum $k_0 = 0$ and generalize the result later. Let us define the particle densities $n = {}^{N}\!/_{L}$ and $n_0 = {}^{N_0}\!/_{L}$, where N_0 is the population of the zero-momentum mode. In the following, we assume that the condensate depletion δ defined as

$$\delta = \frac{n - n_0}{n} = \frac{N - N_0}{N} = \frac{1}{N} \sum_{k \neq 0} N_k \ , \tag{4.6}$$

is small, that is $\delta \ll 1$. In this case, we can use the mean-field approximation $\hat{b}_0 = \sqrt{L n_0} \approx \sqrt{L n}$.

As we established earlier, the jump operators $\hat{L}_k$ in momentum basis are given by

$$\hat{L}_k = \sqrt{\frac{\kappa}{L}} \sum_q (e^{-i(q-k)} + 1)(e^{iq} - 1)\hat{b}^\dagger_{q-k}\hat{b}_q \; . \tag{4.7}$$

Only keeping terms up to order $\sqrt{n}$ and observing that the $q = 0$ summand is zero yields

$$\hat{L}_k = 2\sqrt{\kappa n}(e^{ik} - 1)\hat{b}_k + \mathcal{O}(1) \; . \tag{4.8}$$

The prefactor in $\hat{L}^\dagger_k$ is the complex conjugate and since $|2\sqrt{n}(e^{ik} - 1)|^2 = 16n \sin^2\left({}^{k}\!/\!{}_{2}\right)$, we may redefine the jump operator as

$$\hat{L}_k = \sqrt{\kappa_k}\hat{b}_k \quad , \quad \text{with} \quad \kappa_k = 16n\kappa \sin^2\left({}^{k}\!/\!{}_{2}\right) , \tag{4.9}$$

without changing the Lindbladian. Cruicially, since only pairs of jump operators appear in the Lindbladian, this gives the $\mathcal{O}(n)$ approximation to the dissipator. Under the approximation (and discarding boundary effects), the Bose-Hubbard Hamiltonian has the new form

$$\hat{H} = \sum_{k \neq 0} \left\{ (\epsilon_k + Un)\hat{b}^\dagger_k \hat{b}_k + \frac{Un}{2}\left(\hat{b}_k\hat{b}_{-k} + \hat{b}^\dagger_k\hat{b}^\dagger_{-k}\right) \right\} , \tag{4.10}$$

with the single particle energy $\epsilon_k = 4J \sin^2\left({}^{k}\!/\!{}_{2}\right)$. Unfortunately, in this form the Hamiltonian still couples the momenta k and $-k$ with each other, which is why we introduce new creation and annihilation operators $\hat{c}^\dagger_k$, $\hat{c}_k$ connected to the old ones via a unitary relation

$$\begin{pmatrix} \hat{c}_k \\ \hat{c}_{-k} \end{pmatrix} = \frac{1}{\sqrt{2}} \begin{pmatrix} 1 & 1 \\ -1 & 1 \end{pmatrix} \begin{pmatrix} \hat{b}_k \\ \hat{b}_{-k} \end{pmatrix} \; . \tag{4.11}$$

As already said, this transformation does not change the commutation relations. Since the transformation is unitary, the system is furthermore identically described by the jump operators

$$\hat{L}_k = \sqrt{\kappa_k}\hat{c}_k \, , \tag{4.12}$$

and cruicially, the Hamiltonian decouples into

$$\hat{H} = \sum_{k \neq 0} \left\{ (\epsilon_k + Un)\hat{c}^\dagger_k \hat{c}_k + \frac{Un}{2}\left(\left[\hat{c}_k\right]^2 + \left[\hat{c}^\dagger_k\right]^2 \right) \right\} . \tag{4.13}$$

Now, both the Hamiltonian and the jump operators do not couple different k-sectors. As a consequence, we can solve the Lindblad equation individually for every k. The Hamiltonian in a single k-sector can be recast into the matrix form

$$\hat{H}_k = \frac{1}{2} \begin{pmatrix} \hat{c}^\dagger_k & \hat{c}_k \end{pmatrix} \begin{pmatrix} \epsilon_k + Un & Un \\ Un & \epsilon_k + Un \end{pmatrix} \begin{pmatrix} \hat{c}_k \\ \hat{c}^\dagger_k \end{pmatrix} \; , \tag{4.14}$$

with $\hat{H} = \sum_{k \neq 0} \hat{H}_k$. As an ansatz for the steady state we use a mixed state in each k-sector given by

$$\hat{\rho}_k = \mathcal{Z}_k^{-1} \exp\Big(- \beta_k \hat{a}^\dagger_k \hat{a}_k \Big) , \tag{4.15}$$

with new bosonic Bogoliubov creation and annihilation operators, defined through the relation

$$\begin{pmatrix} \hat{c}^\dagger_k & \hat{c}_k \end{pmatrix} = \begin{pmatrix} \hat{a}^\dagger_k & \hat{a}_k \end{pmatrix} \begin{pmatrix} e^{-i\phi_k}\cosh(\theta_k) & -e^{i\phi_k}\sinh(\theta_k) \\ -e^{-i\phi_k}\sinh(\theta_k) & e^{i\phi_k}\cosh(\theta_k) \end{pmatrix} \; . \tag{4.16}$$

The parameters ϕ_k and θ_k are free and the ansatz Eq. (4.15) fulfills the relation

$$\hat a_k \hat\rho_k = \hat\rho_k\, \hat a_k e^{-\beta_k}\ . \tag{4.17}$$

Due to Eq. (4.17), all creation and annihilation operators in the dissipator can be moved to one side of $\hat\rho_k$. This way the Hamiltonian part can be compared to the dissipator later. The condition $\mathcal{L}\hat\rho = 0$ translates to

$$i\big[\hat H,\hat\rho\big] = -\kappa_k\big(\mathbf{d}_{1,1}\hat a_k^\dagger \hat a_k + \mathbf{d}_{2,1}\big[\hat a_k^\dagger\big]^2 + \mathbf{d}_{1,2}\big[\hat a_k\big]^2 + \mathbf{d}_{2,2}\big)\hat\rho_k\,, \tag{4.18}$$

with the coefficient matrix $\mathbf{d}$. The left-hand side is evaluated by writing the Hamiltonian in the new basis

$$\hat H_k = \begin{pmatrix}\hat a_k^\dagger & \hat a_k\end{pmatrix} \mathfrak{H} \begin{pmatrix}\hat a_k \\ \hat a_k^\dagger\end{pmatrix}\ , \tag{4.19}$$

where $\mathfrak{H}$ is a 2×2 matrix. Now, the diagonal elements of this matrix do not contribute to the commutator in Eq. (4.18), as they commute with $\hat\rho$. Eq. (4.17) implies the commutation relations $\Big[\big[\hat a_k\big]^2,\hat\rho\Big] = (1-e^{2\beta_k})\big[\hat a_k\big]^2\hat\rho$ and $\Big[\big[\hat a_k^\dagger\big]^2,\hat\rho\Big] = (1-e^{-2\beta_k})\big[\hat a_k^\dagger\big]^2\hat\rho$, and calculating the full commutator with the Hamiltonian yields two linearly independent equations over the coefficients

$$1.\quad \mathrm{e}^{-\beta_k}\cosh^2\theta_k - \sinh^2\theta_k = 0\ , \tag{4.20}$$

$$2.\quad \mathrm{i}\big(1-\mathrm{e}^{-2\beta_k}\big)\mathfrak{H}_{12} = \frac{\kappa_k}{2}\sinh\theta_k\cosh\theta_k\big(1-\mathrm{e}^{-\beta_k}\big)^2\ , \tag{4.21}$$

where $\mathfrak{H}_{12} = -(\epsilon_k + Un)\sinh\theta_k\cosh\theta_k + \frac{Un}{2}\big(\mathrm{e}^{2\mathrm{i}\phi_k}\sinh^2\theta_k + \mathrm{e}^{-2\mathrm{i}\phi_k}\cosh^2\theta_k\big)$. With a little bit of algebra, the first constraint Eq. (4.20) is rearranged into

$$\cosh\big(2\theta_k\big) = \coth\big({}^{\beta_k}\!/_2\big)\ , \tag{4.22}$$

where we used the explicit form of the arcoth and $2\cosh^2(x) = \cosh(2x)+1$. The second constraint Eq. (4.21) can be split up into two separate equations by considering the real and imaginary part individually

$$\text{(I)}\quad -2(\epsilon_k+Un)\sinh(\theta_k)\cosh(\theta_k) + Un\cos(2\phi_k)\big(\sinh^2(\theta_k)+\cosh^2(\theta_k)\big) = 0\ , \tag{4.23}$$

$$\text{(II)}\quad \sin(2\phi_k)\big(1-e^{-2\beta_k}\big)(\epsilon_k+Un) = \frac{\kappa_k}{2}\sinh(\theta_k)\cosh(\theta_k)\big(1-e^{-\beta_k}\big)^2\ . \tag{4.24}$$

Again, with a little bit of algebra, Equation (4.23) translates to

$$\cos(2\phi_k) = \frac{\epsilon_k+Un}{Un}\tanh(2\theta_k)\,. \tag{4.25}$$

Inserting this into Equation (4.24) and rearranging yields

$$\cot(2\phi_k) = \frac{\epsilon_k+Un}{\big({}^{\kappa_k}\!/_2\big)}\ , \tag{4.26}$$

which is the first final equation. To express θ_k in terms of system parameters, we insert Eq. (4.26) back into Eq. (4.25) and get

$$\cosh^2\big(2\theta_k\big) = \coth^2\big({}^{\beta_k}\!/_2\big) = \frac{\big({}^{\kappa_k}\!/_2\big)^2 + \big(\epsilon_k+Un\big)^2}{\big({}^{\kappa_k}\!/_2\big)^2 + E_k^2}\ , \tag{4.27}$$

where we defined $E_k^2 = \epsilon_k^2 + 2Un\epsilon_k$, which is the corresponding Bogoliubov energy. Indeed, Eq. (4.26) and (4.27) determine the steady state completely. It remains to be shown that the two equations admit solutions in the parameter regions we are interested in.

4.2.1 Validity of the mean-field approximation

As already pointed out, it is imperative to check whether Eq. (4.26) and (4.27) have physical solutions. Otherwise, the Gaussian ansatz Eq. (4.15) is not sufficient and the steady state has a different form. Summarizing, we are interested in the following two questions.

1. In which parameter regime are Equation (4.26) and (4.27) solvable.
2. In which parameter regime is the constraint $\delta \ll 1$ actually fulfilled.

We will first discuss question 1. Equation (4.26) always has a solution, since cot : $(0, \pi) \to \mathbb{R}$ is bijective. Equation (4.27) on the other hand is more involved. Since $\cosh^2$ and $\coth^2$ map to $[1, \infty)$, the right-hand side needs to lie in this interval as well. The nominator is strictly positive and always greater than the denominator and a solution therefore exists if the denominator is strictly positive. Considering specific parameter regimes, this is fulfilled if $J, U \geq 0$. Only the case with $J \geq 0$ and $U < 0$ is tricky and we need to insert the explicit expressions for all quantities to find the constraint

$$\sin^2\left({}^{k}\!/\!_{2}\right) > \frac{|U|Jn}{J^2 + \left(2n\kappa\right)^2} \;, \quad \forall\, k > {}^{2\pi}\!/\!_{L} \;. \tag{4.28}$$

Note that this condition is especially fulfilled in two interesting limits

1. if $\kappa \to \infty$ for arbitrary large (but constant) L and $|U|$,
2. if $N \to \infty$ for arbitrary large (but constant) L and $|U|$.

In both these limits, the Gaussian state is the steady state for arbitrary large $|U|$.

It remains to be shown that the depletion of the steady state is small. Since the steady state describes the non-condensed bosons (the condensed ones are taken into account in the mean-field) we just need to compute the particle number in the steady state. We start by calculating the number of $\hat{c}_k^\dagger$-quasiparticles N_k^c in the system. We use Eq. (4.16) to find

$$N_k^c = \mathcal{Z}^{-1}\mathrm{Tr}\Big(\hat{c}_k^\dagger \hat{c}_k e^{-\beta_k \hat{a}_k^\dagger \hat{a}_k}\Big) = \left(\cosh^2\theta_k + \sinh^2\theta_k\right)\mathcal{Z}^{-1}\mathrm{Tr}\Big(\hat{a}_k^\dagger \hat{a}_k e^{-\beta_k \hat{a}_k^\dagger \hat{a}_k}\Big) + \sinh^2\theta_k \;, \tag{4.29}$$

where we used the definition of $\hat{a}_k^\dagger$, $\hat{a}_k$, the conservation of Bogoliubov-particle number $\hat{a}_k^\dagger \hat{a}_k$ in the steady state. With the Bose-Einstein statistics and Eq. (4.27) we find

$$N_k^c = \frac{1}{2}\Big(\cosh\left(2\theta_k\right) + 1\Big)\Big(\cosh\left(2\theta_k\right) - 1\Big) = \frac{1}{2}\frac{(Un)^2}{\kappa_k^2 + E_k^2} \;. \tag{4.30}$$

Now the relation $\hat{b}_k^\dagger \hat{b}_k + \hat{b}_{-k}^\dagger \hat{b}_{-k} = \hat{c}_k^\dagger \hat{c}_k + \hat{c}_{-k}^\dagger \hat{c}_{-k}$ implies that $\sum_{k\neq 0} N_k = \sum_{k\neq 0} N_k^c$, where N_k denotes the number of $\hat{b}_k^\dagger$-bosons. Thus, the condensate depletion is given by

$$\delta = \frac{1}{N}\sum_{k\neq 0} N_k^c = \frac{1}{2N}\sum_{k\neq 0}\frac{(Un)^2}{\kappa_k^2 + E_k^2} = \tag{4.31}$$

$$= \frac{1}{N}\sum_{k\neq 0}\frac{(Un)^2}{32\big(16(n\kappa)^2 + J^2\big)\sin^4\left({}^{k}\!/\!_{2}\right) + 16UnJ\sin^2\left({}^{k}\!/\!_{2}\right)} \;. \tag{4.32}$$

Although this expression looks involved, we can analyze its behavior in certain limits. If $N \to \infty$

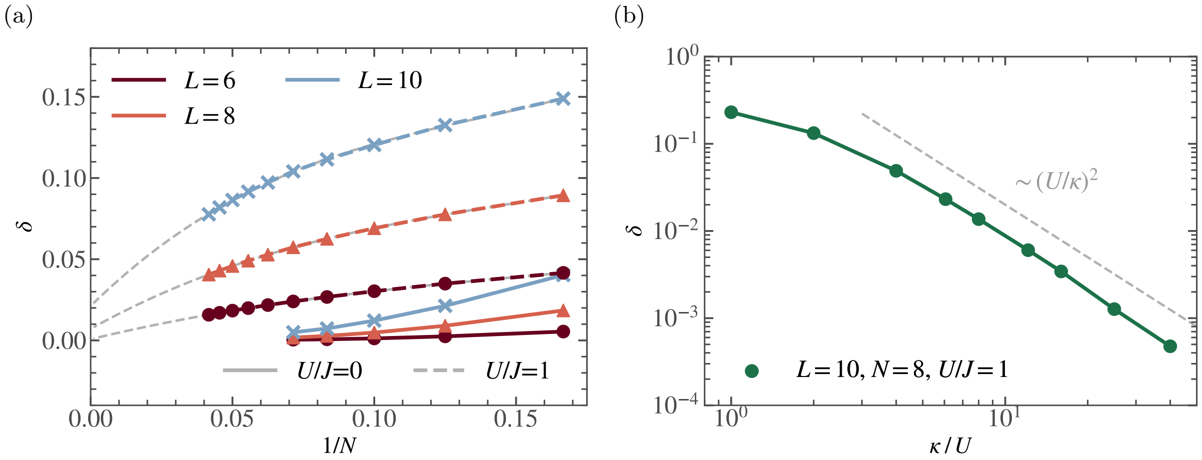

Figure 12: Condensate depletion δ for the full dissipative preparation of a BEC according to Eq. (3.1). Panel a): We show the dependence of the condensate depletion Eq. (4.6) on the number of bosons N for various L and U/J. Especially for $U/J > 0$ and $L = 6, 8$ we recover the mean-field predicted linear scaling of the depletion Eq. (4.33). We set $\kappa/J = 2$. Panel b): Condensate depletion depending on dissipation κ/U with coefficients specified in the plot. Upon increasing κ, the depletion decreases quadratically as predicted by Eq. (4.34). All steady states were obtained by performing a time evolution until sufficient convergence is reached. All calculations were performed with the parameters $J = 1$, as well as $k_0 = 0$. The local dimension was set to $d = N + 1$. For further details on the numerical implementation see App. A.1. The figures are adapted from [1].

and L is constant, the denominator in Eq. (4.32) is dominated by n^2 and the whole sum is of order $\mathcal{O}(1)$, leading to

$$\delta = \mathcal{O}\big(1/N\big). \tag{4.33}$$

If instead $\kappa \to \infty$ at constant L we get

$$\delta = \mathcal{O}\big((U/\kappa)^2\big). \tag{4.34}$$

Equation (4.33) and (4.34) can be verified numerically for the full Lindbladian Eq. (3.1), as shown in Fig. 12. Both the scaling in particle number N (Fig. 12a) as well as the scaling with κ/U (Fig. 12b) matches the mean-field predictions, suggesting that the mean-field treatment in these limits is valid. In particular, Fig. 12b underscores the beneficial controllability of the condensate density through dissipative parameters like κ. The finite depletion in Fig. 12a in case of $U/J = 0$ comes from boundary effects which vanish in the thermodynamic limit.

These two limits give good intuition on how to tune the system parameters such that a good condensation is reached. Especially the second limit Eq. (4.34) opens a possibility to experimentally counteract localization effects caused by the onsite interaction. However, care must be taken when discussing the limit $\kappa \to \infty$, since the Born approximation is not valid any more (c.f. Sec. 2.1). Nevertheless, in Fig. 12b we find the scaling Eq. (4.34) also at intermediate κ/U.

After verifying the validity of the mean-field analysis, we can discuss if the steady state can be interpreted as a thermal state of some effective Hamiltonian, due to its Gaussian form. We are mainly interested in the physical system the effective Hamiltonian corresponds to and we address these questions in the next sections.

4.2.2 Connection to finite-temperature isolated systems

Equation (4.15) has the form of a thermal state of some effective Hamiltonian $\sum_{k\neq 0}\beta_k\hat{a}_k^\dagger\hat{a}_k$ and we would like to understand the physical meaning of this connection. For this, we need to find an effective isolated system with Hamiltonian $\hat{H}_{\text{eff}}$ at some finite temperature T_{eff} that gives rise to a thermal state similar to the dissipative steady state.

The key difference to an isolated system is the appearance of the dissipation strength κ in the central Equation (4.27). However, by appropriately rescaling the onsite interaction the dissipation gets absorbed. This procedure is made possible by the similarity in the k-dependence between ϵ_k and κ_k. Precisely, we have,

$$\kappa_k = \frac{4n\kappa}{J}\epsilon_k\,, \tag{4.35}$$

and by rescaling U according to

$$\tilde{U} = (1+a^2)^{-1}\,U\,, \tag{4.36}$$

where we defined the rescaling parameter $a = {}^{4n\kappa}\!/_{J}$, Equation (4.27) takes the form

$$\coth^2\left({}^{\beta_k}\!/_2\right) = 1 + \frac{(Un)^2}{1+a^2}\frac{1}{\tilde{E}_k^2}\,, \tag{4.37}$$

with the new Bogoliubov energy $\tilde{E}_k = \sqrt{\epsilon_k^2 + 2\tilde{U}n\epsilon_k}$. We want to recover an effective temperature T_{eff} such that $\beta_k = {}^{\tilde{E}}\!/_{T_{\text{eff}}}$. Then, the dissipative system would be indistinguishable from an effective isolated Bose-Hubbard model (with rescaled on site interaction $\tilde{U}$) at finite temperature T_{eff}. For this, we rearrange Eq. (4.37) to find

$$\beta_k = \ln\left(\frac{\sqrt{x}+1}{\sqrt{x}-1}\right)\,, \qquad x = 1 + \frac{(Un)^2}{1+a^2}\frac{1}{\tilde{E}_k^2}\,, \tag{4.38}$$

where we used the explicit form of the inverse of coth. Expanding the logarithm around 1 for $x \gg 1$ gives

$$\beta_k = \frac{2}{\sqrt{x}} + \mathcal{O}(x^{-1})\,. \tag{4.39}$$

Now, expanding the square root gives the final expression

$$\beta_k = \frac{\tilde{E}_k}{T_{\text{eff}}}\,, \qquad T_{\text{eff}} = \frac{UJn}{2\sqrt{J^2 + \left(4n\kappa\right)^2}}\,. \tag{4.40}$$

Consequently, the steady state Eq. (4.15) is indistinguishable from the thermal state of an effective Bose-Hubbard model $\hat{H}_{\text{eff}}$ at effective temperature T_{eff}. This effective Hamiltonian is given by

$$\hat{H}_{\text{eff}} = \sum_k(\epsilon_k + \tilde{U}n)\hat{b}_k^\dagger\hat{b}_k + \frac{\tilde{U}n}{2}\left(\left[\hat{b}_k\right]^2 + \left[\hat{b}_k^\dagger\right]^2\right)\,, \tag{4.41}$$

with rescaled interaction $\tilde{U}$. Especially the mixed states $\hat{\rho}_k$ with $k \ll {}^{\sqrt{UJ}}\!/_{\kappa}$ are well described by this approximation, as $\tilde{E}_k \to 0$ at $k \to 0$. We want to emphasize that besides the zero momentum mode, small k modes are filled the most in the effective isolated, as well as in the real dissipative system Eq. (3.1). As a consequence, we also expect the approximation to work well in the setting where only a few k fulfill the constraint $k \ll {}^{\sqrt{UJ}}\!/_{\kappa}$ and the approximation makes sense for the full state $\hat{\rho}$, although not all k satisfy the constraint. Note that for any

$\kappa > 0$ we have $\tilde{U} < U$, so the dissipation acts as an *effective reduction of the onsite interaction* U.

We stress that some of these observations are not included in [17], which mostly considers the zero-th order in κ (consequently T_{eff} does not depend on κ, and $\hat{H}_{\text{eff}} = \hat{H}$).

4.2.3 Connection to zero-temperature isolated systems

Equation (4.40) especially holds in the limit $\kappa < U$, while the limit $\kappa \gg U$ can be treated similarly and has great importance, since in experiment a large κ is desirable to increase the condensate fidelity.

To study this limit properly, we first need to briefly consider the isolated case. Here, the bosonic Bogoliubov operators are given by $\hat{d}_k = \cosh\gamma_k\, \hat{c}_k + \sinh\gamma_k\, \hat{c}_k^\dagger$ and γ_k is related to the system parameters as

$$\cosh^2(2\gamma_k) = 1 + \frac{(U_{\text{iso}}\, n)^2}{E_k^2}\ , \tag{4.42}$$

where $E_k = \sqrt{\epsilon_k^2 + 2U_{\text{iso}} n \epsilon_k}$ and we denote the onsite interaction by U_{iso} to avoid confusion. The zero-temperature equilibrium state is the groundstate of the Hamiltonian given by the vacuum of Bogoliubov quasiparticles, $|\text{vac}(\hat{d})\rangle$. The particle number can be calculated easily by first considering the rotated particle basis $\hat{c}_k$ and inserting Eq. (4.42)

$$N_k^{T=0} = \langle\text{vac}(\hat{d})|\, \hat{c}_k^\dagger \hat{c}_k\, |\text{vac}(\hat{d})\rangle = \frac{1}{2}\left(\sqrt{1 + \frac{(U_{\text{iso}}\, n)^2}{E_k^2}} - 1\right) = \frac{1}{4}\frac{(U_{\text{iso}}\, n)^2}{E_k^2}\ , \tag{4.43}$$

where we used the assumption $U_{\text{iso}} \ll J$ in the last equality, as well as $L = \text{const}$. This equation looks quite similar to the individual terms in the condensate depletion Eq. (4.31). We only need to find the matching U_{iso} at which the condensate depletions in the isolated equals the dissipative system Eq. (4.32). Considering the limit of low interaction $U_{\text{iso}} \ll J/(NL)$, we can neglect some terms in the denominator and finally obtain for the isolated system at $T = 0$

$$N_k^{T=0} = \frac{(U_{\text{iso}}\, n)^2}{4J^2} \frac{1}{16\sin^4(k/2)} + \mathcal{O}\big((U_{\text{iso}}\, n/\epsilon_k)^3\big)\ . \tag{4.44}$$

In the dissipative case, we can start from Eq. (4.32) and approximate the particle number N_k^κ similarly for each k in the limit $\kappa \gg U$ as

$$N_k^\kappa = \frac{(Un)^2}{2(J^2 + 4n^2\kappa^2)} \frac{1}{16\sin^4(k/2)}\ . \tag{4.45}$$

Comparing the coefficients in Eq. (4.44) and (4.45) we can find the U_{iso} an isolated system at zero-temperature needs in order to generate the same depletion as the dissipative Bose-Hubbard model with κ

$$U_{\text{iso}} = \sqrt{2}\frac{U}{\sqrt{1+a^2}}\ , \tag{4.46}$$

implying that $\delta_{T=0}(U_{\text{eff}}) = 1/N \sum_k N_k^{T=0} = 1/N \sum_k N_k^\kappa = \delta_\kappa(U)$. Interestingly, the equality holds component-wise for the condensed particles in each k sector, $N_k^{T=0} = N_k^\kappa$. As we will show in the next section, this also implies that

$$\text{Tr}\big(\hat{c}_k^\dagger \hat{c}_{k'} \hat{\rho}_{\text{ss}}\big) = \langle\text{vac}(\hat{d})|\, \hat{c}_k^\dagger \hat{c}_{k'}\, |\text{vac}(\hat{d})\rangle\ , \tag{4.47}$$

showing equality of the two point correlation functions, which determine correlations in the steady state. This analysis implies, that the dissipative driving effectively cools down the system, eventually reaching low temperatures inaccessible to current methods.

4.2.4 Correlation structure of the steady state

We are also interested in the one-body reduced density matrix (OBDM), which is often referred to as the correlation function and defined as

$$\gamma_{ij} = \langle \hat{b}_j^\dagger \hat{b}_i \rangle_{\mathrm{ss}} = \mathrm{Tr}\big(\hat{b}_j^\dagger \hat{b}_i \hat{\rho}_{\mathrm{ss}}\big) = \langle\!\langle \mathbb{1} | \hat{\mathbb{1}} \otimes (\hat{b}_j^\dagger \hat{b}_i) | \rho_{\mathrm{ss}} \rangle\!\rangle \,. \tag{4.48}$$

While its leading eigenvalue is connected to the number of condensed bosons, its off-diagonal elements contain information about the correlations in the system. The off-diagonal elements of γ behave like

$$\gamma_{ij} = \frac{c_1}{|i-j|^{c_2}} \mathrm{e}^{-|i-j|/\xi} + c_3 \,. \tag{4.49}$$

Here, $c_3 > 0$ implies long-range order, $c_2 > 0$ quasi-long-range order, and $\xi < \infty$ short-range order. ξ is termed the correlation length. For instance in a Mott-insulating phase the off-diagonal elements decay exponentially, while they approach a constant in the superfluid BEC phase [127].

The notion of long-rang order only makes sense in the thermodynamic limit. At finite system sizes L, a true long-range order is indistinguishable from a slow exponential decay $\xi > L$. Consequently, we can speak of the emergence of a BEC on lengthscales of the system, if the exponential decay is slower than the system size, $\xi > L$. We often refer to this state as a *lattice BEC* or *local BEC*.

We can probe the behavior of the OBDM by evaluating it in the mean-field approximation. Since the Lindbladian is almost diagonal in momentum space, γ is directly connected to the depletion Eq. (4.31) yielding

$$\gamma_{lm} = n_0 + \frac{1}{L} \sum_{k \neq 0} \frac{(Un)^2}{2(1+a^2)E_k^2} \mathrm{e}^{\mathrm{i}(l-m)k} \,. \tag{4.50}$$

This simple structure is owed to the fact in the $\hat{c}_k$ basis, different momenta are decoupled and γ is diagonal. To understand the dependence on system parameters better, we can use a naive bound on the sum to find

$$\gamma_{lm} > n(1-2\delta) = n - \mathcal{O}\big((U/\kappa)^2\big) \,, \tag{4.51}$$

which reveals the emergence of long-range order for high κ, or equivalently N, at finite L. In Fig. 13a we show results from a simulation with the full Lindbladian Eq. (3.1) for 10 sites and 8 particles at parameters $U = J = 1$. We plot the deviation of the off-diagonal element γ_{L1} from the mean value n and recover the quadratic scaling predicted by Eq. (4.51). Additionally, in Fig. 13b we plot the off-diagonal elements γ_{2j} for the same system, at multiple dissipations κ. While for $\kappa = 2$ the exponential decay is clearly visible, at higher κ it is indistinguishable to a long-range correlated state and a lattice BEC forms.

It remains to be discussed if the states prepared with the dissipative preparation are real BECs in the thermodynamic limit. A BEC is defined through an extensive scaling of the leading eigenvalue of the OBDM when approaching the thermodynamic (TD) limit [127]. Looking at Eq. (4.32), in the TD limit (assuming constant density), that is, $L, N \to \infty$ while n, J, U, κ are kept constant, we recover a Riemann sum

$$\delta = \frac{1}{2N} \sum_{k \neq 0} \frac{(Un)^2}{\kappa_k^2 + E_k^2} \longrightarrow \frac{1}{2n} \int_{1\mathrm{BZ}} \frac{(Un)^2}{\kappa_k^2 + E_k^2} \frac{\mathrm{d}k}{v_0} \,, \tag{4.52}$$

where v_0 denotes the volume of the 1BZ [17]. Since the denominator diverges quadratically for $k \to 0$, the integral diverges in one and two dimensional systems, and we expect the mean-field

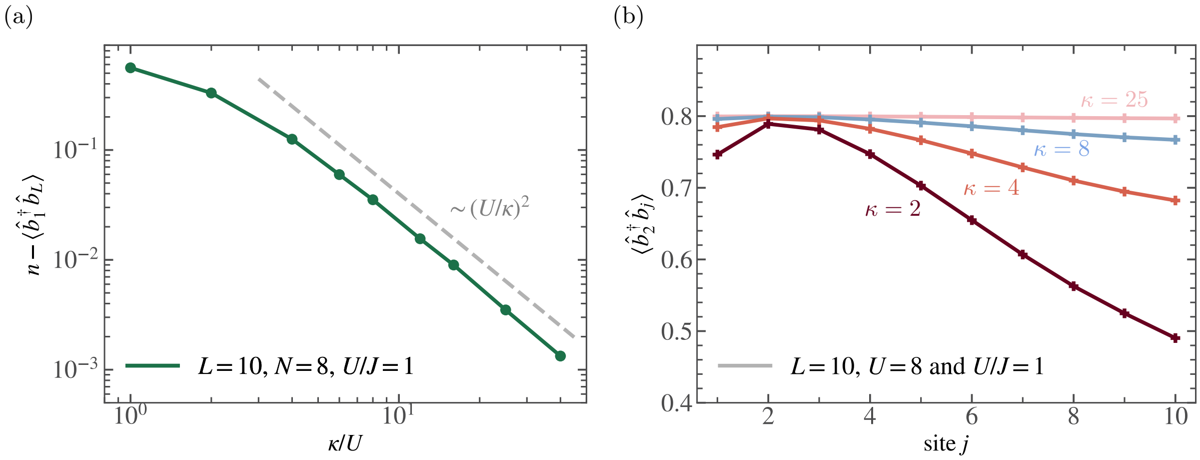

Figure 13: Simulating the full dissipative preparation Eq. (3.1) of a BEC for 10 sites, 8 particles, $U = J = 1$, and $k_0 = 0$. Panel a): We show the deviation of the off-diagonal element γ_{1L} from the mean value n for several κ/U. We recover the scaling predicted in Eq. (4.51), showing that the steady state features a lattice analogue of a long-range order. Panel b): Off-diagonal elements of the OBDM γ_{2L} for four different κ. With increasing κ, the decay is smoothed out, until the behavior is indistinguishable from a true long-range correlation. The local dimension was set to $d = N + 1$. For more details on the numerical implementation see App. A.1. The figures are adapted from [1].

analysis to break down in the TD limit. This also implies that in one and two dimensions, the dissipative preparation does not produce a true BEC. Rather, as we reasoned before, it prepares a state which features high condensation in certain parameter regimes and is indistinguishable from a long-range correlated state in finite systems. Since we are mostly interested in the experimental realization on optical lattices, which are not at the TD limit when it comes to the number of sites, the formation of a local BEC suffices. Note that in three dimensions, the integral is finite and condensation may occur at positive $U > 0$ also in the TD limit [17].

We can check that we do not recover a full BEC by again considering the off diagonal elements of the OBDM. As discussed previously, in a superfluid phase we expect an extensively scaling correlation length $\xi(L) = \mathcal{O}(L)$, while an insulating phase is characterized by a saturating correlation length, $\xi(L) = \mathcal{O}(1)$ [127, 128]. To capture an intermediate algebraic as well as an exponential decay, we fit the off diagonal $\gamma_{i_0 j}$ at a fixed site i_0 with the asymptotic behavior Eq. (3.42) with the constraint that c_1, c_2, c_3 and ξ need to be positive.

In Fig. 14a we show the correlation length ξ for different system sizes L at constant particle density $n = 0.5$ for different finite U/J at $\kappa/J = 2$. We directly see that the correlation length is monotonic in U, increasing with decreasing $|U|$ as we expect. Nevertheless, it saturates with increasing L for all finite U, indicating that a short-range correlated phase appears. Notice however, that at $L = 10$ and $U/J = 0.5$, ξ is bigger than the system size (gray dotted line), indicating that the state looks like a BEC on all accessible lengthscales, and we speak of a local BEC. As the system size increases, this local BEC disappears, reminiscent of a phase transition. This transition also has implications for the spectrum of the Lindbladian as we discuss in Sec. 4.3. The system therefore exhibits a critical point at $U = 0$, and we can extract the critical exponent α associated with divergence of ξ as $U \to 0$ by a fit with the ansatz

$$\xi(U/J) = a(U/J)^{-\alpha}\,, \tag{4.53}$$

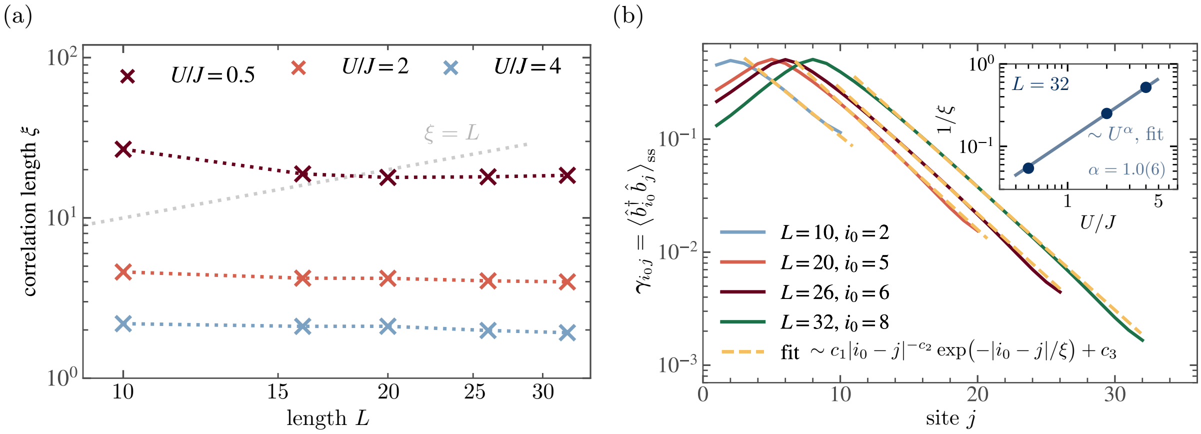

Figure 14: Simulating the full dissipative preparation of a BEC Eq. (3.1) for large system sizes. Panel a): Correlation length ξ (c.f. Eq. (4.49)) in dependence of the system size for different U/J at $\kappa/J = 2$. In all cases, the correlation length approaches a constant value upon increasing L. Panel b): Off-diagonal elements of the OBDM for different lengths at $U/J = \kappa/J = 2$. The off-diagonal elements decay exponentially and the correlation length ξ can be extracted by fitting with Eq. (3.42) (indicated as gray dotted lines). Note that the fitting lines are almost parallel, indicating equal ξ. Inset: Dependence of the correlation length ξ on U/J for $L = 32$. We fit with the power-law ansatz Eq. (4.53) and extract the critical exponent $\alpha = 1.06 \pm 0.02$. All steady states were obtained using CLIK-MPS and convergence was guaranteed using the methods presented in Sec. 3.2. At $L = 32$ we used $T = 32$ and $\delta t = 0.4$, at $L = 26$, $T = 22$ and $\delta t = 0.4$, at $L = 20$, $T = 18$ and $\delta t = 0.2$, at $L = 16$, $T = 10$ and $\delta t = 0.1$, while at $L = 10$ we used $T = 6$, $\delta t = 0.1$. For $L = 32$, $L = 26$, $L = 20$, and $L = 16$ sites we used the complex angle $\alpha = 0.02$, while for $L = 10$ we employed $\alpha = 0.05$. All calculations were performed at $J = 1$ and half filling $N/L = 0.5$, as well as $k_0 = 0$. The local dimension was set to $d = N + 1$. For more details on the numerical implementation, see App. A.1. The figures where adapted from [2].

where $\xi(\bullet)$ is the correlation length in the thermodynamic limit. In the inset of Fig. 14b we extrapolate the correlation length of the $L = 32$ data according to Eq. (4.53). We recover a critical exponent $\alpha = 1.06 \pm 0.02$. This is a typical sign of a phase transition between a short-range and a long-range correlated state. Our analysis suggests, that if the system parameters are chosen correctly, one can achieve a finite lattice analogue of a BEC with the dissipative preparation protocol. In Fig. 14b we lastly present the off diagonal elements of the OBDM for a number of system sizes, used to extract the correlation lengths shown in Fig. 14a. We also provide the fit according to Eq. (3.42) and see the exponential decay clearly.

4.3 Transport and finite-size scaling

In the preceding sections we analyzed the properties of the steady state both through a mean-field and numerical analysis and we found a critical point at $U = 0$ [69, 17, 1], where a true BEC is stabilized, while at small U a local BEC emerges. Indeed, we established that this critical point is characterized by a diverging correlation length and we extracted the critical exponent $\alpha = 1.0(6)$ from fitting the correlation function. In the context of open quantum systems there is a class of phase transitions, so called dissipative phase transition (DPT), whose critical points are characterized by the closing of the dissipative gap, implying that the relaxation timescales of the system diverge in the thermodynamic limit [3, 5]. In close analogy to DPTs, we can ask if the critical point observed in the dissipative Bose-Hubbard model has an influence on the long time behavior of the system.

To investigate the behavior of the dissipative gap, we employ CLIK-MPS and approximate the dissipative gap $\Delta = -\mathrm{Re}\,\lambda_2$ at several different lengths of the system at half filling $N/L = 0.5$. The particle number conservation, combined with the Lindbladian being local enforces $\Delta \to 0$ for $L \to \infty$ and the asymptotic scaling relation is of the form [97]

$$\Delta(L) = \frac{a}{L^z}\,, \tag{4.54}$$

where we introduced the dynamical exponent z. Note that there is a close connection between the transport properties of the system and the scaling $\Delta(L)$ [97]. Using Eq. (4.54) we perform a finite-size extrapolation of the dissipative gap and extract the dynamical exponent depending on the onsite interaction U/J. In Figure 15, we show the finite-size scaling of the dissipative gap for the Bose-Hubbard model Eq. (3.1). We consider three onsite interaction strengths, $\kappa/J = 2$ and system sizes up to $L = 32$. We obtain the dissipative gap using CLIK-MPS and we guarantee convergence as discussed in Sec. 3.3.2. Note that for the fits we excluded the smallest system with $L = 16$ sites in order to reliably identify the gap closing. Interestingly, we observe a change in the scaling behavior of $\Delta(L)$ from a dominating linear scaling $z = 1.00 \pm 0.05$ for large interactions (c.f. the $U = 0.66$ data) to a scaling $z = 1.59 \pm 0.17$ in the limit $U = 0$. We interpret this as an additional signature of the increasing correlation length when approaching $U = 0$. At vanishing onsite interaction, the dynamics is governed by the coherent hopping term and the dissipation. Representing the bosonic operators as $\hat{b}_j^\dagger = \sqrt{\hat{\rho}_j}\exp\left(\mathrm{i}\hat{\theta}_j\right)$ [129, 17], we can rewrite the jump operator $\hat{L}_j$. They feature a term $\mathrm{i}\hat{\rho}_j\left(\hat{\theta}_{j+1} - \hat{\theta}_j\right)$ [17], which couples local phase fluctuations (c.f. $\hat{\theta}_{j+1} - \hat{\theta}_j$) to the local bosonic density (c.f. $\hat{\rho}_j$). We propose that this coupling leads to non-linear interactions which are a signature of the KPZ universality class. This universality class was first introduced in the study of the growth of interfaces and surfaces [130]. The universality class is described by a partial stochastic differential equation for the function $h(x,t)$, given by

$$\frac{\partial h}{\partial t} = \nu\nabla^2 h + \frac{\lambda}{2}\left(\nabla h\right)^2 + \eta(x,t)\,, \tag{4.55}$$

where ν, λ are constants and η is Gaussian white noise. In the last decades, it also attracted interest in quantum systems, where the KPZ universality class was observed in exciton-polariton condensates [131], other bosonic systems [132], or a one-dimensional Heisenberg chain [133]. The KPZ universality class is characterized by a dynamical exponent $z = 3/2$, in agreement with the numerical data found in our simulations.

On the other hand, for strong onsite interactions the particle coherence length ξ is smaller than the overall system size as discussed in Sec. 4.2.4 and incoherent scattering is pronounced, indicating a transition to a diffusive regime where $z = 1$.

We therefore find a picture in which the critical point is accompanied by a KPZ scaling. Interestingly, also for the system at $U/J = 0.16$, we observe a dynamical exponent $z = 1.48 \pm 0.03$,

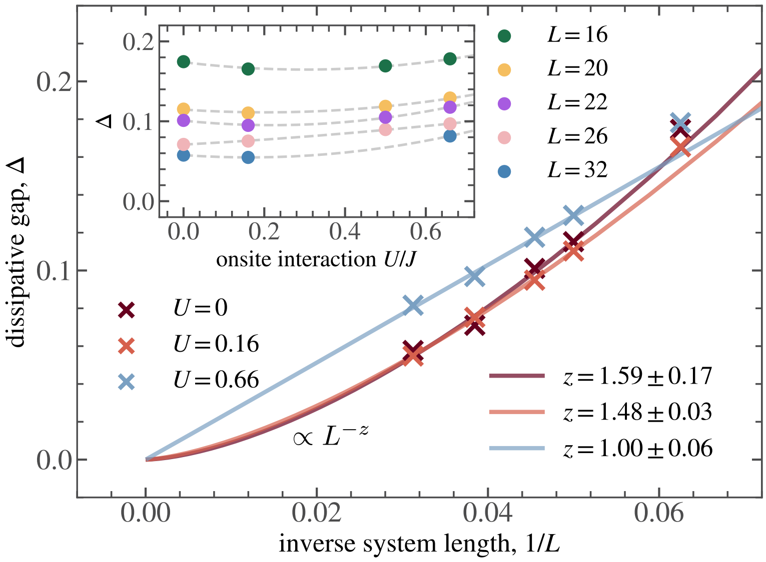

Figure 15: Dissipative gap Δ of the Bose-Hubbard Lindbladian Eq. (3.1) and finite-size scaling. We show Δ for $L = 16$ up to $L = 32$ at half filling $N/L = 0.5$ for several U/J at $\kappa/J = 2$. We extrapolate the finite-size data using Eq. (4.54) and extract the dynamical exponent z. Inset: Dissipative gap depending on U for the same system parameters as before, with quadratic fits. For $L = 16$ and 20, we use $\delta t = 0.2$ and $T = 18, 28$, respectively, while for $L = 22$ and 26 we have $\delta t = 0.4$ and $T = 40$ and 50, respectively. For $L = 32$, $\delta t = 0.6$ and T was chosen U-dependent to ensure convergence (c.f. Fig. 9b). This figure is adapted from [2].

which suggests a KPZ scaling. Using the critical scaling for ξ from Eq. (4.53), we can predict the correlation length at $U/J = 0.16$ to be $\xi \approx 60$. Since this is much larger than the system sizes we look at, incoherent scattering is suppressed compared to the non-linear interactions appearing in the dissipator, and we get a KPZ scaling. However with increasing system size, the incoherent scattering is enhanced and $\xi/L \to 0$, leading to a diffusive scaling $z = 1$ in the thermodynamic limit. The numerical results thus suggest a picture, where the scaling behavior strongly depends on the correlation length

$$\Delta(L) \sim \begin{cases} L^{-1} & \text{if } \xi \ll L,\ \kappa \neq 0\,, \\ L^{-3/2} & \text{if } \xi \gg L,\ \kappa \neq 0\,. \end{cases} \tag{4.56}$$

Note that this is not the whole story, since in the limit κ/J, $U/J \to 0$ the system is described by a non-interacting Hamiltonian featuring ballistic transport $z = 2$. This reveals, that there are additional regimes and the situation is a bit more complicated than Eq. (4.56). The theoretical and numerical exploration of the transport properties seem very intriguing and the rigorous formulation of the arguments given in this section will be subject to future research.

Aside from the theoretical importance of the large system size scaling, the observation, that the dissipative gap closes (quicker than) linearly, is interesting as well. It implies a (super-) linear scaling of the characteristic time for a random to converge to the steady state. This further highlights the necessity of speeding up the dissipative protocol. Before we do so, we investigate some further useful properties of the dissipative Bose-Hubbard model in the next section.

4.4 Unitary equivalences between different Lindbladians

After we addressed the mean-field treatment for the zero-momentum case in great detail, we want to discuss if this analysis carries over to the finite characteristic momentum case. In this section we will show that there is a strong equivalence between the Lindbladians at different k_0, ultimately implying that the steady state properties are almost independent of the characteristic momentum k_0.

Besides the parameters U, J and κ controlling the competion between different Lindbladian terms, the Lindbladian also depends on the targeted momentum k_0. Intuitively, k_0 dictates the momentum which is occupied the most. Other than that, its influence on the Lindbladian structure is not immediately clear. To understand it, we will construct suitable transformations, mediated through unitary superoperators, with the goal of uniting the spectral properties of the seemingly different Lindbladians.

Due to the intuitive meaning of k_0, it seems reasonable to introduce a transformation, which shifts the bosonic momentum by $-k_0$. Then, the condensation should again happen in the zero-momentum mode and we can compare all Lindbladians. Rigorously speaking, we introduce a transformation mediated through the unitary $\hat{U}_{-k_0}$, which acts on creation operators as

$$\hat{U}_{-k_0} \hat{b}_j^\dagger \hat{U}_{-k_0}^\dagger = \mathrm{e}^{-ik_0 j} \hat{b}_j^\dagger \, . \tag{4.57}$$

To identify the transformation behavior of the Lindbladian, we study the Hamiltonian and jump operators separately. The Hamiltonian transforms as

$$\hat{U}_{-k_0} \hat{H}_{k_0}(J,U) \hat{U}_{-k_0}^\dagger = \hat{H}_{k=0}\big(\sigma_{k_0} J, U\big) \, , \tag{4.58}$$

and the jump operators obey

$$\hat{U}_{-k_0} \hat{L}_j^{k=k_0} \hat{U}_{-k_0}^\dagger = \hat{L}_j^{k=0} \, . \tag{4.59}$$

To act on the Lindbladian, we need to work in the vectorized framework. Here, the unitary is given by $\hat{\mathcal{U}}_{k_0} = \hat{U}_{k_0} \otimes \hat{U}_{k_0}^*$ as discussed in Sec. 2.3. Indeed, if we act with the unitary on some density matrix and vectorize the whole expression, we find

$$\hat{U}_{-k_0} \hat{\rho} \hat{U}_{-k_0}^\dagger \to \big(\hat{U}_{-k_0} \otimes \hat{U}_{-k_0}^*\big) |\rho\rangle\!\rangle \, . \tag{4.60}$$

Now we can use Eq. (4.58) and (4.59) and act with $\hat{\mathcal{U}}_{-k_0}$ on the Lindbladian (we write the parameter dependence explicitly here)

$$\hat{\mathcal{U}}_{-k_0} \hat{\mathcal{L}}_{k_0}(J,U,\kappa) \hat{\mathcal{U}}_{-k_0}^\dagger = \hat{\mathcal{L}}_0(\sigma_{k_0} J, U, \kappa) \, . \tag{4.61}$$

This implies that the Lindbladian at characteristic momentum k_0 and coefficients (J,U,κ) is the same as the Lindbladian at 0 with coefficients $(\sigma_{k_0} J, U, \kappa)$ just with a global shift in momentum of k_0.

Most importantly, the unitary equivalence between the two Lindbladians has consequences for their spectra and eigenvectors. First, the spectrum is the same for both Lindbladians. Additionally, the eigenmodes are also related. Although they are not equal, they only differ by the unitary transformation $\hat{\mathcal{U}}_{k_0}$ and obey

$$|r_j^{k=k_0}\rangle\!\rangle = \hat{\mathcal{U}}_{k_0} |r_j^{k=0}\rangle\!\rangle, \quad |l_j^{k=k_0}\rangle\!\rangle = \hat{\mathcal{U}}_{k_0} |l_j^{k=0}\rangle\!\rangle \, , \tag{4.62}$$

where $|r_j^k\rangle\!\rangle$ ($|l_j^k\rangle\!\rangle$) denote the right (left) eigenmode to eigenvalue λ_j for the Lindbladian with characteristic momentum k. Intuitively, this relation makes sense, since all momenta are shifted by k_0, which also applies to the eigenmodes.

Consequently, also the steady state and its expectation values change. For instance, the OBDMs of steady states at different characteristic momenta can be related with each other by using the unitary connection given in Eq. (4.62). We find

$$\gamma^{k_0}_{lm} = \mathrm{Tr}\big(\hat{r}_1^{k_0}\hat{b}_m^\dagger\hat{b}_l\big) = \mathrm{Tr}\big(\hat{U}_{k_0}\hat{r}_1^0\hat{U}_{k_0}^\dagger\,\hat{b}_m^\dagger\hat{b}_l\big) = e^{ik_0(m-l)}\mathrm{Tr}\big(\hat{r}_1^0\hat{b}_m^\dagger\hat{b}_l\big)\,, \tag{4.63}$$

where we used the representation of the vectorized unitary on density matrices in the second step and in the third step the cyclicity of the trace, as well as Eq. (4.57). This modulation by a site-dependent prefactor is a bit unintuitive. So, to better interpret the result, we may change into the Fourier basis, which is done by inserting the momentum space representation of the creation and annihilation operators introduced in Sec. 4.1 and find

$$\gamma^{k_0}_{k,k'} = \sum_{m,l}\mathrm{e}^{\mathrm{i}(mk'-lk)}\mathrm{Tr}\big(\hat{r}_1^{k_0}\hat{b}_m^\dagger\hat{b}_l\big) = \sum_{m,l}\mathrm{e}^{\mathrm{i}(mk'-lk)}e^{ik_0(m-l)}\gamma^0_{lm} = \gamma^0_{k+k_0,k'+k_0}\,. \tag{4.64}$$

This shows that, also on the level of the OBDM, changing k_0 can be interpreted as a global shift in the momentum space by k_0. Most importantly, Eq. (4.64) constitutes a unitary transformation on the matrix and reveals that the condensate density of both steady states is the same, and the leading eigenvector is also just shifted by k_0. If we find a certain scaling behavior of the condensate density for $k_0 = 0$, we can directly infer that the same scaling holds true for finite k_0, and that the condensation happens at momentum k_0. The only subtlety in Eq. (4.61) is the change in the sign of the hopping amplitude, $J \to \sigma_{k_0}J$. Consequently, the condensate density still depends on whether $|k_0| < \pi/2$ or $|k_0| \geq \pi/2$, and the regimes are connected via changing the sign of the hopping amplitude.

However, it is possible to shift the sign into the onsite interaction term. We define another unitary, which leaves the dissipator unchanged while changing the overall sign of the Hamiltonian by exploiting the structure of the commutator in the Lindbladian Eq. (2.2), which changes sign upon swapping the inputs. This amounts to swapping the physical and auxiliary lattice in the vectorized language. To avoid confusion in the following, we will denote bosonic operators on the physical sublattice by $\hat{b}^\dagger$ ($\hat{b}$), and on the auxiliary sublattice by $\hat{a}^\dagger$ ($\hat{a}$). We define a unitary $\hat{\mathcal{S}}$ acting as

$$\hat{\mathcal{S}}\hat{a}_j\,\hat{\mathcal{S}}^\dagger = \hat{b}_j\ , \quad \hat{\mathcal{S}}\hat{b}_j\,\hat{\mathcal{S}}^\dagger = \hat{a}_j\ . \tag{4.65}$$

Denoting by $\hat{\mathcal{H}}_0(J,U)$ and $\hat{\mathcal{D}}_0(\kappa)$ the Hamiltonian and dissipative part of the Lindbladian $\hat{\mathcal{L}}_0(J,U,\kappa)$ (see Eq. (2.8)), respectively, we find the transformation behavior

$$\hat{\mathcal{S}}\hat{\mathcal{H}}_0(J,U)\hat{\mathcal{S}}^\dagger = -\hat{\mathcal{H}}_0(J,U) = \hat{\mathcal{H}}_0(-J,-U)\ , \tag{4.66}$$

where we used the relation $\hat{H}_0^T(J,U) = \hat{H}_0(J,U)$, since the Hamiltonian is real for $k_0 = 0$. The jump operators obey $\hat{L}_j^0 = \big[L_j^0\big]^*$, where $*$ denotes a complex conjugation, implying

$$\hat{\mathcal{S}}\hat{\mathcal{D}}_0(\kappa)\hat{\mathcal{S}}^\dagger = \hat{\mathcal{D}}_0(\kappa)\ . \tag{4.67}$$

This finally yields unitary equivalence between the Lindbladians

$$\hat{\mathcal{S}}\big(\hat{\mathcal{H}}_0(J,U) + \hat{\mathcal{D}}_0(\kappa)\big)\hat{\mathcal{S}}^\dagger = \big(\hat{\mathcal{H}}_0(-J,-U) + \hat{\mathcal{D}}_0(\kappa)\big)\ . \tag{4.68}$$

If we now combine with the momentum-shift transformation Eq. (4.61) we can relate the Lindbladian with momentum $|k_0| \geq \pi/2$ with the one at $k_0 = 0$ without changing the sign of J,

$$\hat{\mathcal{U}}_{k_0}\hat{\mathcal{S}}\hat{\mathcal{L}}_0(J,-U,\kappa)\hat{\mathcal{S}}^\dagger\hat{\mathcal{U}}_{k_0}^\dagger = \hat{\mathcal{L}}_{k_0}(J,U,\kappa)\ . \tag{4.69}$$

Consequently, the Lindbladians at positive $U > 0$ and $|k_0| \geq \pi/2$ are unitarily connected to the ones with $U < 0$ and $|k_0| < \pi/2$.

Importantly, the uniqueness of the steady state in the zero-momentum case [17] carries over to the general k_0 case, since the steady states are unitarily connected to one another.

4.5 Fast preparation via the quantum Mpemba effect

As we established in Section 4.3 the dissipative gap Δ closes superlinearly with system size, leading to a superlinear increase in the preparation times $t \sim 1/\Delta$. This constitutes a major problem, especially if BECs on large-scale optical lattices of about 10^3 [134] need to be prepared.

A possible way to curtail these increasing preparation times is the quantum Mpemba effect, which we already discussed in Sec. 2.4. Initializing the ultracold atoms in the optical lattice with a carefully chosen microscopic configuration, the dynamics will avoid the slow dissipative channels and converge to the steady state exponentially quicker, compared to an initialization with a random state [18]. Unfortunately, finding such initial states requires an orthogonalization to the slowest decaying left eigenmode $\hat{l}_2$. Although CLIK-MPS allows for the calculation of this eigenmode, devising ways to analytically determine the quickly converging initial states proves as more efficient.

This section is organized as follows: After giving a short introduction to the main ideas of our strategy to find admissible states in Sec. 4.5.1, we analytically investigate the symmetry properties of the slowest decaying mode in Sec. 4.5.2. The arguments rely on perturbation theory, and we numerically verify and back them for large scale systems using CLIK-MPS. In Sec. 4.5.3 we numerically check if the quantum Mpemba effect emerges in all parameter regimes both for small and large system sizes with CLIK-MPS. In Sec. 4.5.4 we briefly discuss the applicability of the arguments in the general characteristic momentum case. Lastly, in Sec. 4.5.5 we numerically calculate the speedups which can be expected when initializing with optimized states, and we discuss the experimental realization of the quickly-converging states.

4.5.1 Introduction and general idea

Before we dive into the arguments for the emergence of the quantum Mpemba effect, we need to analyze the symmetries of the dissipative Bose-Hubbard model Eq. (3.1) more thoroughly. We already identified a $U(1)$-symmetry of the system in Sec. 4.1, which also gives rise to a particle number conservation. Interestingly, there is another discrete symmetry, which is mediated by a unitary $\hat{U}_{\text{inv}}$ with action

$$\hat{U}_{\text{inv}} \hat{b}_j^\dagger \hat{U}_{\text{inv}}^\dagger = \hat{b}_{L+1-j}^\dagger \; . \tag{4.70}$$

It can be interpreted as an inversion around the middle site(s), which is why we term it *inversion symmetry.* The Hamiltonian (c.f. Eq. (4.1)) commutes with the unitary, $\big[\hat{U}_{\text{inv}}, \hat{H}\big] = 0$, while the jump operators transform as

$$\begin{aligned}\hat{U}_{\text{inv}} \hat{L}_j \hat{U}_{\text{inv}}^\dagger &= \hat{U}_{\text{inv}} \sqrt{\kappa} \big(\hat{b}_{j+1}^\dagger + \hat{b}_j^\dagger\big) \hat{U}_{\text{inv}}^\dagger \hat{U}_{\text{inv}} \big(\hat{b}_{j+1} - \hat{b}_j\big) \hat{U}_{\text{inv}}^\dagger \\ &= \sqrt{\kappa} \big(\hat{b}_{L-j}^\dagger + \hat{b}_{L-j+1}^\dagger\big) \big(\hat{b}_{L-j} - \hat{b}_{L-j+1}\big) = -\hat{L}_{L-j} \; ,\end{aligned} \tag{4.71}$$

implying that the Lindbladian commutes with the vectorized unitary $\hat{\mathcal{U}}_{\text{inv}} = \hat{U}_{\text{inv}} \otimes \hat{U}_{\text{inv}}^*$, that is $\big[\hat{\mathcal{U}}_{\text{inv}}, \hat{\mathcal{L}}\big] = 0$. However, from Sec. 2.3 we conclude that the inversion symmetry is a weak symmetry, and the generator is not conserved. Nevertheless, as we discussed in Sec. 2.3, the Lindbladian attains a block diagonal structure, and since we deal with a $\mathbb{Z}_2$-symmetry, the Lindbladian splits up into two blocks. One block contains all states that transform without changing their sign under inversion, while the other contains states picking up a minus sign

$$\hat{\mathcal{U}}_{\text{inv}} |\rho_{\text{even}}\rangle\!\rangle = |\rho_{\text{even}}\rangle\!\rangle \quad (\text{evenly transf.})\, ; \quad \hat{\mathcal{U}}_{\text{inv}} |\rho_{\text{odd}}\rangle\!\rangle = -|\rho_{\text{odd}}\rangle\!\rangle \quad (\text{oddly transf.}) \; . \tag{4.72}$$

This classification also holds for the eigenvectors of the Lindbladian, and we have evenly and oddly transforming eigenvectors. Ideally we would like to know the transformation behavior of each eigenvalue (i.e. of the corresponding eigenvector). A special interest lies on the slowest decaying mode, as it governs the long time behavior of the system.

In the following sections we will explore exactly that. The analysis for the slowest decaying mode will enable us to find special states that converge exponentially faster to the steady state than general states.

Our arguments rely on the idea, that if a mode lies in one of the two subspaces, it is orthogonal to all states lying in the other one, since evenly transforming states are orthogonal to oddly transforming ones. Therefore, if we show that the slowest decaying mode transforms oddly, we directly know that an evenly initialized state will converge exponentially faster. In Fig. 16a we show the low-lying spectrum of the Lindbladian schematically. Here, the color indicates which eigenvector transforms evenly (lilac) or oddly (blue). In Fig. 16b we schematically depict two different pure product state initializations. $|\rho_{\mathrm{random}}\rangle$, where the bosons are distributed randomly over the lattice results in the state $\hat{\rho} = |\rho_{\mathrm{random}}\rangle\langle\rho_{\mathrm{random}}|$ and has no special transformation behavior. The second state $|\rho_{\mathrm{sym}}\rangle$ on the other hand transforms evenly when inverting the lattice, which mans that it is orthogonal to all modes that transform oddly under inversion.

To find the transformation behavior of the steady state (which is equal to the normalized right eigenvector $|r_1\rangle\rangle$), we can use the property that it is a physical state and thus is traceful. Using the insights from Section 2.3, we conclude that the steady state lies in the $\hat{\mathcal{Q}} = 0$ sector, where $\hat{\mathcal{Q}}$ denotes the generator of $\hat{\mathcal{U}}_{\mathrm{inv}}$. This directly implies that the steady state is evenly transforming. Note that this transformation behavior is to be understood with regards to the vectorized unitary, which is different compared to the unitary on the physical lattice only. Indeed, consider two physical states $|\psi_{\mathrm{sym}}\rangle$ and $|\psi_{\mathrm{antisym}}\rangle$, where the former transforms evenly and the latter oddly with respect to $\hat{U}_{\mathrm{inv}}$. Building vectorized states by taking tensor products, we may first build the two density matrices $|\rho_1\rangle\rangle = |\psi_{\mathrm{sym}}\rangle \otimes |\psi_{\mathrm{sym}}\rangle$ and $|\rho_2\rangle\rangle = |\psi_{\mathrm{antisym}}\rangle \otimes |\psi_{\mathrm{antisym}}\rangle$. However, *both* states transform evenly under the vectorized inversion $\hat{\mathcal{U}}_{\mathrm{inv}}$. This is owed to the fact that the vectorized generator $\hat{\mathcal{Q}}$ is connected to the physical generator $\hat{Q}$ by $\hat{\mathcal{Q}} = \hat{Q} \otimes \hat{\mathbb{1}} - \hat{\mathbb{1}} \otimes \hat{Q}$. Therefore, even if the physical states on both sublattices transform oddly (i.e. $\hat{Q} = 1$), the resulting vectorized state transforms evenly. An oddly transforming vectorized state is built by taking two differently transforming states into the tensor product, like $|\rho_3\rangle\rangle = |\psi_{\mathrm{sym}}\rangle \otimes |\psi_{\mathrm{antisym}}\rangle$. The transformation behavior multiplies under taking the tensor product of two states (c.f. Eq. (4.80)). In the following we refer to the transformation behavior as the behavior on the vectorized lattice, if not stated otherwise.

4.5.2 Approach via perturbation theory

In this section, we finally face the challenge of making the arguments from Sec. 4.5.1 rigorous and show that the slowest decaying eigenvectors transform oddly. This proves to be difficult, as the Lindbladian is not integrable, preventing the direct consideration of the full Lindbladian. Instead, we first consider the Hamiltonian part alone without dissipation. In this case we can show which eigenvalues correspond to which transformation behavior. However, the dynamics is purely unitary and there is no steady state in the common sense. In a second step, the dissipation is slowly turned on, and perturbation theory is utilized to analyze the movement of the different eigenvectors. With this analysis, we infer the eigenspace of the Hamiltonian part, where the slowest decaying mode originated from. This basic idea is also schematically depicted in Figure 17.

It is not straightforwardly obvious why perturbation theory can be used in this setting, leading to efforts to back up the perturbation theory numerically not only for system sizes within reach for ED, but also for larger system sizes, where a treatment using CLIK-MPS is needed. We also restrict the analysis to the zero momentum case, as we already established the unitary

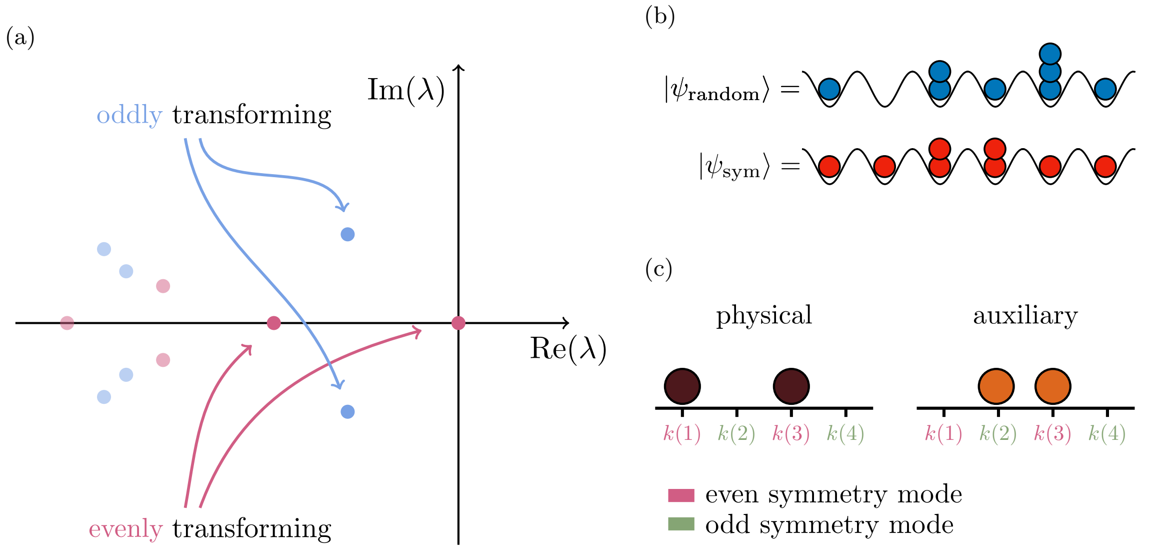

Figure 16: Panel a): Schematic depiction of the Lindbladian spectrum, with indication of the transformation behavior under $\hat{\mathcal{U}}_{\text{inv}}$ by color. The steady state admits $\lambda_1 = 0$ and transforms evenly (lilac), the slowest decaying mode comes as a complex pair λ_2, λ_2^* and transforms oddly (blue). Panel b): A random (blue) and symmetric (red) pure product state on the real lattice. The random state has no fixed transformation behavior under $\hat{\mathcal{U}}_{\text{inv}}$. The symmetric state transforms evenly under the unitary $\hat{U}_{\text{inv}}$ on the physical lattice, and hence the corresponding density matrix $|\psi_{\text{sym}}\rangle\langle\psi_{\text{sym}}|$ also transforms evenly under $\hat{\mathcal{U}}_{\text{inv}}$. Panel c): A state in the eigenspace of $\hat{\mathcal{H}}$ to eigenvalue $-\mathrm{i}(E_{k(1)} - E_{k(2)})$ for an even ($L = 4$) number of sites L. The state transforms oddly under $\hat{\mathcal{U}}_{\text{inv}}$, easily seen by the transformation behavior (under $\hat{U}_{\text{inv}}$) of every individual particle (green or pink) and Eq. (4.80). Panel b) and c) have been adapted from [1].

connections between the Lindbladians with different momenta in Sec. 4.4.

Consider the Bose-Hubbard Hamiltonian at $k_0 = 0$

$$\hat{H} = -J \sum_{j=1}^{L-1} \left(\hat{b}_{j+1}^\dagger \hat{b}_j + \text{h.c.} \right) + \frac{U}{2} \sum_{j=1}^{L} \left[\hat{b}_j^\dagger\right]^2 \left[\hat{b}_j\right]^2 , \tag{4.73}$$

with OBCs as analyzed before. In the case of vanishing onsite interaction $U = 0$, the Hamiltonian is quadratic and can be diagonalized by introducing new creation and annihilation operators

$$\hat{d}_k^\dagger = \sum_{j=1}^{L} \sin(kj)\, \hat{b}_j^\dagger , \quad k(m) = \frac{\pi}{L+1} m,\ m \in \{1, \dots, L\} . \tag{4.74}$$

The Hamiltonian then attains the diagonal form

$$\hat{H} = \sum_k E_k \hat{d}_k^\dagger \hat{d}_k, \qquad E_k = -2J \cos(k) , \tag{4.75}$$

and the new creation operators $\hat{d}_k^\dagger$ create particles with energy E_k. Thus, the many-body eigenvectors are constructed by successively adding particles $\hat{d}_k^\dagger$ into the system and can be characterized by a vector $\mathbf{n} = (n_1, n_2, \dots, n_L)$, which describes the occupation of each of the modes $k(m)$, $m = 1, \ldots, L$,

$$|\mathbf{n}\rangle = \prod_{m=1}^{L} \frac{\big(\hat{d}^{\dagger}_{k(m)}\big)^{n_m}}{\sqrt{n_m!}} |0\rangle \ , \tag{4.76}$$

with energy

$$E(\mathbf{n}) = \sum_{m=1}^{L} E_{k(m)} n_m \ . \tag{4.77}$$

Interestingly, the spectrum is symmetric around $k(m) = \pi/2$,

$$E_{k(m)} = -E_{k(L+1-m)} \ . \tag{4.78}$$

Moreover, due to the inversion symmetry, the eigenvectors are inversion symmetric with respect to $\hat{U}_{\text{inv}}$. One can show that the transformation behavior is alternating due to the sine in Eq. (4.74),

$$\hat{U}_{\text{inv}} \hat{d}^{\dagger}_{k(m)} \hat{U}^{\dagger}_{\text{inv}} = (-1)^{m-1} \hat{d}^{\dagger}_{k(m)} \ . \tag{4.79}$$

The transformation behavior of a many-body eigenvector $|\mathbf{n}\rangle$ is directly derived from Eq. (4.79) together with Eq. (4.74)

$$\begin{aligned} \hat{U}_{\text{inv}} |\mathbf{n}\rangle &= \prod_{m=1}^{L} \frac{\big(\hat{U}_{\text{inv}} \hat{d}^{\dagger}_{k(m)} \hat{U}^{\dagger}_{\text{inv}}\big)^{n_m}}{\sqrt{n_m!}} |0\rangle = \prod_{m=1}^{L} (-1)^{n_m(m-1)} \frac{\big(\hat{d}^{\dagger}_{k(m)}\big)^{n_m}}{\sqrt{n_m!}} |0\rangle \\ &= |\mathbf{n}\rangle \prod_{m=1}^{L} (-1)^{n_m(m-1)} . \end{aligned} \tag{4.80}$$

This reduces calculating the transformation behavior of a many-body eigenstate to counting the number of particles in each mode and then multiplying all their individual eigenvalues together.

In order to study the Lindbladian, it is necessary to consider the enlarged, vectorized Hilbert space. We already introduced the general form of the vectorized Lindbladian [24] in Eq. (2.8) and introduced the jump operators in Eq. (4.2). Setting $k_0 = 0$ the jump operators read

$$\hat{L}_j = \sqrt{\kappa}(\hat{b}^{\dagger}_{j+1} + \hat{b}^{\dagger}_{j})(\hat{b}_{j+1} - \hat{b}_{j}) \ . \tag{4.81}$$

In the following, we focus on the unitary part of the Lindbladian $\hat{\mathcal{H}}$ in Eq. (2.8), whose eigenvectors are tightly connected to the many-body eigenvectors of the Hamiltonian

$$\hat{\mathcal{H}} \, |\mathbf{n}\rangle \otimes |\tilde{\mathbf{n}}\rangle = -\mathrm{i}\big(E(\mathbf{n}) - E(\tilde{\mathbf{n}})\big) \, |\mathbf{n}\rangle \otimes |\tilde{\mathbf{n}}\rangle \ , \tag{4.82}$$

where $\mathbf{n}$ and $\tilde{\mathbf{n}}$ denote the configuration on physical and auxiliary lattice. This notation is utilized throughout the section if not stated otherwise. For clarity, we will label the quantum numbers on the physical lattice k_{p} by $\text{p} = 1, \ldots, L$ and on the auxiliary k_{a} by $\text{a} = 1, \ldots, L$. Due to the strong $U(1)$-symmetry admitting the particle number conservation, the Lindbladian is block diagonal, each block representing a fixed particle number. Since we are only interested in the dynamics of an initial state with fixed particle number N, we can directly restrict the analysis to eigenstates lying in this subsector. These eigenvectors obey $\|\mathbf{n}\|_1 = \|\tilde{\mathbf{n}}\|_1 = N$. An example of an eigenstate of $\hat{\mathcal{H}}$ with two particles on a four site lattice is depicted in Fig. 16c. The state is directly written in the particle number basis and it describes a state in the two particle sector, which is easily seen from the two particles on the physical (blue) and auxiliary (orange) sublattices. The transformation behavior under $\hat{\mathcal{U}}_{\text{inv}}$ can be directly inferred from the number of

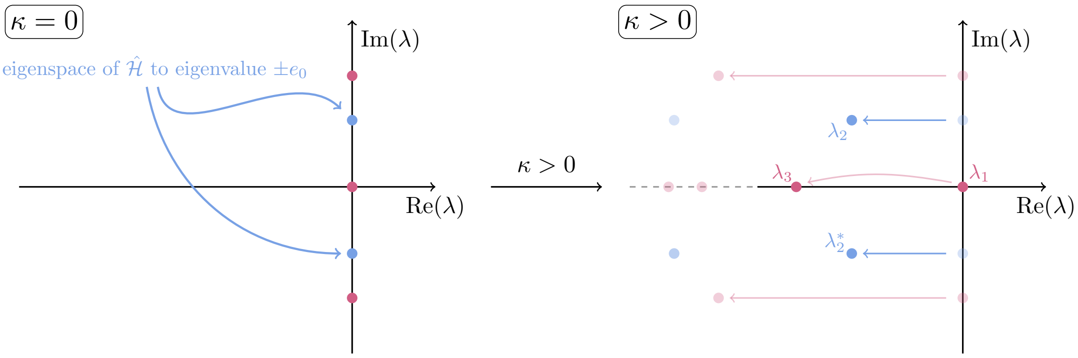

Figure 17: Schematic depiction of the arguments for the transformation behavior of the slowest decaying mode $|l_2\rangle\rangle$. First, we only consider the vectorized Hamiltonian part $\hat{\mathcal{H}}$ (c.f. Eq. (2.8)) of the Lindbladian (left panel), which admits a highly degenerate spectrum. Theorem 1 implies that the subspaces associated to the eigenvalue $\pm \mathrm{i} e_0 = \pm \mathrm{i}(E_{k(1)} - E_{k(2)})$ only contain oddly transforming vectors under $\hat{\mathcal{U}}_{\text{inv}}$. In a next step, we turn on the dissipation and trace the movement of the eigenmodes. This way we can identify the transformation behavior of the eigenvectors of the full Lindbladian (theorem 5). Using extensive numerical analysis, we show that the slowest decaying eigenvectors originate out of the eigenspace to eigenvector e_0.

particles and the occupied modes according to Eq. (4.80). In total, three particles sit on evenly transforming modes, while one sits on an oddly transforming mode. Multiplying together yields $(+1)(+1)(+1)(-1) = -1$, showing that the resulting state transforms oddly under $\hat{\mathcal{U}}_{\text{inv}}$.

As stated at the beginning of this section we want to find out the transformation behavior of the eigenvectors associated to some eigenvalues. In the present case, this is difficult, since the spectrum of $\hat{\mathcal{H}}$ is highly degenerate. Nevertheless we can prove theorems about certain eigenspaces of $\hat{\mathcal{H}}$.

1. Theorem: Let $|\mathbf{n}\rangle \otimes |\tilde{\mathbf{n}}\rangle$ be an eigenstate of $\hat{\mathcal{H}}$ to eigenvalue $\pm \mathrm{i}(E_{k(1)} - E_{k(2)})$. Then it transforms oddly under inversion, that is $\hat{\mathcal{U}}_{\text{inv}} |\mathbf{n}\rangle \otimes |\tilde{\mathbf{n}}\rangle = - |\mathbf{n}\rangle \otimes |\tilde{\mathbf{n}}\rangle$.

At this stage, it is not clear why this eigenspace is so important, but the perturbation theory will reveal that the slowest decaying modes originates out of this subspace.

Proof of 1: We may take a general ket in the subspace with eigenvalue $\pm \mathrm{i}(E_{k(1)} - E_{k(2)})$, characterized by $\mathbf{n}$ and $\tilde{\mathbf{n}}$. This eigenvalue can only be realized if all but two particles contribute a sum of 0 to the eigenvalue, while the remaining two have exactly the eigenvalue of interest (see Eq. (4.82)). As a consequence, we can reduce to the case with two physical and two auxiliary particles, but additionally we need to prove, that states with eigenvalue 0 transform evenly (proven in theorem 2). So let's prove the two particle case.

For a state with two physical particles (that means two on physical and two on the auxiliary sublattice), two particles need to create the energy difference. Consequently, the possible fillings are: $k_{\mathrm{p}}(1)$ and $k_{\mathrm{p}}(L-1)$; $k_{\mathrm{a}}(L)$ and $k_{\mathrm{a}}(2)$; $k_{\mathrm{p}}(1)$ and $k_{\mathrm{a}}(2)$; $k_{\mathrm{p}}(L-1)$ and $k_{\mathrm{a}}(L)$ (the last two stem from the special symmetry of the dispersion relation). In the case of even L, the first two transform evenly, the last two oddly. For odd L, all transform oddly. The two remaining particles combined need to have energy 0. If this is achieved by one particle on the physical and one on the auxiliary lattice, the two particles need to occupy $k_{\mathrm{a}}(m)$ and $k_{\mathrm{p}}(m)$, and thus transform evenly. If they both sit in one lattice, they need to occupy $k_{\mathrm{p/a}}(m)$ and $k_{\mathrm{p/a}}(L+1-m)$ and together transform oddly in the case of even L, and evenly for odd L. In total, all possibilities transform oddly according to Eq. (4.80).

The proof therefore relies on the following theorem.

2. Theorem: Let $|\mathbf{n}\rangle \otimes |\tilde{\mathbf{n}}\rangle$ be an eigenstate of $\hat{\mathcal{H}}$ to eigenvalue 0. Then it transforms evenly under inversion, that is, $\hat{\mathcal{U}}_{\mathrm{inv}} |\mathbf{n}\rangle \otimes |\tilde{\mathbf{n}}\rangle = |\mathbf{n}\rangle \otimes |\tilde{\mathbf{n}}\rangle$.

Proof of 2: The main difficulty in proving theorem 2 lies in the particle number of $|\mathbf{n}\rangle \otimes |\tilde{\mathbf{n}}\rangle$ being arbitrary. Hence, we first reduce the general particle number case to the case with one or two particles, which in the last step can be checked by counting all possible fillings as in the proof of theorem 1.

To reduce the general case, we first rewrite the eigenvalue of a state as

$$E(\mathbf{n}) - E(\tilde{\mathbf{n}}) = \sum_{m=1}^{\lfloor \frac{L}{2} \rfloor} \big(n_m - \tilde{n}_m - n_{L+1-m} + \tilde{n}_{L+1-m}\big) E_{k(m)} \,, \tag{4.83}$$

which is possible due to Eq. (4.78). This rewriting is necessary, since now all contributing energies $E_{k(m)}$ are distinct and incommensurable. Consequently, the left-hand side only vanishes if

$$n_m - \tilde{n}_m - n_{L+1-m} + \tilde{n}_{L+1-m} = 0, \quad \forall\, m \leq \left\lfloor \frac{L}{2} \right\rfloor . \tag{4.84}$$

In case of odd L care must be taken, as $n_{L+1/2} - \tilde{n}_{L+1/2}$ might be nonzero, owing to the fact that $E_{L+1/2} = 0$. From now on, the k-sites m and $L+1-m$ on the physical and auxiliary lattice together will be called m-th *sector*. In each of the sectors, the constraint Eq. (4.84) must be fulfilled (with the exception of the ${}^{L+1}/_2$-sector, which we will refer to as *zero-sector*).
This also entails an *even* number of particles in each sector. Consequently, there always exist two particles that contribute a combined eigenvalue of 0. Such particles may be found by taking a sector m which contains particles, and since the constraint Eq. (4.84) translates to $n_m + \tilde{n}_{L+1-m} = \tilde{n}_m + n_{L+1-m}$, we can take out two particles whose energy adds up to 0. The possibilities for these particles are one on the physical lattice and one on the auxiliary lattice, or both are on the same sublattice. In the latter case, there is some other sector which contains two particles on the other sublattice that have a combined eigenvalue of zero due to the total particle number being equal on both sublattices. Taking away these 2 or 4 particles, we end up with a state with $N-1$ or $N-2$ physical particles that has the same eigenvalue. The 2 or 4 particles taken out also have combined eigenvalue 0, and we will show that they transform evenly. Doing this successively until no particles are left, we indeed reduced to the two and one particle case, which we study now.

We will make a case distinction between even and odd number of sites L, due to the subtlety of the zero-sector. Starting with an *even* number of sites and one (physical) particle, to fulfill the subspace constraint Eq. (4.84), the physical and the auxiliary particle need to sit in the same sector, denoted by m. It reads

$$n_m + \tilde{n}_{L+1-m} = n_{L+1-m} + \tilde{n}_m = 1 \,, \tag{4.85}$$

giving the possibilities $n_m = \tilde{n}_m = 1$ or $n_{L+1-m} = \tilde{n}_{L+1-m} = 1$, and both possible configurations transform evenly.
For two physical particles, there are more possible fillings. Either all 4 particles (2 physical and

2 auxiliary) are loaded in one sector, or two sectors are filled with two particles each. In the former case, the subspace constraint enforces

$$n_m + \tilde{n}_{L+1-m} = n_{L+1-m} + \tilde{n}_m = 2\,, \tag{4.86}$$

for one sector m, which gives rise to the fillings $n_m = \tilde{n}_m = 2$, $n_{L+1-m}+\tilde{n}_{L+1-m} = 2$, $n_m = \tilde{n}_m = n_{L+1-m} = \tilde{n}_{L+1-m} = 1$, all transforming evenly. Note that all other possible configurations satisfying the constraint are ruled out due to the fact that physical and auxiliary sublattice are equally populated.

Next, there is also the possibility of just two particles sitting in the same sector, for which there are two subcases: Either, in each of the filled sectors m and r, one physical and one auxiliary particle is placed, or two physical particles are placed in one sector and two auxiliary particles in the other. The first case is just two times the one particle case discussed above, and as a consequence, it gives rise to even states. The second case however is different; labeling the occupied sectors by m and r, the constraint translates to

$$n_m = n_{L+1-m} = 1, \qquad \tilde{n}_r = \tilde{n}_{L+1-r} = 1\,, \tag{4.87}$$

which also transforms evenly. This concludes the discussion in the case of an even number of sites.

For odd L, the case distinction above stays valid (although the individual arguments, why in each case the state transforms evenly, change). However, we have to take into account the zero sector, in which particles can reside without fulfilling the constraint Eq. (4.84). But we know that an even number of particles is in the total vectorized lattice and in each of the normal sectors, an even number of particles has to be located. Thus, simple counting shows that an even number of particles has to sit in the zero sector as well. Since we only need to deal with one and two physical particles, we can extract the cases where the zero-sector is populated. The case of one physical particle is straightforward, since both vectorized particles need be in the zero-sector, combining to an even transformation. For two physical particles, there are two cases, either four or two particles are in the zero-sector, while in the latter case the remaining two particles need to obey the fillings discussed in the one-particle case above. So, as every single particle in the zero-sector has odd symmetry (but an even number of them is in there), we only get evenly transforming states.

This concludes the discussion of the case $\kappa = 0$, where we established that a certain eigenspace of $\hat{\mathcal{H}}$ only consists of oddly transforming states. We use this in the following theorem.

5. Main theorem: Consider the Lindbladian Eq. (3.1) with $k_0 = 0$. All left eigenmodes, which, when adiabatically switching on the dissipation, stem from the eigenspace of $\hat{\mathcal{H}}$ to eigenvalue $\mathrm{i}e_0 = \mathrm{i}\big(E_{k(1)} - E_{k(2)}\big)$, will have zero overlap with evenly transforming states.

Proof of 5: Let $\hat{l}_m$ be an eigenmode stemming from the eigenspace $\mathrm{i}(E_{k(1)} - E_{k(2)})$. That is, there is a $\hat{l}_m^{\text{appr.}}$ in this subspace which agrees with $\hat{l}_m$ in the case of vanishing dissipation $\kappa \to 0^+$. Such an approximate mode is found by (degenerate) perturbation theory and we can therefore safely say that $\mathrm{Tr}\big(\hat{l}_m^\dagger \hat{l}_m^{\text{appr.}}\big) \neq 0$ also for strong dissipation (see Fig. 18). However, since the approximate mode lives in a space spanned by only antisymmetric states according to theorem 1, $\hat{l}_m$ has an antisymmetric component. Since the Lindbladian is inversion symmetric according to Sec. 4.5.1 the left eigenmodes can be chosen as eigenvectors of $\hat{\mathcal{U}}_{\text{inv}}$. We conclude, that $\hat{l}_k$ has to be antisymmetric and thus has *vanishing overlap with symmetric states.*

Note that the above arguments are readily generalized to eigenmodes stemming from the eigenspace $-\mathrm{i}e_0$ by switching the auxiliary and physical lattice.

Unfortunately, theorem 5 does not contain any information about the eigenvalues associated to the eigenvectors stemming out of the considered subspace. This is a major problem, as we do not know if the slowest decaying mode is such an eigenmode, which is important for our analysis. A possible route to understand the behavior of the eigenvalues would be to employ first order perturbation theory and describe the dissipation as a small perturbation. However, since the eigenvalues of $\hat{\mathcal{H}}$ are strongly degenerate, perturbation theory only reduces the task to solving the general eigenvalue problem of $\hat{\mathcal{L}}$ in each eigenspace of $\hat{\mathcal{H}}$. The dimension of these subspaces is arbitrarily large for increasing particle number and system size, hindering the efficient analysis. Additionally it is not immediately clear why perturbation theory should work in this setting, as the dissipation changes the real part of the eigenvalues, which in the non-dissipative setting is zero, rendering the dissipation not a small perturbation. All of these considerations and problems prove analytic treatment difficult, and we instead perform extensive numerical analysis to pin the transformation behavior and the origin of the slowest decaying mode. In the following, we will investigate a wide parameter range, showing that the slowest decaying mode stems from the eigenspace in question (see Sec. 4.5.3), and theorem 5 is applicable.

Additionally, we need to treat the case of finite U. Similar to considering finite κ, we can incorporate the onsite interaction by slowly turning it on and treating it perturbatively. This is possible due to the finite system-sizes, where the sharp phase transition between $U = 0$ and $U \neq 0$ (seen in the TD limit, c.f. Sec. 4.2) is washed out and everything is continuous. In the analysis, we therefore slowly increase the onsite interaction similar to κ according to $U = \mathcal{O}(\kappa)$, and the prefactor dictates the target ratio between onsite interaction and dissipation, as shown in Figure 18.

Numerically investigating the origin of the slowest decaying mode requires the knowledge of the low lying spectrum, which we can access through ED methods as well as our new CLIK-MPS framework. We then track the behavior of the eigenvalue associated to the slowest decaying mode when lowering the dissipation $\kappa \to 0^+$.

There are two signatures that tell whether the slowest decaying mode stems from the eigenspace in question. If we denote the eigenvectors of $\hat{\mathcal{H}}$ to eigenvalue e_0 by $\{|e_0, p\rangle\rangle\}_p$, where p numbers the multiplicity, we can check how strong the eigenvector $|l_2(\kappa)\rangle\rangle$ overlaps with the eigenspace. In the following, we will write the dependence on the dissipation strength κ explicitly in eigenvectors and eigenvalues whenever it is of importance. Constructing the projector onto the respective eigenspace $\hat{\Pi}_{e_0} = \sum_p |e_0, p\rangle\rangle\langle\langle e_0, p|$, and projecting the slow decaying eigenvector onto this subspace, the weight outside of the eigenspace is quantified by

$$\Delta_{\mathrm{out}}(\kappa) = 1 - \sum_p \left|\langle\langle e_0, p|l_2(\kappa)\rangle\rangle\right|^2 . \tag{4.88}$$

There exists a normalized vector $|l_2^{\mathrm{appr.}}\rangle\rangle = \sum_l c_l |e_0, l\rangle\rangle$ with weights c_l such that $\Delta_{\mathrm{out}} = 1 - |\langle\langle l_2^{\mathrm{appr.}}|l_2\rangle\rangle|^2$. The state $|l_2^{\mathrm{appr.}}\rangle\rangle$ is the best approximation in the subspace in the sense that it maximizes the overlap with $|l_2\rangle\rangle$. A hard proof that the state $|l_2\rangle\rangle$ stems from the e_0-eigenspace is thus the limit behavior

$$\lim_{\kappa \to 0^+} \Delta_{\mathrm{out}}(\kappa) = 0 . \tag{4.89}$$

Unfortunately this criterion is quite difficult to track for large systems, since not only $|l_2\rangle\rangle$ needs to be known, but also a full basis of the (potentially very large) subspace to eigenvalue e_0. Another handier criterion is connected to the imaginary part of λ_2. If it stems from the

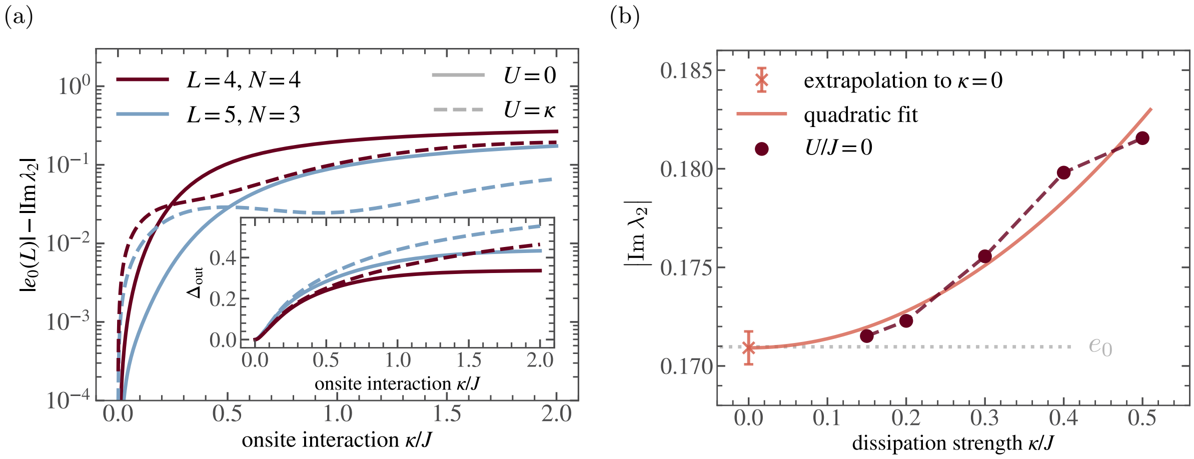

Figure 18: Perturbation theory for the slowest decaying mode. Panel a): Difference of $\mathrm{Im}\,\lambda_2$ to the subspace eigenvalue $e_0(L) = E_{k(2)} - E_{k(1)}$ (see Eqs. (4.75) and (4.82)) as $\kappa \to 0^+$ for small scale systems. Inset: Component Δ_{out} of the eigenmode that lies outside the eigenspace to eigenvalue $\mathrm{i}\, e_0(L)$ (see Eq. (4.88)). Note that slowly increasing the onsite interaction $U = \mathcal{O}(\kappa)$ does not affect the general structure of the overlap, as well as the eigenvalue. The data has been generated using exact diagonalization (ED). Panel b): Analysis for large-scale system with $L = 12$, $N = 8$ using CLIK-MPS. We calculate $\left|\mathrm{Im}\,\lambda_2\right|$ and fit it with the ansatz $a_1 + a_2\kappa^2$, which is motivated from the ED analysis. We recover the value $a_1 = 0.1709 \pm 9 \times 10^{-4}$, which is in agreement with $e_0 = 0.1710$, proving the emergence of the quantum Mpemba effect in this large-scale system. We set $U/J = 0$, chose $\alpha = 0.02$ and the other parameters for CLIK-MPS such that convergence is reached. This includes $\delta t = 0.4$ and $T = 30$, (38) for $\kappa/J = 0.5$, (0.4), $\delta t = 0.8$ and $T = 60$, (64) for $\kappa/J = 0.3$, (0.2), and $\delta t = 1.2$ and $T = 90$ for $\kappa/J = 0.15$. For more details on the numerical implementation see App. A.1. The figures are adapted from [1].

e_0-subspace, we should recover

$$\lim_{\kappa\to 0^+} \left|\mathrm{Im}\,\lambda_2\right| = E_{k(1)} - E_{k(2)} = e_0 \ , \tag{4.90}$$

which seems to be a weaker criterion than Eq. (4.89). However, one can actually show that they are equivalent. As already stated, it is immediately clear that Eq. (4.89) implies Eq. (4.90). To prove the other direction, we start by explicitly separating the κ-dependence from the Lindbladian via $\hat{\mathcal{L}} = \hat{\mathcal{H}} + \kappa\hat{\mathcal{D}}$ (this includes a slight redefinition of $\hat{\mathcal{D}}$ compared to Eq. (2.8)). Now, we can relate the expectation value with the eigenvalue via

$$\left|\lambda_2(\kappa) - E(\kappa)\right| \le \kappa \|\hat{\mathcal{D}}\|_{\mathrm{op}} \ , \tag{4.91}$$

where we introduced new notation for the Hamiltonian expectation value $E(\kappa) = \langle\!\langle l_2(\kappa)|\hat{\mathcal{H}}|l_2(\kappa)\rangle\!\rangle$. In a similar manner, one can show that the variance vanishes

$$\langle\!\langle l_2(\kappa)|\big(\hat{\mathcal{H}} - E(\kappa)\big)^2|l_2(\kappa)\rangle\!\rangle = \mathcal{O}(\kappa) \ , \tag{4.92}$$

by multiplying out and using the eigenvector properties. We can also calculate the variance in the eigenbasis of $\hat{\mathcal{H}}$. We find

$$\begin{aligned}\langle\!\langle l_2(\kappa)|\big(\hat{\mathcal{H}} - E(\kappa)\big)^2|l_2(\kappa)\rangle\!\rangle &= \sum_{E,l} \big(E - E(\kappa)\big)^2 \left|\langle\!\langle E,l|l_2(\kappa)\rangle\!\rangle\right|^2 \\ &= \mathcal{O}(\kappa^2) + \sum_{E\neq e_0,l} \big(E - E(\kappa)\big)^2 \left|\langle\!\langle E,l|l_2(\kappa)\rangle\!\rangle\right|^2 , \end{aligned} \tag{4.93}$$

where (E, l) label the eigenvalues of $\hat{\mathcal{H}}$. Due to the uniform convergence of $E(\kappa)$ to e_0 implied by Eq. (4.91), $\big|E - E(\kappa)\big| > 0.5 \min_{E'\neq e_0} |E' - e_0|$ for all $E \neq e_0$ in the spectrum of $\hat{\mathcal{H}}$ at low enough κ. This makes it possible to upper bound $\Delta_{\text{out}}(\kappa)$ by the above expression, finally showing that

$$\Delta_{\text{out}}(\kappa) \leq \sum_{E\neq e_0,l} \frac{\big(E - E(\kappa)\big)^2}{\big(0.5 \min_{E'\neq e_0} |E' - e_0|\big)^2} \left|\langle\!\langle E,l|l_2(\kappa)\rangle\!\rangle\right|^2 = \mathcal{O}(\kappa) , \tag{4.94}$$

concluding the proof of equivalence. Hence, it suffices to check Eq. (4.90), which directly implies the eigenmode stemming from the e_0-eigenspace.

In Fig. 18 we finally check the criteria Eq. (4.89) and (4.90). In Fig. 18a we study if the behavior Eq. (4.90) is found in the systems with $L = 4, N = 4$ (red) and $L = 5$, $N = 3$ (blue). The solid lines show the behavior for $J = 1$ and $U = 0$, and we observe that the difference of $\operatorname{Im}\lambda_2$ and e_0 vanishes upon lowering κ. We furthermore find that the difference vanishes quadratically, that is $\big|\operatorname{Im}\lambda_2\big| = e_0 + \mathcal{O}(\kappa^2)$, which will be important for the large-scale analysis. Similar behavior is seen when considering a finite U (dashed lines). Here, to recover the subspaces of the Hamiltonian with zero onsite interaction, we turn on U slowly similar to κ as discussed previously, by considering $U = \kappa$. In the inset we check Eq. (4.89) for the same parameters as before, and find the sought after behavior in all cases, as predicted by the equivalence of the criteria.

To really understand if the analytic arguments also apply in large systems, we need numerical tools that reach the low-lying eigenvalues for system sizes not accessible to ED methods. For this task we can directly employ CLIK-MPS, which makes it possible to calculate $\big|\operatorname{Im}\lambda_2\big|$ with high accuracy. In Fig. 18b we show $\big|\operatorname{Im}\lambda_2\big|$ for a system with 12 sites and 8 bosons at $U/J = 0$, depending on the dissipation strength κ/J calculated via CLIK-MPS. Upon lowering the dissipation strength the imaginary part approaches the subspace eigenvalue $e_0 = 0.1710$. To assess if it actually satisfies Eq. (4.90), we can use the knowledge from the ED analysis and extrapolate the finite κ data according to $\big|\operatorname{Im}\lambda_2\big| = a_1 + a_2\kappa^2$. We find $a_1 = 0.1709 \pm 9 \times 10^{-4}$, which is in agreement with e_0. This validates that the Mpemba effect also emerges in this large-scale system, and the analytical results apply.

Although we checked the perturbative arguments for several system parameters, we need to check if they hold for any set of parameters.

4.5.3 Dependence of the Mpemba effect on system parameters

In the last subsection we established an explanation for the emergence of the quantum Mpemba effect for initial states transforming evenly under $\hat{\mathcal{U}}_{\text{inv}}$, partially based on perturbation theory and numerics. However the question remains, if this is the whole story, or if in some parameter regimes a different behavior is seen. For instance, a good candidate for divergent behavior is the high U limit, as we treated U perturbatively in the last section.

To assess the emergence of the Mpemba effect thoroughly, we can perform ED calculations for parameters on a grid of κ/J and U/J. These results are shown in Figure 19 for a system of $L = 6$ and $N = 3$ particles. In Fig. 19a we calculate the modulus of the imaginary part

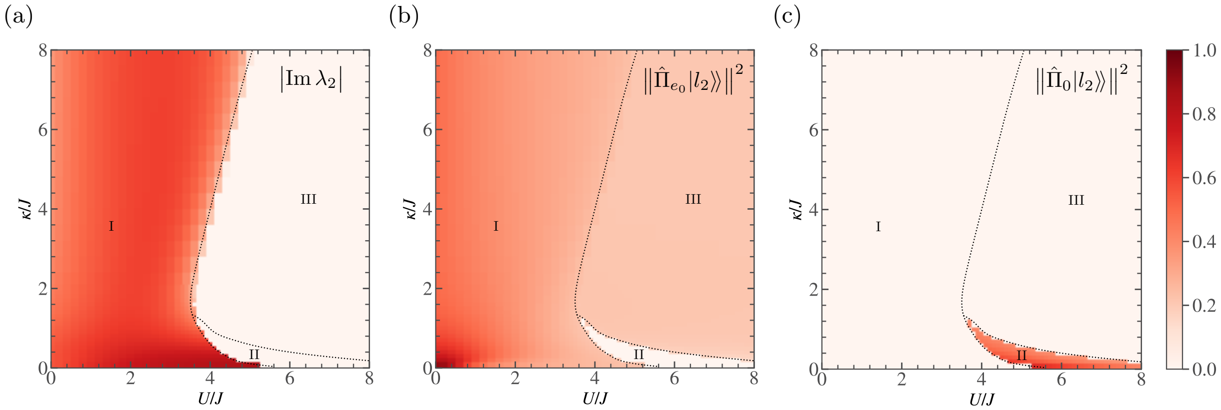

Figure 19: Slowest decaying mode in different parameter regions for the dissipative Bose-Hubbard model Eq. (3.1) depending on the two free parameters κ/J and U/J. Panel a): Modulus of λ_2-s imaginary part. Panel b): Overlap of the slowest decaying left eigenvector with the e_0-eigenspace, which only contains oddly transforming states. Panel c): Overlap of the slowest decaying left eigenvector with the 0-eigenspace, which only contains evenly transforming states. The projector $\hat{\Pi}_0$ is defined similar to $\hat{\Pi}_{e_0}$. The dotted black lines mark parameters at which sudden changes in the observed quantities happen. They separate the different regions I, II and III. The system contains 6 sites and 3 bosons, all calculations where performed using ED at $k_0 = 0$. The figures are adapted from [1].

of the slowest decaying mode, in Fig. 19b the overlap of $|l_2\rangle\rangle$ with the e_0-eigenspace of $\hat{\mathcal{H}}$, and in Fig. 19c the overlap of $|l_2\rangle\rangle$ with the 0-eigenspace of $\hat{\mathcal{H}}$. The overlaps with the respective eigenspaces of $\hat{\mathcal{H}}$ are calculated similarly to Sec. 4.5.2, where we defined the projectors onto the respective subspaces $\hat{\Pi}_E$ for an eigenvalue E. We then look at the norm of the projection onto the respective space as $\left\|\hat{\Pi}_E|l_2\rangle\rangle\right\|^2$.

As predicted by our perturbative analysis, for small $U \ll \max(J,\kappa)$, $\left|\mathrm{Im}\,\lambda_2\right|$ is strictly positive, which leads to a finite overlap with the e_0-eigenspace and thus an odd transformation behavior under $\hat{\mathcal{U}}_{\mathrm{inv}}$. We call parameters with this behavior *region I*, also indicated in the plots. Increasing U/J, $\left|\mathrm{Im}\,\lambda_2\right|$ abruptly jumps to zero, indicating that we expect the slowest decaying mode to transform evenly in this regime.

At small κ/J and intermediate U/J this is exactly the case, as seen when looking at the overlap with the 0-eigenspace in Fig. 19c, where we encounter a jump in the population from zero to a finite value, exactly when $\left|\mathrm{Im}\,\lambda_2\right|$ vanishes. This region is termed *region II.* Contrary to expectation, at higher U/J or κ/J the overlap with the 0-eigenspace jumps back to zero, although $\left|\mathrm{Im}\,\lambda_2\right|$ is still zero. In this region, termed *region III*, the overlap with the e_0-eigenspace is again finite, indicating an odd transformation behavior. In summary, there are the following three spectral regions, which are all distinguished through jumps in some observable.

- Region I: *Finite* $\left|\mathrm{Im}\,\lambda_2\right|$, $|l_2\rangle\rangle$ stemming out of the e_0-eigenspace, implying *odd* transformation behavior. Admitting Mpemba speedups and perturbative description.

- Region II: *Zero* $\left|\mathrm{Im}\,\lambda_2\right|$, $|l_2\rangle\rangle$ stemming out of the 0-eigenspace, implying *even* transformation behavior. Admitting no Mpemba speedups.

- Region III: *Zero* $\left|\mathrm{Im}\,\lambda_2\right|$, but $|l_2\rangle\rangle$ does transform *oddly.* Admitting Mpemba speedups but perturbative description is not possible.

These three parameter regions feature fundamentally different behavior. Luckily, in regions I & III the Mpemba effect due to the odd transformation behavior is present, and these phases make out the biggest part of the parameter plane. But still, only for region I the perturbative analysis provided in Sec. 4.5.2 holds, while it does not apply for region III. We think that for the perturbative analysis of region III a different fixed-point is needed, which we assume to be the model at $\kappa = 0$ and $U = \infty$. This fixed-point will be subject to future research.

Since we work on a finite dimensional Hilbert space and the parameter dependence in the Lindbladian is continuous, the spectrum is also continuous, implying that the jumps must originate from level crossings.

Beyond the quantum Mpemba effect, this behavior is reminiscent of a first order phase transition, which is also characterized by jumps in an observable. However, we do not deal with a phase transition in the typical sense, since information about the decaying modes is lost when approaching the infinite time limit. The discontinuous changes in equilibration behavior are only seen at finite times. In our case, we will see discontinuous differences in the time regime $t \sim -1/\mathrm{Re}(\lambda_2)$, where the equilibration behavior is dictated by the slowest decaying mode. Defining the Hermitian and anti-Hermitian component of $\hat{r}_2$ by $\hat{r}_2^h = \frac{1}{2}(\hat{r}_2 + \hat{r}_2^\dagger)$ and $\hat{r}_2^a = \frac{1}{2\mathrm{i}}(\hat{r}_2 - \hat{r}_2^\dagger)$ yields

$$\hat{\rho}(t) - \hat{\rho}_{\mathrm{ss}} = 2\,\mathrm{Re}\big(\mathrm{e}^{\lambda_2 t}\langle\!\langle l_2|\rho\rangle\!\rangle\big)\hat{r}_2^h - 2\,\mathrm{Im}\big(\mathrm{e}^{\lambda_2 t}\langle\!\langle l_2|\rho\rangle\!\rangle\big)\hat{r}_2^a\,, \tag{4.95}$$

and in the following we abbreviate the prefactors by R and I. In case of a smooth parameter transition from region II or III to I, there will be a drastic change in this difference. In the former regions, the eigenvalue is real implying $\hat{r}_2^a = 0$, and a general distance measure will see a monotonic decay according to $\mathrm{e}^{\mathrm{Re}\,\lambda_2\, t}$. On the other hand, in region I we get

$$\|\hat{\rho}(t) - \hat{\rho}_{\mathrm{ss}}\|_2^2 = R^2\|\hat{r}_2^h\|_2^2 + I^2\|\hat{r}_2^a\|_2^2 - 2RI\,\mathrm{Re}\langle\!\langle r_2^h|r_2^a\rangle\!\rangle\,. \tag{4.96}$$

and the last term introduces periodic oscillations, which are clearly visible and constitute a discontinuous change compared to regions II and III. Lastly, if a transition between the regions II and III happens, the equilibration behavior again changes. Although $\rho(t) - \rho_{\mathrm{ss}}$ is monotonically in time, the prefactor is dictated by $\langle\!\langle l_2|\rho\rangle\!\rangle$, which changes drastically, since the slowest decaying mode in both regimes have different transformation behavior. This means that crossing a boundary between regions leads to discontinuous changes in the convergence behavior of a generic initial state. We call this behavior a *in-spectrum phase transition (ISPT)*, which is characterized by changes in the spectrum which are discontinuous and have consequences for the behavior at intermediate times. Note that a similar level crossing was recently observed in a classical Ising model, which was connected to a dynamical phase transition [135].

For the emergence of the quantum Mpemba effect, it is imperative to check if region II expands with increasing lattice size. Otherwise, symmetric states converge quicker only in small systems, which hinders the use in large-scale optical lattices. In larger systems some of the analysis presented in Figure 19 is not possible any more, and we need to work with the quantities accessible through CLIK-MPS. Luckily, the eigenvalue λ_2 needed for Fig. 19a can be calculated with CLIK-MPS. For 19b and 19c, the projection onto an eigenspace is difficult to calculate, since the corresponding subspaces are prohibitively large. Consequently, we instead look directly at the transformation behavior of the eigenvectors under $\hat{\mathcal{U}}_{\mathrm{inv}}$, which is even in II but odd in I & III. First, observe it suffices to examine the transformation behavior of the right eigenvector $|r_2\rangle\!\rangle$, since $\langle\!\langle r_2|l_2\rangle\!\rangle \neq 0$.

We generate random product states $|\psi\rangle\!\rangle$ and calculate the overlap of $|r_2\rangle\!\rangle$ with its evenly and oddly transforming components. These can be readily obtained for pure product states by

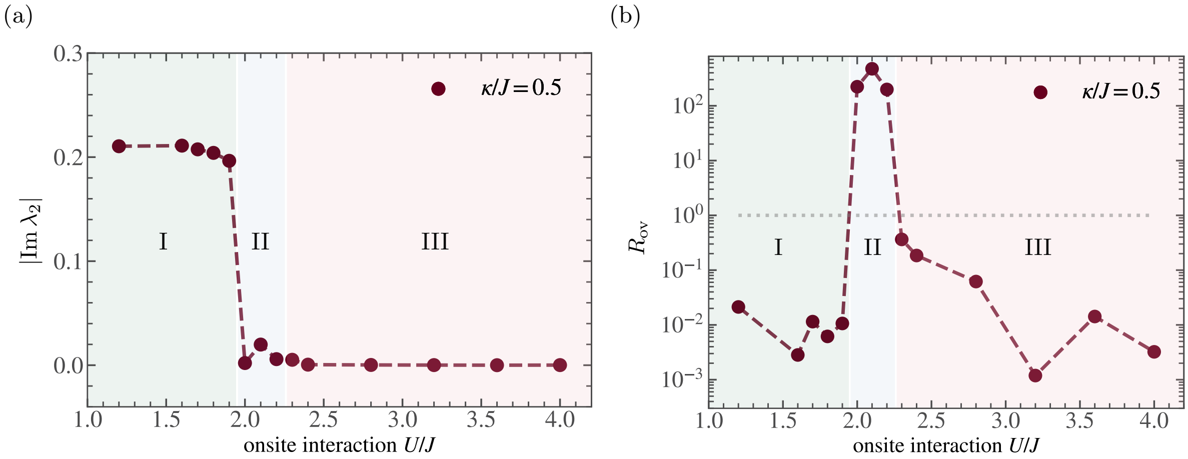

Figure 20: Slowest decaying mode depending on U/J at $\kappa/J = 0.5$ for a large-scale system with 16 sites and 8 bosons. Panel a): Modulus of λ_2-s imaginary part. Panel b): Overlap ratio R_{ov} (Eq. (4.97)) averaged over 50 random pure product states. $R_{\mathrm{ov}} \ll 1$ ($R_{\mathrm{ov}} \gg 1$) suggests that $|r_2\rangle\rangle$ transforms oddly (evenly) under $\hat{\mathcal{U}}_{\mathrm{inv}}$. The shaded areas highlight the different regions I (green), II (blue) and III (red). All data was obtained using CLIK-MPS with angle $\alpha = 0.02$, $\delta t = 0.4$ and $T = 40$, and we chose $k_0 = 0$ for the simulations. For more details on the numerical parameters and implementation see Sec. 3.2 and A.1. The plots are adapted from [1].

$|\psi_{\mathrm{even/odd}}\rangle\rangle = {}^1\!/\!\sqrt{2}\big(|\psi\rangle\rangle \pm \hat{\mathcal{U}}_{\mathrm{inv}}|\psi\rangle\rangle\big)$, respectively. We then track the overlap ratio $R_{\mathrm{ov}}(\psi)$ defined by

$$R_{\mathrm{ov}}(\psi) = \frac{\left|\langle\langle\psi_{\mathrm{even}}|r_2\rangle\rangle\right|^2}{\left|\langle\langle\psi_{\mathrm{odd}}|r_2\rangle\rangle\right|^2}\,. \tag{4.97}$$

To get rid of the dependence on the random state ψ, we take the *mean overlap ratio* R_{ov} over many random states. For the calculations in this thesis we found 50 realizations sufficient. If the right eigenmode transforms oddly we expect $R_{\mathrm{ov}} = 0$, while for even transformation behavior $R_{\mathrm{ov}} = \infty$. Since CLIK-MPS only yields an approximate eigenmode $|l_2\rangle\rangle$, we do not expect to find this exact behavior, but rather distinguish between the cases $R_{\mathrm{ov}} \ll 1$ and $R_{\mathrm{ov}} \gg 1$.

In Fig. 20 we show the analysis for a system of 16 sites and 8 bosons, with $\kappa/J = 0.5$. According to the small scale results from Figure 19 this should place us in a regime where all three phases are visible when varying U/J. Indeed, if we turn on a small onside interaction, we find a finite $\mathrm{Im}\,\lambda_2$ in Fig. 20a combined with an odd transformation behavior indicated by $R_{\mathrm{ov}} \ll 1$ in Fig. 20b, which we thus identify as region I. At $U/J = 1.95 \pm 0.05$ the behavior abruptly changes, $\mathrm{Im}\,\lambda_2$ drops to zero and $R_{\mathrm{ov}} \gg 1$, indicating the transition to region II. The mean overlap ratio again drops to $R_{\mathrm{ov}} \ll 1$ at $U/J = 2.25 \pm 0.05$, while $\mathrm{Im}\,\lambda_2$ does not change, suggesting that the slowest decaying mode again transforms oddly, and indicating the onset of region III. Notice how the behavior does not qualitatively differ from the small system discussed in Fig. 19. Most importantly, when comparing the size of region II given by ΔU_{II} at fixed $\kappa/J = 0.5$ for the two system sizes $L = 6$ and $L = 16$, we find that it does not increase with system size. This suggests that the parameter regions, where an Mpemba effect is found in this model, do not vanish with increasing system size. The quantum Mpemba effect is therefore stable and we can move on and quantify the obtained exponential speedups. But first, we need to discuss the general k_0 case.

4.5.4 Dependence of the symmetry on k_0

Our perturbative arguments in Sec. 4.5.2 were only valid for the $k_0 = 0$ case. We already established in Sec. 4.4 that there are unitary equivalences between Lindbladians with different momenta. The corresponding unitary is termed $\hat{\mathcal{U}}_{k_0}$. This reveals that in principle all of the results from Sec. 4.5.2 are applicable also in the general k_0 case, but the unitary $\hat{U}_{\text{inv}}$ needs to be transformed via $\hat{\mathcal{U}}_{k_0}$ to yield a symmetry of the Lindbladian with k_0. We find that in general

$$\hat{\mathcal{L}}_{k_0} = \hat{\mathcal{U}}_{k_0}\hat{\mathcal{U}}_{\text{inv}}^{\dagger}\hat{\mathcal{U}}_{k_0}^{\dagger}\hat{\mathcal{L}}_{k_0}\hat{\mathcal{U}}_{k_0}\hat{\mathcal{U}}_{\text{inv}}\hat{\mathcal{U}}_{k_0}^{\dagger} \, . \tag{4.98}$$

A new unitary may now be defined by $\hat{\mathcal{U}}_{\text{inv}}^{k_0} = \hat{\mathcal{U}}_{k_0}\hat{\mathcal{U}}_{\text{inv}}\hat{\mathcal{U}}_{k_0}^{\dagger}$ on the vectorized lattice, and Eq. (4.98) directly implies that it is a weak symmetry of the Lindbladian with k_0. To understand its action on creation and annihilation operators, we deduce the corresponding unitary $\hat{U}_{\text{inv}}^{k_0}$ on the physical lattice

$$\hat{U}_{\text{inv}}^{k_0} = \hat{U}_{k_0}\hat{U}_{\text{inv}}\hat{U}_{k_0}^{\dagger} \, . \tag{4.99}$$

Using Eq. (4.70) and Eq. (4.57) we finally get

$$\hat{U}_{\text{inv}}^{k_0}\hat{b}_j^{\dagger}\big(\hat{U}_{\text{inv}}^{k_0}\big)^{\dagger} = \mathrm{e}^{\mathrm{i}k_0(L+1)}\mathrm{e}^{-2\mathrm{i}k_0 j}\hat{b}_{L+1-j}^{\dagger} \, , \tag{4.100}$$

which is again a unitary with eigenvalues ±1 and is indeed a weak symmetry of $\hat{\mathcal{L}}_{k_0}$. Therefore, by substituting the initial inversion symmetry $\hat{U}_{\text{inv}}$ with this k_0-inversion symmetry, all analysis and results of Sec. 4.5.2 are trivially generalized to the general k_0-case. Care must be taken when considering $|k_0| \geq \pi/2$, since an additional unitary $\hat{\mathcal{S}}$ pops up (c.f. Eq. (4.65)). This does not change any of the results obtained before, since we find $\hat{\mathcal{S}}\hat{\mathcal{U}}_{\text{inv}}^{k_0}\hat{\mathcal{S}}^{\dagger} = \hat{\mathcal{U}}_{\text{inv}}^{k_0}$, and the resulting k_0-inversion symmetry is not affected. Therefore, the convergence to the respective steady state is the same for all Lindbladians independent of their characteristic momentum.

4.5.5 Consequences and experimentally realizable fast initial states

Knowing the class of quickly-converging initial states, we may address two important questions:

- Which states are actually easy to prepare on an optical lattice platform?
- Which state converges the fastest?

The first question is imperative, as the quicker convergence rate only matters if the difficulty of preparing the optimized initial state is similar to a random state. Interestingly, we can produce simple evenly-transforming states directly on the physical lattice by

$$|\psi_{\mathbf{n}}\rangle = |n_1, n_2, \ldots, n_{L/2}, n_{L/2}, \ldots n_2, n_1\rangle \ , \tag{4.101}$$

where $\mathbf{n} = (n_1, \ldots, n_{L/2})$ indicates the number of particles on the sites. Note that Eq. (4.101) applies to a lattice with an even number of sites L, while for an odd L the filling $n_{(L+1)/2}$ is chosen for the central site. The corresponding density matrices $\rho_{\mathbf{n}} = |\psi_{\mathbf{n}}\rangle\langle\psi_{\mathbf{n}}|$ are pure product states and transform evenly under $\hat{\mathcal{U}}_{\text{inv}}^{k_0}$ for all k_0, hence we refer to them as evenly-transforming pure product (ETPP) states. In experiment, such states can be realized by loading individual particles, one at a time, into the optical lattice. This loading procedure can be performed using optical tweezers [136, 137], which trap individual particles in a laser beam, enabling the precise control over their spatial position. This technique has shown to be very well suited for preparing certain configurations in optical lattices and related platforms, exhibiting only minor losses and

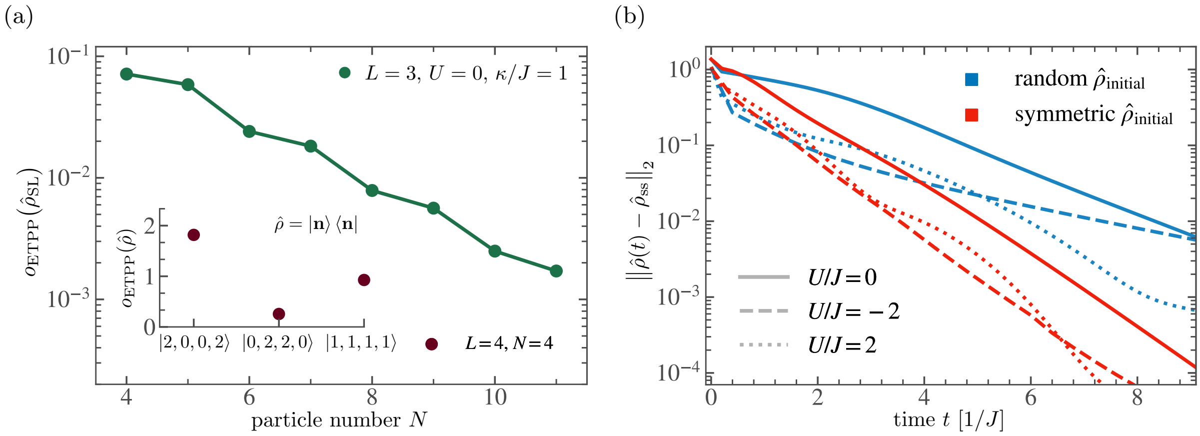

Figure 21: Panel a): Weighted overlap o_{ETPP} with $\hat{l}_3$ (c.f. Eq. (4.103)) for small system sizes using ED. For the symmetrically-localized (SL) state, o_{ETPP} vanishes exponentially with increasing particle number N. We consider a system with $L=3$. Inset: o_{ETPP} of all ETPP states of a system with 4 sites and 4 particles. For all calculations we considered $U=0$ and $\kappa/J=1$. Panel b): Distance of time-evolved states to the steady state for lattice with $L=10$ sites and $N=10$ particles. If the symmetrically-localized (SL) state is chosen to be the initial state (red), the distance converges exponentially quicker to zero than for a random initialization (blue). This holds for all considered U/J. To ensure a fair comparison, we average over 5 different random initializations. This plot is adapted from [1]. For details on the numerical parameters and implementation, see App. A.1.

decoherence [138, 139, 140, 134]. Common examples of ETPP-states include so-called wedding-cake states $|\psi\rangle = |1,\,2,\ldots,\,{}^{L}\!/\!{}_{2},\,{}^{L}\!/\!{}_{2},\,\ldots,2,\,1\rangle$, which can be readily prepared in harmonic traps without the use of tweezers [141]. These ETPP-states constitute an accessible set of initial states for the experimental utilization of the quantum Mpemba effect in the present context.

As a result, it is reasonable to restrict the search for an answer to question 2 to the set of evenly transforming pure product states. To systematically probe the ETPP-states, we need to first understand how different convergence speeds arise. Representing everything in the eigenbasis of the Lindbladian, the distance to the steady state $\hat{\rho}_{\mathrm{ss}}$ at late times $t > -1/\mathrm{Re}\,\lambda_3$ is dictated by

$$\|\hat{\rho}(t)-\hat{\rho}_{\mathrm{ss}}\|_2 = \mathrm{e}^{\mathrm{Re}(\lambda_3)t}\left|\langle\!\langle l_3|\rho_0\rangle\!\rangle\right|, \tag{4.102}$$

where we used Eq. (2.4) and that the slowest decaying mode does not contribute. We are therefore searching for an ETPP-state, which features a very small overlap $\left|\langle\!\langle l_3|\rho_0\rangle\!\rangle\right|$. To quantitatively assess this overlap, we want to compare each ETPP-state to all of the other ones, which is facilitated by the *weighted overlap* of an ETPP-state $\hat{\rho}$

$$o_{\mathrm{ETPP}}(\hat{\rho}) = \frac{\left|\langle\!\langle l_3|\rho\rangle\!\rangle\right|}{\sum_{\rho_j\in\mathrm{ETPP}}\left|\langle\!\langle l_3|\rho_j\rangle\!\rangle\right|} \times (\#\mathrm{ETPP})\,, \tag{4.103}$$

where #ETPP denotes the number of ETPP-states for the considered lattice size L and particle number N. This expression compares the overlap of the state $\hat{\rho}$ with the mean of the overlap of all ETPP-states, and we are thus interested in ETPP-states exhibiting $o_{\mathrm{ETPP}}(\hat{\rho}) \ll 1$.

For small scale systems it is easy to calculate this quantity using ED methods. In Figure 21a we plot o_{ETPP} for a variety of system sizes and particle numbers. The inset contains data for a system with 4 sites and 4 particles. With these specifications, there are three ETPP states, and we plot o_{ETPP} for all of them. The state having all particles in the central site(s) features the smallest overlap with $\hat{l}_3$, which is why we call it SL state $\hat{\rho}_{\mathrm{SL}}$ and mostly consider it throughout the rest of the section. In the main panel of Fig. 21a we now only show $o_{\mathrm{ETPP}}(\hat{\rho}_{\mathrm{SL}})$ in a system with 3 sites and several numbers of bosons N. For all considered N, the weighted overlap obeys $o_{\mathrm{ETPP}}(\hat{\rho}_{\mathrm{SL}}) \ll 1$, rendering it a perfect initial state. Moreover, o_{ETPP} vanishes exponentially with particle number N.

To convince ourself that evenly transforming stats acquire an exponential speedup, we can simulate the time evolution of a SL-state and compare it to the time evolution of random non-symmetric pure product states, where we average over 5 random initial states. The time evolutions are performed on the vectorized lattice using the numerical machinery described in Sec. 2.5, and we calculate the L_2-distance of the time-evolved states to the steady state, which is approximated by an even longer time evolution, as discussed in App. A.1. The results for a lattice spanning over 10 sites and 10 bosons at dissipation $\kappa/J = 2$ and multiple onsite interactions are shown in Fig. 21b. We clearly see the change in slope between random and SL-states, which is the key signature of the strong quantum Mpemba effect.

We may also ask about the relative reduction of time needed to prepare the steady state with a precision of some ϵ. This constitutes the time-saving we get by using an evenly-transforming state compared to some random initialization, and is consequently important for the real world applications. To put this idea on rigorous footing, we need some distance measure, which we set to be the L_2-norm. Then, the *speedup* $S(\epsilon)$ of a SL state is defined by

$$S(\epsilon) = \frac{t(\epsilon, \hat{\rho}_{\mathrm{random}})}{t(\epsilon, \hat{\rho}_{\mathrm{SL}})} , \qquad t(\epsilon, \hat{\rho}) = \min \left\{ t \,\middle|\, \|\hat{\rho}(t) - \hat{\rho}_{\mathrm{ss}}\|_2 \leq \epsilon \right\} . \tag{4.104}$$

We may ask about the properties of this quantity. Indeed, if $\epsilon \ll 1$ then $t(\epsilon, \hat{\rho}) \gg -1/\mathrm{Re}(\lambda_2)$ and we have $\|\hat{\rho}(t) - \hat{\rho}_{\mathrm{ss}}\|_2 = c_j(\rho) \mathrm{e}^{t \mathrm{Re} \lambda_j}$, where $j = 2$ for a random and $j = 3$ for the SL-state. $c_j(\rho)$ only depends on overlaps of the eigenvectors $|r_j\rangle\rangle$ and $|l_j\rangle\rangle$ with $|\rho\rangle\rangle$. Rearranging for $t(\epsilon, \hat{\rho})$ and inserting into Eq. (4.104) yields

$$S(\epsilon) = \frac{\mathrm{Re}\,\lambda_3}{\mathrm{Re}\,\lambda_2} \frac{\ln \epsilon - \ln c_2(\rho_{\mathrm{random}})}{\ln \epsilon - \ln c_3(\rho_{\mathrm{SL}})} \xrightarrow{\epsilon \ll 1} \frac{\mathrm{Re}\,\lambda_3}{\mathrm{Re}\,\lambda_2} , \tag{4.105}$$

which shows well-definedness, and a neat connection to spectral signatures of the system. To generalize, we define the *spectral speedups* Δ_j via

$$\Delta_j = \frac{\mathrm{Re}\,\lambda_j}{\mathrm{Re}\,\lambda_2} . \tag{4.106}$$

Consequently, they are closely related to the speedups $S(\epsilon)$ by $\Delta_3 = \lim_{\epsilon \to 0} S(\epsilon)$. The spectral speedups for $j > 3$ then correspond to the case of an initial state that is orthogonal to all eigenvectors $|l_k\rangle\rangle$ with $k < j$. We can calculate the speedups S by time-evolving SL- and random states sufficiently long, and employing Eq. (4.104).

In Fig. 22a, we show the speedup ratio $S(\epsilon)$ at $\epsilon = 10^{-4}$ and $\kappa/J = 2$ for a variety of lattice lengths L and particle numbers N, as well as three different onsite interactions U/J. We find that the speedups are almost independent of the lattice size and particle number. The speedups at $U/J < 0$ are much larger than at $U/J \geq 0$, and they cover the case of positive U/J at characteristic momentum $|k_0| \geq \pi/2$.

Additionally, in Fig. 22b we calculate the spectral speedups Δ_j for $j = 3$ and $j = 4$ using CLIK-MPS for the system sizes $L = 10$ and $L = 20$ at half filling $N/L = 0.5$. At least for Δ_3, we expect the ratios to match the results of Fig. 22a due to Eq. (4.105). Indeed, Δ_3 is quite insensitive to the system size as well as the onsite interaction U/J, staying between 1.5 and 1.8

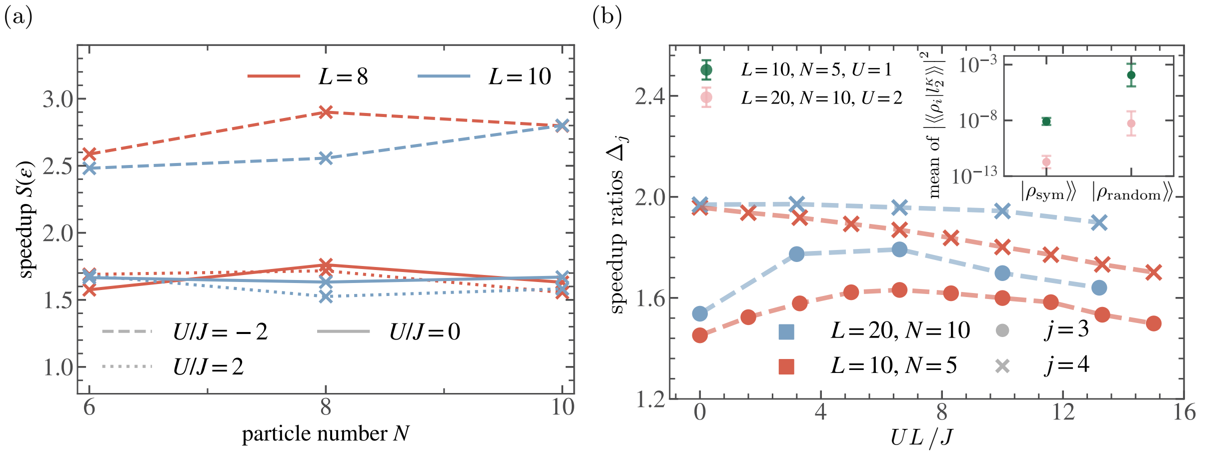

Figure 22: Quantifying the Mpemba speedups for large-scale systems. Panel a): Speedup $S(\epsilon)$ defined in Eq. (4.104) for $\epsilon = 10^{-4}$ depending on the system specifications L, N, U/J at $\kappa/J = 2$ and $k_0 = 0$. Speedups are calculated numerically by time evolutions on the vectorized lattice. Panel b): Spectral speedups Δ_j (c.f. Eq. (4.106)) for large-scale systems obtained from CLIK-MPS. We show the first two spectral speedup ratios $\Delta_{3,4}$ for systems with 10 and 20 sites at half filling and $\kappa/J = 2$. Note that Δ_j increases with system size, and that Panel b) is in agreement with the speedups $S(\epsilon)$, as predicted by the limit behavior Eq. (4.105). Inset: Mean overlaps of different product states with the obtained slowest decaying left eigenmode $|l_2^K\rangle\rangle$. The mean was calculated with 50 randomly sampled symmetric states ($|\rho_{\text{sym}}\rangle\rangle$) and random product states ($|\rho_{\text{random}}\rangle\rangle$), respectively. For symmetric states, the overlap is 4 orders of magnitude smaller, indicating the emergence of the quantum Mpemba effect. The error bars show that this behavior is systematic. For the CLIK-MPS calculations, we used $\alpha = 0.05$, $\delta t = 0.1$ and $T = 12$ for $L = 10$, while $\alpha = 0.02$ and $\delta t = 0.2$ was chosen for $L = 20$. For $L = 20$, T was chosen such that convergence is reached, which we checked in Fig. 22b. For more information on the numerical implementation see App. A.1. Panel a) and b) is adapted from [1] and [2], respectively.

similar to the speedups $S(\epsilon)$. Interestingly however, they feature a maximum at $UL/J \approx 6.5$ and slowly increase with system size. Δ_4 on the other hand decreases monotonically.

The large-scale analysis provided here also gives some information on previously discussed phenomena. For one, the imaginary part of the eigenvalue λ_2, which was calculated for the spectral speedup ratios in Fig. 22b is finite for all parameters shown here, which establishes that these parameters lie in region I (c.f. Fig. 19). This proves the stability of region I even beyond the system sizes discussed in Figure 20.

To really showcase the quantum Mpemba effect in these large scale systems, we calculate overlaps of the slowest decaying left eigenmode with symmetric ($|\rho_{\text{sym}}\rangle\rangle$) and general ($|\rho_{\text{random}}\rangle\rangle$) random states in the inset of Fig. 22b for 10 and 20 sites using CLIK-MPS. Targeting left eigenmodes requires time evolving with the adjoint Lindbladian $\hat{\mathcal{L}}^\dagger$ as discussed in Sec. 3.2.3. We each average over 50 random and symmetric states and plot the mean overlap combined with the standard deviation. We find that the overlaps with symmetric states are 4 orders of magnitude smaller than with random states, indicating the emergence of the quantum Mpemba effect.

Lastly, we are now able to address the question raised at the beginning of this chapter, in Section 4.1. Here, we observed that the number of particles in the k_0-mode approaches the total number of particles N exponentially, if we turn off the Hamiltonian part and only account for the dissipative dynamics in the Lindbladian. However, the exponential convergence was not governed by the slowest decaying mode, as we expected. Additionally, this behavior was universal and did not depend on the initial state. After all of the analysis concerning the quantum Mpemba effect, it seems natural that this observation is closely tied to the inversion symmetry. Indeed, if we write out the dynamics of the expectation value of the number of particles in the k_0-mode for some initial state $\hat{\rho}_0$ we find

$$\langle \hat{n}_{k_0}(t) \rangle = \mathrm{Tr}\big(\hat{n}_{k_0}\hat{\rho}_0(t)\big) = \mathrm{Tr}\big(\hat{n}_{k_0}\hat{\rho}_{\mathrm{ss}}\big) + \sum_{n\geq 2} \mathrm{Tr}\big(\hat{n}_{k_0}\hat{r}_n\big)\mathrm{Tr}\big(\hat{l}_n^{\dagger}\hat{\rho}_0\big)\mathrm{e}^{\lambda_n t} \,. \tag{4.107}$$

If we look at the right-hand side, the time dependence is located inside the sum, and the exponential decay is dictated by the slowest decaying mode. The corresponding prefactor consists of the overlaps $\langle\langle l_2|\rho_0\rangle\rangle$ and $\langle\langle n_{k_0}|r_2\rangle\rangle$. The first one is certainly zero for initial states that are evenly symmetric. However, we found that the convergence behavior is independent of the initial state, so there has to be another mechanism at work. The second overlap is a bit more tedious to work out. Through our analysis in Sec. 4.5.2 and 4.5.3 we found that both $|l_2\rangle\rangle$ and $|r_2\rangle\rangle$ are oddly transforming. Therefore, we are interested in the transformation behavior of $\hat{n}_{k_0}$. We do this analysis only for the case $k_0 = 0$, since all other momenta can be directly inferred due to the unitary equivalences (see Sec. 4.4 and 4.5.4). Applying the inversion to the operator yields

$$\hat{U}_{\mathrm{inv}}^{\dagger}\hat{n}_{k_0=0}\hat{U}_{\mathrm{inv}} = \frac{1}{L}\sum_{j=1}^{L}\hat{U}_{\mathrm{inv}}^{\dagger}\hat{n}_j\hat{U}_{\mathrm{inv}} = \frac{1}{L}\sum_{j=1}^{L}\hat{n}_{L+1-j} = \hat{n}_{k_0=0} \,, \tag{4.108}$$

where we used the representation of $\hat{n}_{k_0=0}$ in terms of site particle operators $\hat{n}_j$. This calculation shows that the particle operator $\hat{n}_{k_0}$ is evenly transforming, which means that the overlap $\langle\langle n_{k_0}|r_2\rangle\rangle$ is always zero. Thus, the first term in the sum on the right-hand side of Eq. (4.107) is always zero, and the exponential convergence should go according to $\mathrm{Re}\,\lambda_3$. And indeed, the real part of λ_3 for the specific case considered in Figure 11 matches the exponential decay perfectly.

5 Discussion and outlook

Quantum systems coupled to environments arise in many settings, such as light-harvesting complexes [142], molecular aggregates [143], magnetic-impurity models [144], and, most prominently, in the control of strong light-matter interactions [11, 12] and optically driving ultracold atoms in optical lattices [57, 58, 59, 60, 61, 62, 63]. This makes a theoretical description imperative, and the theory of open quantum systems provides the natural language to describe such systems. From the theoretical side, open quantum systems have also attracted increasing attention due to diverse phenomena including dissipative phase transitions [3, 4, 5], anomalous thermalization [6], and metastability [22]. However, open quantum systems remain very difficult to treat both analytically and numerically due to their inherent non-Hermiticity and the interplay between coherent internal dynamics with dissipative and decohering influences from the environment.

In this thesis, we took a step toward mitigating the numerical challenges and explored several analytical questions as well. We introduced CLIK-MPS, a tensor-network-based framework that enables the calculation of the steady state, dissipative gap, and a set of low-lying Lindbladian eigenvalues and eigenmodes. To achieve this, we built upon advances in Krylov space techniques based on real [110] and complex [56] time-evolved states. We introduced specific complex contours to span optimized Krylov spaces and thoroughly analyzed their effect on the time evolution. Additionally, we devised physically motivated warm-up procedures to enhance the contribution of the steady state. Crucially, we also found a way to generate states that do not converge to the steady state but to the slowest decaying mode, which enhances the ability to represent the low-lying eigenvalues. The resulting framework is complemented by efficient schemes to calculate expectation values and overlaps directly within the Krylov space. We also developed efficient methods to enforce Hermiticity and symmetries in expectation values. We outlined possible generalizations of the framework to the even more challenging realm of non-Markovian environments. To assess the quality of the approximated spectrum, we proposed straightforward numerical methods to check the convergence of specific eigenvalues and eigenmodes. Benchmarking the framework against exact diagonalization (ED) reference data and a recently proposed Krylov-space approach [110] yielded improvements of up to four orders of magnitude in the approximation of excited eigenmodes.

To showcase the unprecedented capabilities of CLIK-MPS, we analyzed the properties of a dissipative state preparation (DSP) protocol for generating Bose-Einstein condensates (BECs) on optical lattices [17]. Performing a mean-field analysis to assess the steady-state properties, we found that the prepared state is equivalent to a thermal state of an isolated Bose-Hubbard model with a renormalized onsite interaction. In another parameter regime, the steady-state corresponds to a zero-temperature equilibrium state of a Bose-Hubbard model. These insights imply that a BEC is stabilized at finite system sizes, a phenomenon termed a local BEC [17, 1]. We verified our predictions using CLIK-MPS for large-scale systems with up to 32 sites, beyond the reach of standard techniques. Additionally, we numerically investigated the finite-size scaling of the dissipative gap Δ, uncovering strong evidence for the transition from a diffusive $\Delta \sim L^{-1}$ to a $\Delta \sim L^{-3/2}$ behav ior once a local BEC forms. This is strong evidence for the emergence of the KPZ universality class in a driven, interacting many-body setting using CLIK-MPS for systems up to 32 sites.

This, however, entails a (super-)linear scaling of the preparation time, which limits the efficient preparation of a BEC using this protocol. To alleviate this restriction, we investigated the quantum Mpemba effect, which originally referred to a non-equilibrium phenomenon where hot systems cool faster than warm ones. Applying this effect to accelerate DSP protocols was previously hindered by the need to orthogonalize the initial state to the slowest decaying mode, which requires diagonalizing the Lindbladian. We analytically circumvent this obstacle by exploiting a weak discrete symmetry, which enforces a block-diagonal structure in the Lindbladian. After identifying the symmetry properties of the slowest decaying mode, we found experimentally realizable initial states that avoid these slow-decaying symmetry channels. Importantly, we numerically confirmed the validity of our arguments for multiple large-scale systems and wide parameter ranges and quantified the resulting exponential speedups using CLIK-MPS.

Beyond the specific application studied here, our analysis reveals that the potential applications of CLIK-MPS span the numerical investigation of exceptional points [145, 146], DPTs [3, 4], dissipative time crystals [147, 148], and metastability [22] in large-scale, strongly-interacting, open quantum systems. Additionally, there are several avenues for algorithmic improvement, such as combining multiple complex contours, further optimizing the warm-up procedures, or advanced convergence analysis. Although we argued that the treatment of non-Markovian environments should be similar to the Markovian case studied here, CLIK-MPS remains to be tested in this even more challenging realm.

Despite significant efforts to understand the physics of the dissipative Bose-Hubbard model, the theoretical origin of the emergence of the KPZ universality class remains unresolved, and we aim to rigorously investigate this phenomenon in future work. Additionally, while an experimental realization of the dissipative Bose-Hubbard model is still to be performed [17], our proposal for finding rapidly converging states is general and may also apply to other, more easily realizable DSP protocols, for instance, η-paired superconducting states in ultracold atoms [149].

A Appendix

A.1 Appendix A: Further numerical details

As discussed in the main text, time evolution is carried out using LSE-TDVP within the SyTen toolkit [106, 107]. As we pointed out in the main text, the dissipative Bose-Hubbard model Eq. (3.1) possesses a strong $U(1)$-symmetry associated with the conservation of the total particle number. Since the lattice is doubled during vectorization, this single $U(1)$-symmetry induces two $U(1)$-symmetries on the vecotrized lattice, corresponding to particle number conservation on the physical and auxiliary sublattice individually. We can make use of this structure by implementing it directly into the MPS representation. Note that the second $U(1)$-symmetry is crucial, since it enforces a block diagonal structure to the Lindbladian which separates physical from unphysical sectors. Therefore, taking this symmetry into account during the numerical implementation is crucial and prevents truncation errors to lead to contributions in the unphysical subspace, potentially introducing unphysical vectors into the Krylov space. Additionally, the symmetries lead to an exact representation with a local Hilbert space dimension of $d = N+1$, which we chose for all our calculations. Due to the rapid increase in bond dimension in the first few timesteps, especially when starting from a pure state, we employ a smaller step size at the beginning, which is increased afterwards. In case of CLIK-MPS-calculations, this initial timestep lies at $\mathrm{d}t = 0.001$, while it is increased after 10 steps to $\mathrm{d}t = 0.01$. For all other calculations, we initially use a time step of 5×10^{-4} and increase it after 20 steps to either 0.01 or 0.005 (for large scale calculations also 0.002), depending on system size. The maximal bond dimensions chosen for the time evolution vary between 1400 and 2400 for the CLIK-MPS calculations. If not stated differently, calculations with $L = 20$ and $L = 10$ are performed with $\chi = 2400$, while for all other we chose $\chi = 1400$. Time evolutions performed independently of CLIK-MPS were initialized with $\chi = 2000$.

Some MPS-calculations in Section 4 needed the knowledge of the steady state to calculate $\|\hat{\rho}(t) - \hat{\rho}_{\mathrm{ss}}\|_2$, but were performed without CLIK-MPS. For those, we obtained the steady state by a long-time evolution $\hat{\rho}_{\mathrm{ss}} \approx \hat{\rho}(t_{\max})$ and we can track if it is sufficiently converged similarly to the methods introduced in Sec. 3.3.2. Calculating $\|\hat{\rho}(t) - \hat{\rho}_{\mathrm{ss}}\|_2$ when considering $\hat{\rho}(t_{\max})$ and $\hat{\rho}(t_{\max} - \Delta t)$ as the approximate steady state for a sufficiently big Δt serves as a convergence analysis. For the data shown in Fig. 12a we also perform a similar analysis as in Sec. 3.3.2 by tracking if the leading eigenvalue of the OBDM $\boldsymbol{\gamma}$ is converged.

A.2 Appendix B: Using symmetries in the Bose-Hubbard model

In Section 3.2.5 we provided general expressions on how to utilize symmetries and enforce them inside the Krylov space. The dissipative Bose-Hubbard model, which is extensively studied in Section 4, features a discrete $\mathbb{Z}_2$-symmetry, which is given by Eq. (4.70) and amounts to an inversion of the lattice around the central site(s). Since it is a weak symmetry, enforcing it directly during the time evolution is not possible. However, we can use Equation (3.31) to take it into account when calculating expectation values. We are mainly interested in the OBDM $\gamma_{kj} = \langle \hat{b}_j^\dagger \hat{b}_k \rangle_{\mathrm{ss}}$, which means we chose $\hat{A}_{j,k} = \hat{b}_j^\dagger \hat{b}_k$. To use Equation (3.31) and (3.30) we need to calculate the action of the unitary on our operator

$$\frac{1}{N_S} \sum_{n=0}^{N_S-1} (\hat{U}_{\mathrm{inv}}^\dagger)^n \hat{A}_{j,k} \hat{U}_{\mathrm{inv}}^n = \frac{1}{2}\Big(\hat{A}_{j,k} + \hat{A}_{L+1-j,L+1-k}\Big) , \tag{A.1}$$

where we used that $N_S = 2$ and the explicit action of U_{inv} on creation and annihilation operators from Eq. (4.70). Note that this implies, that the symmetrization of the expectation value is a linear operation on the elements of the OBDM

$$\gamma^{\mathrm{symm}}_{j,k} = \frac{1}{2}\big(\gamma_{j,k} + \gamma_{L+1-j,L+1-k}\big)\,, \tag{A.2}$$

with $\boldsymbol{\gamma}$ being the OBDM before and $\boldsymbol{\gamma}^{\mathrm{symm}}$ after symmetrization of the approximate steady state. This shows, that the computational complexity is not affected by the symmetrization procedure.

Also the strong $U(1)$-symmetry can be used to simplify calculations. Calculating expectation values and overlaps in the vecotrized picture requires the knowledge of the vectorized identity $|\mathbb{1}\rangle\rangle$. In a general system with L sites and a local $(N+1)$-dimensional Hilbert space, the vectorized identity can be built by [105]

$$|\mathbb{1}\rangle\rangle = \sum_{n_1,\dots,n_L=0}^{N} |n_1, n_1, \dots, n_L, n_L\rangle = \prod_{j=1}^{L} \hat{S}_j |0\rangle\rangle\,, \tag{A.3}$$

where we defined the operators $\hat{S}_j$

$$\hat{S}_j = \sum_{n=0}^{N} \frac{1}{n!} \big[\hat{b}_j^{\mathrm{p}\dagger}\big]^n \big[\hat{b}_j^{\mathrm{a}\dagger}\big]^n\,, \tag{A.4}$$

and we denote operators acting on the physical (auxiliary) sites by p (a). However, we always consider states with a certain fixed number of particles N, which is conserved in the dynamics due to the strong $U(1)$-symmetry. We can project the vectorized identity directly into the corresponding particle sector [54]. For this, we define the operator

$$\hat{C}_{\mathrm{tot}} = \sum_{j=1}^{L} \hat{b}_j^{\mathrm{p}\,\dagger} \hat{b}_j^{\mathrm{a}\,\dagger}\,, \tag{A.5}$$

which creates pairs of bosons on the physical and auxiliary sublattices. The vectorized identity for N particles is given by

$$|\mathbb{1}\rangle\rangle = \frac{1}{N!} \hat{C}_{\mathrm{tot}}^{N} \,|\mathrm{vac}\rangle\ . \tag{A.6}$$

This relation is easily proven using the multinomial theorem. Building the vectorized identity according to Eq. (A.6) is computationally much more efficient, and we employ it throughout the thesis.

Acknowledgments

I would like to begin by expressing my deepest gratitude to *Prof. Ulrich Schollwöck*, *Dr. Sebastian Paeckel* and *Dr. Mattia Moroder* for their support, guidance, and countless hours of advice throughout this work. Their deep understanding and passion for physics are truly inspiring.

I am especially thankful to *Dr. Sebastian Paeckel* for his foresight, which led to the collaboration with *Dr. Mattia Moroder* and ultimately shaped the topic of this thesis. His help with the many tedious implementational challenges and analytic questions along the way was invaluable. My heartfelt thanks also go to *Dr. Mattia Moroder* whose deep expertise in open quantum systems, generous advice, and many hours of discussion were essential to this work. Thanks to you two also for proof-reading this thesis.

I am really grateful to both of you and am excited to work on many more projects together. It just makes a hell of fun to do research with you two!

I would also like to thank *Dr. François Damanet*, *Prof. John Martin* and *Baptiste Debecker* for their collaboration and valuable input on the CLIK-MPS framework and non-Markovian systems. I look forward to continuing our fruitful collaboration.

A huge thanks goes out to my colleagues from my Bachelor's and Master's studies. The countless hours we spent studying together made daily life so much better. To give a non-exhaustive list, thanks to *Fabi*, *Daphne*, *Marie*, *Luca*, *Tobi*, *Michi*, *Joshua*, *Marco*, *Niko*, *Luc*, *Thomas*, *Flori*, *Benjamin*, *Leo*, and *Daniel.*

Lastly, deeply grateful to *my family* and *my partner* for their encouragement, constant support and simply being awesome people.

I also gratefully acknowledge *the computational resources provided by the ASC.*

Glossary

1BZ First Brillouin zone. 43, 52

1D one-dimensional. 33, 42

BEC Bose-Einstein condensate. 3, 8, 19, 41–43, 45, 49, 52–55, 59, 77

CLIK-MPS complex-time Lindbladian Krylov subspace MPS. 7, 8, 18–21, 23, 30, 33, 35–41, 54, 55, 59, 60, 66–68, 70, 71, 74, 75, 77–79

DMRG density matrix renormalization group. 7, 16

DPT dissipative phase transition. 7, 18, 55, 78

DSP dissipative state preparation. 7, 8, 19, 41, 42, 77, 78

ED exact diagonalization. 6, 7, 18, 20, 21, 35, 36, 44, 60, 66–69, 73, 77

ETPP evenly-transforming pure product. 72, 73

HEOM hierarchical equations of motion. 33

ISPT in-spectrum phase transition. 70

KPZ Kardar-Parisi-Zhang. 3, 8, 41, 55, 56, 77, 78

LSE local subspace expansion. 35

LSE-TDVP local subspace expansion time-dependent variational principle. 17, 79

MPO matrix-product operator. 16, 17, 19

MPS matrix-product state. 8, 9, 15–18, 21–23, 28–31, 33, 41, 79

OBC open boundary condition. 42, 61

OBDM one-body reduced density matrix. 38, 52–54, 58, 79, 80

ONB orthonormal basis. 21–23, 29

SL symmetrically-localized. 73, 74

SVD singular value decomposition. 16

TD thermodynamic. 16, 52, 53, 66

TDVP time-dependent variational principle. 17, 33, 35

TN tensor-network. 7, 17, 20, 77

References

[1] Philipp Westhoff, Sebastian Paeckel, and Mattia Moroder. Fast and direct preparation of a genuine lattice bec via the quantum mpemba effect. *arXiv preprint arXiv:2504.05549*, 2025. URL `https://arxiv.org/abs/2504.05549`.

[2] Philipp Westhoff, Mattia Moroder, Ulrich Schollwöck, and Sebastian Paeckel. A tensor network framework for lindbladian spectra and steady states. *arXiv preprint arXiv:2509.07709*, 2025.

[3] Fabrizio Minganti, Alberto Biella, Nicola Bartolo, and Cristiano Ciuti. Spectral theory of liouvillians for dissipative phase transitions. *Phys. Rev. A*, 98:042118, Oct 2018. doi: 10.1103/PhysRevA.98.042118. URL `https://link.aps.org/doi/10.1103/PhysRevA.98.042118`.

[4] Fabrizio Minganti, Vincenzo Savona, and Alberto Biella. Dissipative phase transitions in n-photon driven quantum nonlinear resonators. *Quantum*, 7:1170, November 2023. ISSN 2521-327X. doi: 10.22331/q-2023-11-07-1170. URL `https://doi.org/10.22331/q-2023-11-07-1170`.

[5] Baptiste Debecker, John Martin, and Fran çois Damanet. Spectral theory of non-markovian dissipative phase transitions. *Phys. Rev. A*, 110:042201, Oct 2024. doi: 10.1103/PhysRevA.110.042201. URL `https://link.aps.org/doi/10.1103/PhysRevA.110.042201`.

[6] Mattia Moroder, Oisín Culhane, Krissia Zawadzki, and John Goold. Thermodynamics of the quantum mpemba effect. *Phys. Rev. Lett.*, 133:140404, Oct 2024. doi: 10.1103/PhysRevLett.133.140404. URL `https://link.aps.org/doi/10.1103/PhysRevLett.133.140404`.

[7] Ehud Altman, Kenneth R. Brown, Giuseppe Carleo, Lincoln D. Carr, Eugene Demler, Cheng Chin, Brian DeMarco, Sophia E. Economou, Mark A. Eriksson, Kai-Mei C. Fu, Markus Greiner, Kaden R.A. Hazzard, Randall G. Hulet, Alicia J. Kollár, Benjamin L. Lev, Mikhail D. Lukin, Ruichao Ma, Xiao Mi, Shashank Misra, Christopher Monroe, Kater Murch, Zaira Nazario, Kang-Kuen Ni, Andrew C. Potter, Pedram Roushan, Mark Saffman, Monika Schleier-Smith, Irfan Siddiqi, Raymond Simmonds, Meenakshi Singh, I.B. Spielman, Kristan Temme, David S. Weiss, Jelena Vučković, Vladan Vuletić, Jun Ye, and Martin Zwierlein. Quantum simulators: Architectures and opportunities. *PRX Quantum*, 2:017003, Feb 2021. doi: 10.1103/PRXQuantum.2.017003. URL `https://link.aps.org/doi/10.1103/PRXQuantum.2.017003`.

[8] Flavien Gyger, Maximilian Ammenwerth, Renhao Tao, Hendrik Timme, Stepan Snigirev, Immanuel Bloch, and Johannes Zeiher. Continuous operation of large-scale atom arrays in optical lattices. *Phys. Rev. Res.*, 6:033104, Jul 2024. doi: 10.1103/PhysRevResearch.6.033104. URL `https://link.aps.org/doi/10.1103/PhysRevResearch.6.033104`.

[9] Lars S Madsen, Fabian Laudenbach, Mohsen Falamarzi Askarani, Fabien Rortais, Trevor Vincent, Jacob F F Bulmer, Filippo M Miatto, Leonhard Neuhaus, Lukas G Helt, Matthew J Collins, Adriana E Lita, Thomas Gerrits, Sae Woo Nam, Varun D Vaidya, Matteo Menotti, Ish Dhand, Zachary Vernon, Nicolás Quesada, and Jonathan

Lavoie. Quantum computational advantage with a programmable photonic processor. *Nature*, 606(7912):75–81, June 2022. URL `https://www.nature.com/articles/s41586-022-04725-x`.

[10] Acharya et al. Quantum error correction below the surface code threshold. *Nature*, 638(8052):920–926, February 2025. URL `https://www.nature.com/articles/s41586-024-08449-y`.

[11] Denis G. Baranov, Martin Wersäll, Jorge Cuadra, Tomasz J. Antosiewicz, and Timur Shegai. Novel nanostructures and materials for strong light–matter interactions. *ACS Photonics*, 5(1):24–42, 2018. doi: 10.1021/acsphotonics.7b00674. URL `https://doi.org/10.1021/acsphotonics.7b00674`.

[12] Wei Qin, Anton Frisk Kockum, Carlos Sánchez Muñoz, Adam Miranowicz, and Franco Nori. Quantum amplification and simulation of strong and ultrastrong coupling of light and matter. *Physics Reports*, 1078:1–59, 2024. ISSN 0370-1573. doi: https://doi.org/10.1016/j.physrep.2024.05.003. URL `https://www.sciencedirect.com/science/article/pii/S0370157324001571`.

[13] Jihene Zribi, Lama Khalil, Biyuan Zheng, José Avila, Debora Pierucci, Thibault Brulé, Julien Chaste, Emmanuel Lhuillier, Maria C Asensio, Anlian Pan, and Abdelkarim Ouerghi. Strong interlayer hybridization in the aligned SnS2/WSe2 hetero-bilayer structure. *npj 2D Materials and Applications*, 3(1):27, July 2019. URL `https://www.nature.com/articles/s41699-019-0109-3`.

[14] Shaofeng Duan, Yun Cheng, Wei Xia, Yuanyuan Yang, Chengyang Xu, Fengfeng Qi, Chaozhi Huang, Tianwei Tang, Yanfeng Guo, Weidong Luo, Dong Qian, Dao Xiang, Jie Zhang, and Wentao Zhang. Optical manipulation of electronic dimensionality in a quantum material. *Nature*, 595(7866):239–244, July 2021. URL `https://www.nature.com/articles/s41586-021-03643-8`.

[15] G. Lindblad. On the generators of quantum dynamical semigroups. *Communications in Mathematical Physics*, 48(2):119 – 130, 1976.

[16] Frank Verstraete, Michael M Wolf, and J Ignacio Cirac. Quantum computation and quantum-state engineering driven by dissipation. *Nature physics*, 5(9):633–636, 2009.

[17] S Diehl, A Micheli, A Kantian, B Kraus, H P Büchler, and P Zoller. Quantum states and phases in driven open quantum systems with cold atoms. *Nature Physics*, 4(11):878–883, November 2008. URL `https://www.nature.com/articles/nphys1073`.

[18] Federico Carollo, Antonio Lasanta, and Igor Lesanovsky. Exponentially accelerated approach to stationarity in markovian open quantum systems through the mpemba effect. *Phys. Rev. Lett.*, 127:060401, Aug 2021. doi: 10.1103/PhysRevLett.127.060401. URL `https://link.aps.org/doi/10.1103/PhysRevLett.127.060401`.

[19] Fei Song, Shunyu Yao, and Zhong Wang. Non-hermitian skin effect and chiral damping in open quantum systems. *Phys. Rev. Lett.*, 123:170401, Oct 2019. doi: 10.1103/PhysRevLett.123.170401. URL `https://link.aps.org/doi/10.1103/PhysRevLett.123.170401`.

[20] Simon Lieu, Max McGinley, and Nigel R. Cooper. Tenfold way for quadratic lindbladians. *Phys. Rev. Lett.*, 124:040401, Jan 2020. doi: 10.1103/PhysRevLett.124.040401. URL `https://link.aps.org/doi/10.1103/PhysRevLett.124.040401`.

[21] Tsuneya Yoshida, Koji Kudo, Hosho Katsura, and Yasuhiro Hatsugai. Fate of fractional quantum hall states in open quantum systems: Characterization of correlated topological states for the full liouvillian. *Phys. Rev. Res.*, 2:033428, Sep 2020. doi: 10.1103/PhysRevResearch.2.033428. URL `https://link.aps.org/doi/10.1103/PhysRevResearch.2.033428`.

[22] Katarzyna Macieszczak, Măd ălin Guţă, Igor Lesanovsky, and Juan P. Garrahan. Towards a theory of metastability in open quantum dynamics. *Phys. Rev. Lett.*, 116:240404, Jun 2016. doi: 10.1103/PhysRevLett.116.240404. URL `https://link.aps.org/doi/10.1103/PhysRevLett.116.240404`.

[23] Tomaž Prosen. Third quantization: a general method to solve master equations for quadratic open fermi systems. *New Journal of Physics*, 10(4):043026, apr 2008. doi: 10.1088/1367-2630/10/4/043026. URL `https://dx.doi.org/10.1088/1367-2630/10/4/043026`.

[24] Gabriel T. Landi, Dario Poletti, and Gernot Schaller. Nonequilibrium boundary-driven quantum systems: Models, methods, and properties. *Rev. Mod. Phys.*, 94:045006, Dec 2022. doi: 10.1103/RevModPhys.94.045006. URL `https://link.aps.org/doi/10.1103/RevModPhys.94.045006`.

[25] S. R. White. Density matrix formulation for quantum renormalization groups. *Phys. Rev. Lett.*, 69:2863, Nov 1992. URL `https://link.aps.org/doi/10.1103/PhysRevLett.69.2863`.

[26] Steven R. White. Density-matrix algorithms for quantum renormalization groups. *Phys. Rev. B*, 48(14):10345–10356, Oct 1993. doi: 10.1103/PhysRevB.48.10345. URL `https://link.aps.org/doi/10.1103/PhysRevB.48.10345`.

[27] U. Schollwöck. The density-matrix renormalization group in the age of matrix product states. *Ann. Phys.*, 326(1):96, 2011. ISSN 0003-4916. URL `https://www.sciencedirect.com/science/article/pii/S0003491610001752`.

[28] Ulrich Schollwöck. The density-matrix renormalization group. *Reviews of modern physics*, 77(1):259–315, 2005.

[29] F. Verstraete, J. J. García-Ripoll, and J. I. Cirac. Matrix product density operators: Simulation of finite-temperature and dissipative systems. *Phys. Rev. Lett.*, 93:207204, Nov 2004. doi: 10.1103/PhysRevLett.93.207204. URL `https://link.aps.org/doi/10.1103/PhysRevLett.93.207204`.

[30] Tomaž Prosen and Marko Žnidarič. Matrix product simulations of non-equilibrium steady states of quantum spin chains. *Journal of Statistical Mechanics: Theory and Experiment*, 2009(02):P02035, feb 2009. doi: 10.1088/1742-5468/2009/02/P02035. URL `https://dx.doi.org/10.1088/1742-5468/2009/02/P02035`.

[31] Jian Cui, J. Ignacio Cirac, and Mari Carmen Bañuls. Variational matrix product operators for the steady state of dissipative quantum systems. *Phys. Rev. Lett.*, 114:220601, Jun 2015. doi: 10.1103/PhysRevLett.114.220601. URL `https://link.aps.org/doi/10.1103/PhysRevLett.114.220601`.

[32] Eduardo Mascarenhas, Hugo Flayac, and Vincenzo Savona. Matrix-product-operator approach to the nonequilibrium steady state of driven-dissipative quantum arrays. *Phys. Rev. A*, 92:022116, Aug 2015. doi: 10.1103/PhysRevA.92.022116. URL `https://link.aps.org/doi/10.1103/PhysRevA.92.022116`.

[33] A. H. Werner, D. Jaschke, P. Silvi, M. Kliesch, T. Calarco, J. Eisert, and S. Montangero. Positive tensor network approach for simulating open quantum many-body systems. *Phys. Rev. Lett.*, 116:237201, Jun 2016. doi: 10.1103/PhysRevLett.116.237201. URL `https://link.aps.org/doi/10.1103/PhysRevLett.116.237201`.

[34] Augustine Kshetrimayum, Hendrik Weimer, and Román Orús. A simple tensor network algorithm for two-dimensional steady states. *Nature Communications*, 8(1):1291, November 2017.

[35] Adil A. Gangat, Te I, and Ying-Jer Kao. Steady states of infinite-size dissipative quantum chains via imaginary time evolution. *Phys. Rev. Lett.*, 119:010501, Jul 2017. doi: 10.1103/PhysRevLett.119.010501. URL `https://link.aps.org/doi/10.1103/PhysRevLett.119.010501`.

[36] Alejandro D. Somoza, Oliver Marty, James Lim, Susana F. Huelga, and Martin B. Plenio. Dissipation-assisted matrix product factorization. *Phys. Rev. Lett.*, 123:100502, Sep 2019. doi: 10.1103/PhysRevLett.123.100502. URL `https://link.aps.org/doi/10.1103/PhysRevLett.123.100502`.

[37] Stefan Wolff, Ameneh Sheikhan, and Corinna Kollath. Numerical evaluation of two-time correlation functions in open quantum systems with matrix product state methods: a comparison. *SciPost Phys. Core*, 3:010, 2020. doi: 10.21468/SciPostPhysCore.3.2.010. URL `https://scipost.org/10.21468/SciPostPhysCore.3.2.010`.

[38] Chu Guo. Density matrix renormalization group algorithm for mixed quantum states. *Phys. Rev. B*, 105:195152, May 2022. doi: 10.1103/PhysRevB.105.195152. URL `https://link.aps.org/doi/10.1103/PhysRevB.105.195152`.

[39] Hannes Pichler, Johannes Schachenmayer, Andrew J. Daley, and Peter Zoller. Heating dynamics of bosonic atoms in a noisy optical lattice. *Phys. Rev. A*, 87:033606, Mar 2013. doi: 10.1103/PhysRevA.87.033606. URL `https://link.aps.org/doi/10.1103/PhysRevA.87.033606`.

[40] S. Sarkar, S. Langer, J. Schachenmayer, and A. J. Daley. Light scattering and dissipative dynamics of many fermionic atoms in an optical lattice. *Phys. Rev. A*, 90:023618, Aug 2014. doi: 10.1103/PhysRevA.90.023618. URL `https://link.aps.org/doi/10.1103/PhysRevA.90.023618`.

[41] Mattia Moroder, Martin Grundner, Franccois Damanet, Ulrich Schollwock, Sam Mardazad, Stuart Flannigan, Thomas Kohler, and Sebastian Paeckel. Stable bipolarons in open quantum systems. *Physical Review B*, 2022. URL `https://api.semanticscholar.org/CorpusID:259309444`.

[42] Zhaoxuan Xie, Mattia Moroder, Ulrich Schollwöck, and Sebastian Paeckel. Photo-induced dynamics with continuous and discrete quantum baths. *The Journal of Chemical Physics*, 161(7):074109, 08 2024. ISSN 0021-9606. doi: 10.1063/5.0221574. URL `https://doi.org/10.1063/5.0221574`.

[43] Dawid A. Hryniuk and Marzena H. Szymańska. Tensor-network-based variational Monte Carlo approach to the non-equilibrium steady state of open quantum systems. *Quantum*, 8:1475, September 2024. ISSN 2521-327X. doi: 10.22331/q-2024-09-17-1475. URL `https://doi.org/10.22331/q-2024-09-17-1475`.

[44] Michael J. Hartmann and Giuseppe Carleo. Neural-network approach to dissipative quantum many-body dynamics. *Phys. Rev. Lett.*, 122:250502, Jun 2019. doi: 10.1103/PhysRevLett.122.250502. URL `https://link.aps.org/doi/10.1103/PhysRevLett.122.250502`.

[45] Filippo Vicentini, Alberto Biella, Nicolas Regnault, and Cristiano Ciuti. Variational neural-network ansatz for steady states in open quantum systems. *Phys. Rev. Lett.*, 122:250503, Jun 2019. doi: 10.1103/PhysRevLett.122.250503. URL `https://link.aps.org/doi/10.1103/PhysRevLett.122.250503`.

[46] Johannes Mellak, Enrico Arrigoni, and Wolfgang von der Linden. Deep neural networks as variational solutions for correlated open quantum systems. *Communications Physics*, 7(1):268, 2024. URL `https://www.nature.com/articles/s42005-024-01757-9`.

[47] Richard Cleve and Chunhao Wang. Efficient quantum algorithms for simulating lindblad evolution, 2019. URL `https://arxiv.org/abs/1612.09512`.

[48] Nobuyuki Yoshioka, Yuya O. Nakagawa, Kosuke Mitarai, and Keisuke Fujii. Variational quantum algorithm for nonequilibrium steady states. *Phys. Rev. Res.*, 2:043289, Nov 2020. doi: 10.1103/PhysRevResearch.2.043289. URL `https://link.aps.org/doi/10.1103/PhysRevResearch.2.043289`.

[49] Huan-Yu Liu, Tai-Ping Sun, Yu-Chun Wu, and Guo-Ping Guo. Variational quantum algorithms for the steady states of open quantum systems. *Chinese Physics Letters*, 38(8):080301, sep 2021. doi: 10.1088/0256-307X/38/8/080301. URL `https://dx.doi.org/10.1088/0256-307X/38/8/080301`.

[50] Zhiyan Ding, Xiantao Li, and Lin Lin. Simulating open quantum systems using hamiltonian simulations. *PRX Quantum*, 5:020332, May 2024. doi: 10.1103/PRXQuantum.5.020332. URL `https://link.aps.org/doi/10.1103/PRXQuantum.5.020332`.

[51] Sara Santos, Xinyu Song, and Vincenzo Savona. Low-Rank Variational Quantum Algorithm for the Dynamics of Open Quantum Systems. *Quantum*, 9:1620, February 2025. ISSN 2521-327X. doi: 10.22331/q-2025-02-04-1620. URL `https://doi.org/10.22331/q-2025-02-04-1620`.

[52] Xu-Dan Xie, Zheng-Yuan Xue, and Dan-Bo Zhang. Variational quantum algorithm for solving the liouvillian gap. *Chinese Physics Letters*, 42(8):080605, jul 2025. doi: 10.1088/0256-307X/42/8/080605. URL `https://dx.doi.org/10.1088/0256-307X/42/8/080605`.

[53] Jacopo Tosca, Francesco Carnazza, Luca Giacomelli, and Cristiano Ciuti. Efficient variational dynamics of open quantum bosonic systems via automatic differentiation, 2025. URL `https://arxiv.org/abs/2507.14076`.

[54] Sebastian Paeckel, Thomas Köhler, Andreas Swoboda, Salvatore R. Manmana, Ulrich Schollwöck, and Claudius Hubig. Time-evolution methods for matrix-product states. *Ann.*

Phys., 411:167998, Dec 2019. ISSN 0003-4916. URL `http://dx.doi.org/10.1016/j.aop.2019.167998`.

[55] M. Grundner, P. Westhoff, F. B. Kugler, O. Parcollet, and U. Schollwöck. Complex time evolution in tensor networks and time-dependent green's functions. *Phys. Rev. B*, 109: 155124, Apr 2024. doi: 10.1103/PhysRevB.109.155124. URL `https://link.aps.org/doi/10.1103/PhysRevB.109.155124`.

[56] Sebastian Paeckel. Spectral decomposition and high-accuracy greens functions: Overcoming the nyquist-shannon limit via complex-time krylov expansion, 2025. URL `https://arxiv.org/abs/2411.09680`.

[57] Markus Greiner, Olaf Mandel, Tilman Esslinger, Theodor W Hänsch, and Immanuel Bloch. Quantum phase transition from a superfluid to a mott insulator in a gas of ultracold atoms. *Nature*, 415(6867):39–44, January 2002. URL `https://www.nature.com/articles/415039a`.

[58] Robert Jördens, Niels Strohmaier, Kenneth Günter, Henning Moritz, and Tilman Esslinger. A mott insulator of fermionic atoms in an optical lattice. *Nature*, 455(7210): 204–207, September 2008. URL `https://www.nature.com/articles/nature07244`.

[59] M. Aidelsburger, M. Atala, M. Lohse, J. T. Barreiro, B. Paredes, and I. Bloch. Realization of the hofstadter hamiltonian with ultracold atoms in optical lattices. *Phys. Rev. Lett.*, 111:185301, Oct 2013. doi: 10.1103/PhysRevLett.111.185301. URL `https://link.aps.org/doi/10.1103/PhysRevLett.111.185301`.

[60] Gregor Jotzu, Michael Messer, Rémi Desbuquois, Martin Lebrat, Thomas Uehlinger, Daniel Greif, and Tilman Esslinger. Experimental realization of the topological haldane model with ultracold fermions. *Nature*, 515(7526):237–240, November 2014. URL `https://www.nature.com/articles/nature13915`.

[61] Christian Schweizer, Fabian Grusdt, Moritz Berngruber, Luca Barbiero, Eugene Demler, Nathan Goldman, Immanuel Bloch, and Monika Aidelsburger. Floquet approach to z_2 lattice gauge theories with ultracold atoms in optical lattices. *Nature Physics*, 15(11): 1168–1173, 2019. doi: 10.1038/s41567-019-0649-7. URL `https://doi.org/10.1038/s41567-019-0649-7`.

[62] Russell A Hart, Pedro M Duarte, Tsung-Lin Yang, Xinxing Liu, Thereza Paiva, Ehsan Khatami, Richard T Scalettar, Nandini Trivedi, David A Huse, and Randall G Hulet. Observation of antiferromagnetic correlations in the hubbard model with ultracold atoms. *Nature*, 519(7542):211–214, March 2015. URL `https://www.nature.com/articles/nature14223`.

[63] Michael Schreiber, Sean S. Hodgman, Pranjal Bordia, Henrik P. Lüschen, Mark H. Fischer, Ronen Vosk, Ehud Altman, Ulrich Schneider, and Immanuel Bloch. Observation of many-body localization of interacting fermions in a quasirandom optical lattice. *Science*, 349 (6250):842–845, 2015. doi: 10.1126/science.aaa7432. URL `https://www.science.org/doi/abs/10.1126/science.aaa7432`.

[64] Yongtao Zhan, Zhiyan Ding, Jakob Huhn, Johnnie Gray, John Preskill, Garnet Kin-Lic Chan, and Lin Lin. Rapid quantum ground state preparation via dissipative dynamics, 2025. URL `https://arxiv.org/abs/2503.15827`.

[65] Lin Lin. Dissipative preparation of many-body quantum states: Towards practical quantum advantage, 2025. URL `https://arxiv.org/abs/2505.21308`.

[66] X. Mi, A. A. Michailidis, S. Shabani, K. C. Miao, P. V. Klimov, J. Lloyd, E. Rosenberg, R. Acharya, I. Aleiner, T. I. Andersen, M. Ansmann, F. Arute, K. Arya, A. Asfaw, J. Atalaya, J. C. Bardin, A. Bengtsson, G. Bortoli, A. Bourassa, J. Bovaird, L. Brill, M. Broughton, B. B. Buckley, D. A. Buell, T. Burger, B. Burkett, N. Bushnell, Z. Chen, B. Chiaro, D. Chik, C. Chou, J. Cogan, R. Collins, P. Conner, W. Courtney, A. L. Crook, B. Curtin, A. G. Dau, D. M. Debroy, A. Del Toro Barba, S. Demura, A. Di Paolo, I. K. Drozdov, A. Dunsworth, C. Erickson, L. Faoro, E. Farhi, R. Fatemi, V. S. Ferreira, L. F. Burgos, E. Forati, A. G. Fowler, B. Foxen, É. Genois, W. Giang, C. Gidney, D. Gilboa, M. Giustina, R. Gosula, J. A. Gross, S. Habegger, M. C. Hamilton, M. Hansen, M. P. Harrigan, S. D. Harrington, P. Heu, M. R. Hoffmann, S. Hong, T. Huang, A. Huff, W. J. Huggins, L. B. Ioffe, S. V. Isakov, J. Iveland, E. Jeffrey, Z. Jiang, C. Jones, P. Juhas, D. Kafri, K. Kechedzhi, T. Khattar, M. Khezri, M. Kieferová, S. Kim, A. Kitaev, A. R. Klots, A. N. Korotkov, F. Kostritsa, J. M. Kreikebaum, D. Landhuis, P. Laptev, K.-M. Lau, L. Laws, J. Lee, K. W. Lee, Y. D. Lensky, B. J. Lester, A. T. Lill, W. Liu, A. Locharla, F. D. Malone, O. Martin, J. R. McClean, M. McEwen, A. Mieszala, S. Montazeri, A. Morvan, R. Movassagh, W. Mruczkiewicz, M. Neeley, C. Neill, A. Nersisyan, M. Newman, J. H. Ng, A. Nguyen, M. Nguyen, M. Y. Niu, T. E. O'Brien, A. Opremcak, A. Petukhov, R. Potter, L. P. Pryadko, C. Quintana, C. Rocque, N. C. Rubin, N. Saei, D. Sank, K. Sankaragomathi, K. J. Satzinger, H. F. Schurkus, C. Schuster, M. J. Shearn, A. Shorter, N. Shutty, V. Shvarts, J. Skruzny, W. C. Smith, R. Somma, G. Sterling, D. Strain, M. Szalay, A. Torres, G. Vidal, B. Villalonga, C. V. Heidweiller, T. White, B. W. K. Woo, C. Xing, Z. J. Yao, P. Yeh, J. Yoo, G. Young, A. Zalcman, Y. Zhang, N. Zhu, N. Zobrist, H. Neven, R. Babbush, D. Bacon, S. Boixo, J. Hilton, E. Lucero, A. Megrant, J. Kelly, Y. Chen, P. Roushan, V. Smelyanskiy, and D. A. Abanin. Stable quantum-correlated many-body states through engineered dissipation. *Science*, 383(6689):1332–1337, 2024. doi: 10.1126/science.adh9932. URL `https://www.science.org/doi/abs/10.1126/science.adh9932`.

[67] Andrew Pocklington and Aashish A. Clerk. Universal time-entanglement trade-off in open quantum systems. *PRX Quantum*, 5:040305, Oct 2024. doi: 10.1103/PRXQuantum.5.040305. URL `https://link.aps.org/doi/10.1103/PRXQuantum.5.040305`.

[68] Jens Eisert and John Preskill. Mind the gaps: The fraught road to quantum advantage, 2025. URL `https://arxiv.org/abs/2510.19928`.

[69] B. Kraus, H. P. Büchler, S. Diehl, A. Kantian, A. Micheli, and P. Zoller. Preparation of entangled states by quantum markov processes. *Phys. Rev. A*, 78:042307, Oct 2008. doi: 10.1103/PhysRevA.78.042307. URL `https://link.aps.org/doi/10.1103/PhysRevA.78.042307`.

[70] Andrea Tomadin, Sebastian Diehl, and Peter Zoller. Nonequilibrium phase diagram of a driven and dissipative many-body system. *Phys. Rev. A*, 83:013611, Jan 2011. doi: 10.1103/PhysRevA.83.013611. URL `https://link.aps.org/doi/10.1103/PhysRevA.83.013611`.

[71] M. Di Liberto, O. Tieleman, V. Branchina, and C. Morais Smith. Finite-momentum bose-einstein condensates in shaken two-dimensional square optical lattices. *Phys. Rev. A*, 84:013607, Jul 2011. doi: 10.1103/PhysRevA.84.013607. URL `https://link.aps.org/doi/10.1103/PhysRevA.84.013607`.

[72] C E Creffield, G Pieplow, F Sols, and N Goldman. Realization of uniform synthetic magnetic fields by periodically shaking an optical square lattice. *New Journal of Physics*, 18(9):093013, sep 2016. doi: 10.1088/1367-2630/18/9/093013. URL `https://dx.doi.org/10.1088/1367-2630/18/9/093013`.

[73] Alexander Impertro, SeungJung Huh, Simon Karch, Julian F. Wienand, Immanuel Bloch, and Monika Aidelsburger, 2024. URL `https://arxiv.org/abs/2412.09481`.

[74] Vittorio Gorini, Andrzej Kossakowski, and Ennackal Chandy George Sudarshan. Completely positive dynamical semigroups of n-level systems. *Journal of Mathematical Physics*, 17(5):821–825, 1976.

[75] Philip Pearle. Simple derivation of the lindblad equation. *European journal of physics*, 33 (4):805, 2012.

[76] Daniel Manzano. A short introduction to the lindblad master equation. *Aip advances*, 10 (2), 2020.

[77] D Manzano and PI Hurtado. Harnessing symmetry to control quantum transport. *Advances in Physics*, 67(1):1–67, 2018.

[78] Daniel Manzano. A short introduction to the Lindblad master equation. *AIP Advances*, 10(2):025106, 02 2020. ISSN 2158-3226. doi: 10.1063/1.5115323. URL `https://doi.org/10.1063/1.5115323`.

[79] Victor V. Albert, Barry Bradlyn, Martin Fraas, and Liang Jiang. Geometry and response of lindbladians. *Phys. Rev. X*, 6:041031, Nov 2016. doi: 10.1103/PhysRevX.6.041031. URL `https://link.aps.org/doi/10.1103/PhysRevX.6.041031`.

[80] Shigeru Ajisaka, Felipe Barra, Carlos Mejía-Monasterio, and Toma ž Prosen. Nonequlibrium particle and energy currents in quantum chains connected to mesoscopic fermi reservoirs. *Phys. Rev. B*, 86:125111, Sep 2012. doi: 10.1103/PhysRevB.86.125111. URL `https://link.aps.org/doi/10.1103/PhysRevB.86.125111`.

[81] Artur M. Lacerda, Archak Purkayastha, Michael Kewming, Gabriel T. Landi, and John Goold. Quantum thermodynamics with fast driving and strong coupling via the mesoscopic leads approach. *Phys. Rev. B*, 107:195117, May 2023. doi: 10.1103/PhysRevB.107.195117. URL `https://link.aps.org/doi/10.1103/PhysRevB.107.195117`.

[82] Victor V. Albert and Liang Jiang. Symmetries and conserved quantities in lindblad master equations. *Phys. Rev. A*, 89:022118, Feb 2014. doi: 10.1103/PhysRevA.89.022118. URL `https://link.aps.org/doi/10.1103/PhysRevA.89.022118`.

[83] E B Mpemba and D G Osborne. Cool? *Phys. Educ.*, 4(3):172, may 1969. doi: 10.1088/0031-9120/4/3/312. URL `https://dx.doi.org/10.1088/0031-9120/4/3/312`.

[84] Avinash Kumar and John Bechhoefer. Exponentially faster cooling in a colloidal system. *Nature*, 584(7819):64–68, August 2020. URL `https://doi.org/10.1038/s41586-020-2560-x`.

[85] Zhiyue Lu and Oren Raz. Nonequilibrium thermodynamics of the markovian mpemba effect and its inverse. *Proceedings of the National Academy of Sciences*, 114(20):5083–5088, 2017. doi: 10.1073/pnas.1701264114. URL `https://www.pnas.org/doi/abs/10.1073/pnas.1701264114`.

[86] Md Taufique Hussain, Oguz Selvitopi, Aydin Buluç, and Ariful Azad. Communication-avoiding and memory-constrained sparse matrix-matrix multiplication at extreme scale. In *2021 IEEE International Parallel and Distributed Processing Symposium (IPDPS)*, pages 90–100. IEEE, 2021.

[87] David Perez-Garcia, Frank Verstraete, Michael M Wolf, and J Ignacio Cirac. Matrix product state representations. *arXiv preprint quant-ph/0608197*, 2006.

[88] J Ignacio Cirac and Frank Verstraete. Renormalization and tensor product states in spin chains and lattices. *Journal of physics a: mathematical and theoretical*, 42(50):504004, 2009.

[89] J Ignacio Cirac, David Perez-Garcia, Norbert Schuch, and Frank Verstraete. Matrix product states and projected entangled pair states: Concepts, symmetries, theorems. *Reviews of Modern Physics*, 93(4):045003, 2021.

[90] Matthew B Hastings. An area law for one-dimensional quantum systems. *Journal of statistical mechanics: theory and experiment*, 2007(08):P08024, 2007.

[91] Pasquale Calabrese and John Cardy. Evolution of entanglement entropy in one-dimensional systems. *Journal of Statistical Mechanics: Theory and Experiment*, 2005(04):P04010, 2005.

[92] Heitor P. Casagrande, Dario Poletti, and Gabriel T. Landi. Analysis of a density matrix renormalization group approach for transport in open quantum systems. *Computer Physics Communications*, 267:108060, 2021. ISSN 0010-4655. doi: https://doi.org/10.1016/j.cpc.2021.108060. URL `https://www.sciencedirect.com/science/article/pii/S0010465521001727`.

[93] C Hubig, IP McCulloch, and Ulrich Schollwöck. Generic construction of efficient matrix product operators. *Physical Review B*, 95(3):035129, 2017.

[94] Sebastian Paeckel, Thomas Köhler, and Salvatore R Manmana. Automated construction of $u(1)$-invariant matrix-product operators from graph representations. *SciPost Physics*, 3(5):035, 2017.

[95] Gregory M Crosswhite and Dave Bacon. Finite automata for caching in matrix product algorithms. *Physical Review A—Atomic, Molecular, and Optical Physics*, 78(1):012356, 2008.

[96] Raz Firanko, Moshe Goldstein, and Itai Arad. Area law for steady states of detailed-balance local lindbladians. *Journal of Mathematical Physics*, 65(5), 2024.

[97] Marko Žnidarič. Relaxation times of dissipative many-body quantum systems. *Physical Review E*, 92(4):042143, 2015.

[98] Ulrich Schollwöck. The density-matrix renormalization group in the age of matrix product states. *Annals of physics*, 326(1):96–192, 2011.

[99] Jutho Haegeman, Christian Lubich, Ivan Oseledets, Bart Vandereycken, and Frank Verstraete. Unifying time evolution and optimization with matrix product states. *Physical Review B*, 94(16):165116, 2016.

[100] Yihe Xu, Zhaoxuan Xie, Xiaoyu Xie, Ulrich Schollwöck, and Haibo Ma. Stochastic adaptive single-site time-dependent variational principle. *JACS Au*, 2(2):335–340, 2022.

[101] Mingru Yang and Steven R White. Time-dependent variational principle with ancillary krylov subspace. *Physical Review B*, 102(9):094315, 2020.

[102] C. Hubig, I. P. McCulloch, U. Schollwöck, and F. A. Wolf. Strictly single-site dmrg algorithm with subspace expansion. *Phys. Rev. B*, 91:155115, Apr 2015. doi: 10.1103/PhysRevB.91.155115. URL `https://link.aps.org/doi/10.1103/PhysRevB.91.155115`.

[103] Jutho Haegeman, J. Ignacio Cirac, Tobias J. Osborne, Iztok Pižorn, Henri Verschelde, and Frank Verstraete. Time-dependent variational principle for quantum lattices. *Phys. Rev. Lett.*, 107:070601, Aug 2011. URL `https://link.aps.org/doi/10.1103/PhysRevLett.107.070601`.

[104] Martin Grundner, Tizian Blatz, John Sous, Ulrich Schollwöck, and Sebastian Paeckel. Cooper-paired bipolaronic superconductors. *arXiv preprint arXiv:2308.13427*, 2023.

[105] M. Moroder. *Simulating quantum dissipative and vibrational environments.* Ph.d. thesis, LMU München, 2024. URL `https://edoc.ub.uni-muenchen.de/34410/`.

[106] Claudius Hubig, Felix Lachenmaier, Nils-Oliver Linden, Teresa Reinhard, Leo Stenzel, Andreas Swoboda, Martin Grundner, Sam Mardazad, Sebastian Paeckel, and Fabian Pauw. The SyTen toolkit. URL `https://syten.eu`.

[107] Claudius Hubig. *Symmetry-Protected Tensor Networks.* PhD thesis, LMU München, 2017. URL `https://edoc.ub.uni-muenchen.de/21348/`.

[108] Frank Verstraete, Michael M Wolf, and J Ignacio Cirac. Quantum computation and quantum-state engineering driven by dissipation. *Nature Physics*, 5(9):633–636, September 2009. URL `https://www.nature.com/articles/nphys1342`.

[109] Baptiste Debecker, John Martin, and Fran çois Damanet. Controlling matter phases beyond markov. *Phys. Rev. Lett.*, 133:140403, Oct 2024. doi: 10.1103/PhysRevLett.133.140403. URL `https://link.aps.org/doi/10.1103/PhysRevLett.133.140403`.

[110] Fabrizio Minganti and Dolf Huybrechts. Arnoldi-lindblad time evolution: Faster-than-the-clock algorithm for the spectrum of time-independent and floquet open quantum systems. *Quantum*, 6:649, February 2022. ISSN 2521-327X. doi: 10.22331/q-2022-02-10-649. URL `http://dx.doi.org/10.22331/q-2022-02-10-649`.

[111] Alexandra Nagy. *Quantum Monte Carlo Approach to the Non-Equilibrium Steady State of Open Quantum Systems.* PhD thesis, École Polytechnique Fédérale de Lausanne (EPFL), Lausanne, 2020. URL `https://infoscience.epfl.ch/handle/20.500.14299/169130`.

[112] Limin Xu. A quantum kinetic monte carlo method for lindblad equation, 2023. URL `https://arxiv.org/abs/2306.05102`.

[113] Gabriel Almeida, Pedro Ribeiro, Masudul Haque, and Lucas Sá. Universality, robustness, and limits of the eigenstate thermalization hypothesis in open quantum systems, 2025. URL `https://arxiv.org/abs/2504.10261`.

[114] Josef Richter, Lucas Sá, and Masudul Haque. Integrability versus chaos in the steady state of many-body open quantum systems. *Phys. Rev. E*, 111:064103, Jun 2025. doi: 10.1103/PhysRevE.111.064103. URL `https://link.aps.org/doi/10.1103/PhysRevE.111.064103`.

[115] E. M. Stoudenmire and Steven R. White. Real-space parallel density matrix renormalization group. *Phys. Rev. B*, 87:155137, Apr 2013. doi: 10.1103/PhysRevB.87.155137. URL `https://link.aps.org/doi/10.1103/PhysRevB.87.155137`.

[116] Martin Grundner, Tizian Blatz, John Sous, Ulrich Schollwöck, and Sebastian Paeckel, 2023. URL `https://arxiv.org/abs/2308.13427`.

[117] Yoshitaka Tanimura. Numerically “exact” approach to open quantum dynamics: The hierarchical equations of motion (heom). *The Journal of Chemical Physics*, 153(2):020901, 07 2020. ISSN 0021-9606. doi: 10.1063/5.0011599. URL `https://doi.org/10.1063/5.0011599`.

[118] M. Yang and S. R. White. Time-dependent variational principle with ancillary Krylov subspace. *Phys. Rev. B*, 102(9), sep 2020. URL `https://doi.org/10.1103%2Fphysrevb.102.094315`.

[119] Dieter Jaksch, Christoph Bruder, Juan Ignacio Cirac, Crispin W Gardiner, and Peter Zoller. Cold bosonic atoms in optical lattices. *Physical Review Letters*, 81(15):3108, 1998.

[120] K. Sengupta and N. Dupuis. Mott-insulator–to–superfluid transition in the bose-hubbard model: A strong-coupling approach. *Phys. Rev. A*, 71:033629, Mar 2005. doi: 10.1103/PhysRevA.71.033629. URL `https://link.aps.org/doi/10.1103/PhysRevA.71.033629`.

[121] Markus Greiner, Olaf Mandel, Tilman Esslinger, Theodor W Hänsch, and Immanuel Bloch. Quantum phase transition from a superfluid to a mott insulator in a gas of ultracold atoms. *nature*, 415(6867):39–44, 2002.

[122] Sebastian Diehl, Andrea Tomadin, Andrea Micheli, Rosario Fazio, and Peter Zoller. Dynamical phase transitions and instabilities in open atomic many-body systems. *Phys. Rev. Lett.*, 105:015702, Jul 2010. doi: 10.1103/PhysRevLett.105.015702. URL `https://link.aps.org/doi/10.1103/PhysRevLett.105.015702`.

[123] A. Griessner, A. J. Daley, S. R. Clark, D. Jaksch, and P. Zoller. Dark-state cooling of atoms by superfluid immersion. *Phys. Rev. Lett.*, 97:220403, Nov 2006. doi: 10.1103/PhysRevLett.97.220403. URL `https://link.aps.org/doi/10.1103/PhysRevLett.97.220403`.

[124] Markus Greiner, Olaf Mandel, Theodor W Hänsch, and Immanuel Bloch. Collapse and revival of the matter wave field of a bose–einstein condensate. *Nature*, 419(6902):51–54, 2002.

[125] K. B. Davis, M. O. Mewes, M. R. Andrews, N. J. van Druten, D. S. Durfee, D. M. Kurn, and W. Ketterle. Bose-einstein condensation in a gas of sodium atoms. *Phys. Rev. Lett.*, 75:3969–3973, Nov 1995. doi: 10.1103/PhysRevLett.75.3969. URL `https://link.aps.org/doi/10.1103/PhysRevLett.75.3969`.

[126] Maximilian Schlosshauer. Quantum decoherence. *Physics Reports*, 831:1–57, October 2019. ISSN 0370-1573. doi: 10.1016/j.physrep.2019.10.001. URL `http://dx.doi.org/10.1016/j.physrep.2019.10.001`.

[127] Oliver Penrose and Lars Onsager. Bose-einstein condensation and liquid helium. *Phys. Rev.*, 104:576–584, Nov 1956. doi: 10.1103/PhysRev.104.576. URL `https://link.aps.org/doi/10.1103/PhysRev.104.576`.

[128] Till D Kühner, Steven R White, and Hartmut Monien. One-dimensional bose-hubbard model with nearest-neighbor interaction. *Physical Review B*, 61(18):12474, 2000.

[129] F. D. M. Haldane. Effective harmonic-fluid approach to low-energy properties of one-dimensional quantum fluids. *Phys. Rev. Lett.*, 47:1840–1843, Dec 1981. doi: 10.1103/PhysRevLett.47.1840. URL `https://link.aps.org/doi/10.1103/PhysRevLett.47.1840`.

[130] Mehran Kardar, Giorgio Parisi, and Yi-Cheng Zhang. Dynamic scaling of growing interfaces. *Physical Review Letters*, 56(9):889, 1986.

[131] L. M. Sieberer, S. D. Huber, E. Altman, and S. Diehl. Dynamical critical phenomena in driven-dissipative systems. *Phys. Rev. Lett.*, 110:195301, May 2013. doi: 10.1103/PhysRevLett.110.195301. URL `https://link.aps.org/doi/10.1103/PhysRevLett.110.195301`.

[132] P. Comaron, G. Dagvadorj, A. Zamora, I. Carusotto, N. P. Proukakis, and M. H. Szymańska. Dynamical critical exponents in driven-dissipative quantum systems. *Phys. Rev. Lett.*, 121:095302, Aug 2018. doi: 10.1103/PhysRevLett.121.095302. URL `https://link.aps.org/doi/10.1103/PhysRevLett.121.095302`.

[133] Marko Ljubotina, Marko Žnidarič, and Toma ž Prosen. Kardar-parisi-zhang physics in the quantum heisenberg magnet. *Phys. Rev. Lett.*, 122:210602, May 2019. doi: 10.1103/PhysRevLett.122.210602. URL `https://link.aps.org/doi/10.1103/PhysRevLett.122.210602`.

[134] Renhao Tao, Maximilian Ammenwerth, Flavien Gyger, Immanuel Bloch, and Johannes Zeiher. High-fidelity detection of large-scale atom arrays in an optical lattice. *Phys. Rev. Lett.*, 133:013401, Jul 2024. doi: 10.1103/PhysRevLett.133.013401. URL `https://link.aps.org/doi/10.1103/PhysRevLett.133.013401`.

[135] Gianluca Teza, Ran Yaacoby, and Oren Raz. Eigenvalue crossing as a phase transition in relaxation dynamics. *Phys. Rev. Lett.*, 130:207103, May 2023. doi: 10.1103/PhysRevLett.130.207103. URL `https://link.aps.org/doi/10.1103/PhysRevLett.130.207103`.

[136] Arthur Ashkin. Optical trapping and manipulation of neutral particles using lasers. *Proceedings of the National Academy of Sciences*, 94(10):4853–4860, 1997.

[137] Giuseppe Pesce, Philip H Jones, Onofrio M Maragò, and Giovanni Volpe. Optical tweezers: theory and practice. *The European Physical Journal Plus*, 135(12):949, 2020.

[138] Cecilia Muldoon, Lukas Brandt, Jian Dong, Dustin Stuart, Edouard Brainis, Matthew Himsworth, and Axel Kuhn. Control and manipulation of cold atoms in optical tweezers. *New Journal of Physics*, 14(7):073051, 2012.

[139] Matthias Seubert, Lukas Hartung, Stephan Welte, Gerhard Rempe, and Emanuele Distante. Tweezer-assisted subwavelength positioning of atomic arrays in an optical cavity. *PRX Quantum*, 6(1):010322, 2025.

[140] Aaron W. Young, William J. Eckner, Nathan Schine, Andrew M. Childs, and Adam M. Kaufman. Tweezer-programmable 2d quantum walks in a hubbard-regime lattice. *Science*, 377(6608):885–889, 2022. doi: 10.1126/science.abo0608. URL `https://www.science.org/doi/abs/10.1126/science.abo0608`.

[141] Immanuel Bloch and Peter Zoller. Ultracold atoms and molecules in optical lattices. In *Contemporary Concepts of Condensed Matter Science*, volume 5, pages 121–156. Elsevier, 2012.

[142] P. Nalbach, D. Braun, and M. Thorwart. Exciton transfer dynamics and quantumness of energy transfer in the fenna-matthews-olson complex. *Phys. Rev. E*, 84:041926, Oct 2011. doi: 10.1103/PhysRevE.84.041926. URL `https://link.aps.org/doi/10.1103/PhysRevE.84.041926`.

[143] Jie Zheng, Yu Xie, Shengshi Jiang, and Zhenggang Lan. Ultrafast nonadiabatic dynamics of singlet fission: Quantum dynamics with the multilayer multiconfigurational time-dependent hartree (ml-mctdh) method. *The Journal of Physical Chemistry C*, 120(3): 1375–1389, 2016. doi: 10.1021/acs.jpcc.5b09921. URL `https://doi.org/10.1021/acs.jpcc.5b09921`.

[144] Andreas Gleis, Seung-Sup B. Lee, Gabriel Kotliar, and Jan von Delft. Emergent properties of the periodic anderson model: A high-resolution, real-frequency study of heavy-fermion quantum criticality. *Phys. Rev. X*, 14:041036, Nov 2024. doi: 10.1103/PhysRevX.14.041036. URL `https://link.aps.org/doi/10.1103/PhysRevX.14.041036`.

[145] Naomichi Hatano. Exceptional points of the lindblad operator of a two-level system. *Molecular Physics*, 117(15-16):2121–2127, 2019. doi: 10.1080/00268976.2019.1593535. URL `https://doi.org/10.1080/00268976.2019.1593535`.

[146] Fabrizio Minganti, Adam Miranowicz, Ravindra W. Chhajlany, and Franco Nori. Quantum exceptional points of non-hermitian hamiltonians and liouvillians: The effects of quantum jumps. *Phys. Rev. A*, 100:062131, Dec 2019. doi: 10.1103/PhysRevA.100.062131. URL `https://link.aps.org/doi/10.1103/PhysRevA.100.062131`.

[147] Cameron Booker, Berislav Buča, and Dieter Jaksch. Non-stationarity and dissipative time crystals: spectral properties and finite-size effects. *New Journal of Physics*, 22(8): 085007, aug 2020. doi: 10.1088/1367-2630/ababc4. URL `https://dx.doi.org/10.1088/1367-2630/ababc4`.

[148] Federico Carollo, Igor Lesanovsky, Mauro Antezza, and Gabriele De Chiara. Quantum thermodynamics of boundary time-crystals. *Quantum Science and Technology*, 9 (3):035024, may 2024. doi: 10.1088/2058-9565/ad3f42. URL `https://dx.doi.org/10.1088/2058-9565/ad3f42`.

[149] J. Tindall, B. Buča, J. R. Coulthard, and D. Jaksch. Heating-induced long-range η pairing in the hubbard model. *Phys. Rev. Lett.*, 123:030603, Jul 2019. doi: 10.1103/PhysRevLett.123.030603. URL `https://link.aps.org/doi/10.1103/PhysRevLett.123.030603`.

Declaration:

I hereby declare that this thesis is my own work, and that I have not used any sources and aids other than those stated in the thesis.

Munich, October 29th, 2025